University of Tennessee, Knoxville

TRACE: Tennessee Research and Creative Exchange

Doctoral Dissertations

Graduate School

5-2005

Fabrication and characterization of nanoelectronic devices for electron beam lithography applications

Xiaojing Yang
University of Tennessee, Knoxville

Follow this and additional works at: https://trace.tennessee.edu/utk_graddiss

Part of the Materials Science and Engineering Commons

Recommended Citation

Yang, Xiaojing, "Fabrication and characterization of nanoelectronic devices for electron beam lithography applications. " PhD diss., University of Tennessee, 2005.
https://trace.tennessee.edu/utk_graddiss/4353

This Dissertation is brought to you for free and open access by the Graduate School at TRACE: Tennessee Research and Creative Exchange. It has been accepted for inclusion in Doctoral Dissertations by an authorized administrator of TRACE: Tennessee Research and Creative Exchange. For more information, please contact trace@utk.edu.

To the Graduate Council:

I am submitting herewith a dissertation written by Xiaojing Yang entitled "Fabrication and characterization of nanoelectronic devices for electron beam lithography applications." I have examined the final electronic copy of this dissertation for form and content and recommend that it be accepted in partial fulfillment of the requirements for the degree of Doctor of Philosophy, with a major in Materials Science and Engineering.

Michael L. Simpson, Major Professor

We have read this dissertation and recommend its acceptance:

D. H. Lowndes, Philip Rack, Ward Plummer, Gregory Peterson

Accepted for the Council:

Carolyn R. Hodges

Vice Provost and Dean of the Graduate School

(Original signatures are on file with official student records.)

To the Graduate Council:

I am submitting herewith a dissertation written by Xiaojing Yang entitled " Fabrication and characterization of nanoelectronic devices for electron beam lithography applications." I have examined the final paper copy of this dissertation for form and content and recommend that it be accepted in partial fulfillment of the requirements for the degree of Doctor of Philosophy, with a major in Materials Science and Engineering.

Michael L. Simpson, Major Professor

We have read this dissertation
and recommend its acceptance:

Accepted for the Council:

Vice Chancellor and Dean of
Graduate Studies

Thesis
2005b
.428

Fabrication and characterization of nanoelectronic devices for electron beam lithography applications

A Dissertation

Presented for the

Doctor of Philosophy Degree

The University of Tennessee, Knoxville

Xiaojing Yang

May 2005

Dedication

This dissertation is dedicated to my beloved family, especially

to my parents and my husband, Hongtao Cui.

Acknowledgements

I am able to complete my dissertation work only with the help and guidance of many people throughout my studies. Foremost, I am grateful to my advisor, Dr. Michael Simpson, for providing me with invaluable advice, excellent guidance and tremendous support. I am also thankful to my committee, Dr. Ward Plummer, Dr. Philip Rack, Dr. Douglas Lowndes and Dr. Gregory Peterson for their time, discussion and assistance.

I am deeply indebted to Dr. Michael Guillorn who introduced me to various research opportunities and trained me in the use of microfabrication equipment. My thesis work is built upon his pioneering work in the field emission device application of carbon nanofibers. I also thank Dr. Dave Patterson of the Defense Advanced Research Projects Agency for funding this project.

I would like to thank Dr. Larry Baylor and Dr. Walter Gardner for their generous help on both numerical simulation and device design. I am indebted to Richard Kasica, Darrell Thomas, Teri Subich and Pam Fleming for technical assistance and useful discussions. I also acknowledge the whole Molecular-Scale Engineering and Nanoscale Technologies (MENT) Research Group, especially Dale Hensley, Dr. Vladimir Merkulov, Dr. Anatoli Melechko, Timothy McKnight, and Derek Austin. I thank Mark Hale and Dr.Lan Zhang for useful discussions.

The electron beam lithography is carried out at Dr. Joy's lab at the University of Tennessee. I would like to thank Dr. Joy and Jennifer Trollinger for providing me access to this machine. I especially thank Jihoon Kim for his training and assistance with that

machine. I would like to thank Dr. Harry Meyer for help with the Auger analysis. I acknowledge Dr. Nance Ericson and Dr. Gerald Jellison for useful discussions on monochromatic light adsorption studies.

The numerical simulation work is carried out using Lorentz 2D and 3D software from Integrated Engineering Software (IES) company. I would like to thank Grant Bilbrough in help with learning the software and setup of the model geometries. I also would like to thank him for his many useful suggestions.

The EBID and sputtering deposition is carried out in Dr. Philip Rack's group at the University of Tennessee. I would like to thank him for providing me the opportunity and for many fruitful discussions. I also thank Steven Randolph for help with the EBID deposition.

I would like to thank Dr. Laura Morris Edwards for her excellent advice and writing help on my dissertation. With her help, I am able to complete my thesis quickly and with high quality.

I acknowledge Gary Alley, Kathy Martin and Gayle Jones for their administrative support.

Lastly, I would like to thank my family, especially my husband, Hongtao Cui, for the love and support.

Abstract

Vertically aligned carbon nanofibers (VACNFs) have shown promise for use as field emission electron sources. Dual-gate field emission structures (triodes) have been fabricated and characterized. The electron beams can be successfully focused in these triodes. These studies show VACNF based field emission devices are promising for electron beam lithography applications. In this thesis, work is continued on triode device investigation. Methods to improve the device fabrication, to understand/optimize the device performance, and to repair defective triodes are presented.

Numerical simulation of the triode performance is included. Depth of field (DOF) of these triode structures is calculated by simulation and is determined to be ~5μm for the current triode structures. The DOF can be improved by employing thicker electrodes. The optimum beam radius is also reduced for thick electrodes. 3D modeling of the structure misalignment shows that a very small and well-converged beam is observed for the maximum shifts studied: 100nm focus electrode shift or 50nm VACNF shift, although astigmatism and coma-type aberrations will increase somewhat from these misalignments. The simulation results are promising and warrant further research on these devices.

Single-gate individual cathode-addressable devices are successfully fabricated. VACNFs are successfully grown on an insulating substrate instead of a conductive silicon substrate for this purpose. Electron field emission is demonstrated to be successful from these devices.

Several possible fabrication schemes to achieve fully self-aligning aperture formation in triode fabrication are designed and discussed. The best way to achieve self-alignment is to employ a process based on both chemical mechanical polishing (CMP) and reactive ion etching (RIE) selectivity. Fully self-aligned devices are successfully fabricated in this manner. Repair on a missing/defective VACNF in triodes is shown to be promising using an electron beam-induced deposition (EBID) technique; both single and dual-gate devices with an EBID deposited nanoemitter are produced and function very well.

TABLE OF CONTENTS

Chapter Page

1. Introduction 1
1.1 Introduction to microelectronics 1
1.2 Introduction to photolithography 3
1.3 Developments of lithography 6
1.4 Parallel electron-beam array lithography concept 13
1.5 The electron source for use in massively parallel electron beam lithography 16
1.6 Vertically aligned carbon nanofiber (VACNF) based electron source 17
1.7 Thesis objective 19

2. Deposition of field emission materials 23
2.1 Growth of VACNFs 23
2.1.1 The structures of carbon nanotubes and carbon nanofibers 23
2.1.2 VACNF growth method 25
2.1.3 VACNF growth model 28
2.1.4 VACNF alignment mechanism 31
2.1.5 VACNF growth control 34
2.1.6 Charge transport properties of VACNFs 40
2.2 Deposition of tungsten nanofibers by the Electron Beam Induced Deposition (EBID) technique 43
2.2.1 Introduction to electron beam induced deposition (EBID) 43
2.2.2 Use of WF_6 instead of $W(CO)_6$ for the EBID deposition of W nanofibers as the field emission element 44

3. Field emission properties of the active nanostructures 47
3.1 Theory of field emission 47
3.2 FE properties of carbon nanofiber related materials 50
3.3 Field emission properties of VACNFs 51
3.4 Adsorbate effects on VACNF field emission behavior 55
3.5 Field emission properties of EBID W nanofibers 64

4. Electron-beam focusing characteristics of double-gated VACNF based field emission devices 69
4.1 The need for numerical simulation investigations 69
4.2 Numerical simulation techniques are widely employed in scientific research 70
4.3 Integrated Engineering Software (IES) — Lorentz 2D and 3D 71
4.4 Lorentz 2D model set-up 74
4.5 2D Simulation results 76
4.6 3D modeling results 82

5. VACNF based FE structures with individual cathode addressability 89
5.1 Individual cathode addressability is an essential part of DEAL concept 89

5.2 Design of individual cathode addressable field emission devices 90
5.3 Growth of VACNFs on a substrate other than silicon 92
5.4 Individual cathode addressable device fabrication 93
5.5 Characterization of the finished devices. 96

6. Fully self-aligned dual-gate structures using VACNFs and investigation of nanoscale electron beam induced deposition techniques as a repair method 100
6.1 Design of fully self-aligned dual-gate devices.....100
6.1.1 Fine registry of VACNFs required for DEAL applications.....100
6.1.2 Literature review on design of fully self-aligned dual-gate structures 101
6.1.3 Design of fully self-aligned dual-gate (triode) structures using VACNFs .103
6.2 Design of field emission devices using W nanofibers selectively grown by EBID… 113
6.2.1 The need to repair VACNF in dual-gate field emission structures.....113
6.2.2 Single-gate field emission devices using W nanofibers selectively grown by nanoscale EBID… 115
6.2.3 Dual-gate field emission devices using W nanofibers selectively grown by nanoscale EBID… 118

7. Conclusion 122
7.1 Conclusion 122
7.2 Future work 125

LIST OF REFERENCES 127

Vita.....138

LIST OF FIGURES

Figure Page

Figure 1-1. General schematic of the steps in a lithographic process 4
Figure 1-2. Semiconductor industry roadmap of memory technology development 7
Figure 1-3. Schematics of a EUV operation system 9
Figure 1-4. Concept of the Curvilinear Variable Axis Lenses (CVAL) 12
Figure 1-5. Concept of maskless massively parallel electron beam lithography 15
Figure 1-6. Process scheme to fabricate dual-gate field emission structures based on VACNFs 20
Figure 2-1. Nanotube formation: schematic drawing of rolling of graphene sheets 24
Figure 2-2. Comparisons of a VACNF and a MWNT 26
Figure 2-3. Illustration of VACNF growth after the "pre-etching" step 29
Figure 2-4. TEM images of a VACNF and the initial growth model 30
Figure 2-5. Electric field distribution at the sample edge during VACNF growth and the resultant VACNF growth direction 32
Figure 2-6. Base-type and tip-type growth 33
Figure 2-7. The effect of varying the diameter of catalysts 35
Figure 2-8. Effects of catalyst thickness on the growth of VACNFs 36
Figure 2-9. Different shapes of VACNFs formed by changing the ratio of C_2H_2 to NH_3 38
Figure 2-10. Sharpening of the VACNF tips by removing the catalyst material gradually 39
Figure 2-11. Vertical contacts to the nanofibers 42
Figure 2-12. A typical W nanofiber by EBID in the gated device 46
Figure 3-1. Band diagram drawing in the process of field emission from a metal 49
Figure 3-2. An emission current versus applied electric field (I-E) curve and Fowler-Nordheim plot (inset) obtained from a forest of VACNFs 53
Figure 3-3. A plot of the calculated electric field at the substrate as a function of the lateral distance away from the anode probe 54
Figure 3-4. Schematic drawing to illustrate the principle of field emission resonance tunneling 57
Figure 3-5. Field emission patterns with one to four lobes from carbon nanotubes at room temperature 58
Figure 3-6. Field emission I-V curves obtained from VACNFs showing steps and hysteresis 60
Figure 3-7. Optical observation of the electron beam evolution on the phosphor anode 62
Figure 3-8. Field emission energy distribution (FEED) 63
Figure 3-9. Field emission instrument setup and a typical electron image on the phosphor anode 65
Figure 3-10. Field emission current-voltage and stability curves obtained from a W cathode device 67
Figure 4-1. The full 2D simulation model geometry with materials assigned 75

Figure 4-2. Three focusing conditions under different focus potentials.....77
Figure 4-3. 2D depth of field simulation results.....79
Figure 4-4. 2D simulation results of electrode thickness effects and the initial electron energy effects.....81
Figure 4-5. The electron beam shape at the anode for a no-misalignment and misaligned structures.....83
Figure 4-6. 3D modeling geometry with electron beams.....85
Figure 4-7. The electron beam shifts as a function of nanofiber or focus electrode shift.....86
Figure 5-1. Achievement of individual cathode addressability.....91
Figure 5-2. VACNFs of various qualities grown on a metal/SiO_2/Si substrate.....94
Figure 5-3. Schematics of the individual cathode-addressable device fabrication processes.....95
Figure 5-4. SEM images of the finished individual cathode-addressable devices.....97
Figure 5-5. A current-voltage (I-V) curve obtained from the fabricated cathode-addressable device.....99
Figure 6-1. Self-aligned silicon-tips field emission devices based on CMP.....102
Figure 6-2. Pictures of the structures after oxide coating on 1μm-tall VACNFs.....104
Figure 6-3. One proposed fully self-aligning fabrication process based on a single CMP process.....106
Figure 6-4. A design scheme to realize fully self-aligning based on two CMP steps for aperture definition.....107
Figure 6-5. AFM and SEM images of the device at various stages of the fabrication scheme in Figure 6-4.....109
Figure 6-6. A fully self-aligning process based on both CMP and etch selectivity of RIE.....111
Figure 6-7. AFM and SEM images of devices following the fabrication scheme in Figure 6-6.....114
Figure 6-8. Diagram of the DEAL lithography redundancy design.....116
Figure 6-9. Summary of the W nanofiber cathode device fabrication process.....117
Figure 6-10. The SEM images of dual-gate devices prior to and after W nanofiber deposition.....119
Figure 6-11. Optical images of the initial lithography lines obtained using these W nanofiber triode structures.....121

Chapter 1

Introduction

1.1 Introduction to microelectronics

Electronic devices have found widespread use in our everyday lives in areas ranging from consumer electronics, automotive/transportation, to information technology, engineering and medical treatments. The fabrication of these devices and the components within is closely related to a field of study called microelectronics. Microelectronics, as its name suggests, is a subfield of electronics and refers to the study and fabrication of small electronic components.

In 1947, William Shockley, John Bardeen and Walter Brattain invented the first transistor at Bell labs [1]. This device was able to modulate current between two electrodes through the application of a voltage at a third terminal. This invention resulted in profound changes to the engineering world. This simple device has become the parent of all various semiconductor transistor devices including computer microprocessors, memory chips, and solid state power amplification circuits in use today.

The next major invention in the semiconductor industry was monolithic integrated circuits by Jack Kilby and Robert Noyce in 1960 [2]. Kilby and Noyce were able to integrate many solid state transistors and interconnect them internally on a single semiconductor substrate. Although the typical minimum feature size was greater than

20mm at that time, the ability to interconnect the devices internally allowed more advanced and complex functions to be performed by a single device. It was the invention of the integrated circuit that ushered in the modern microelectronics era.

The semiconductor industry has developed quickly since then. Tremendous efforts have been devoted to shrinking the dimensions of the minimum feature sizes of semiconductor devices. It is largely the success of these efforts that has driven the dramatic growth in the semiconductor industry. It is obvious that reductions in feature sizes allow more devices to be integrated on a specific area, which in turn result in more functional and economical products. Reduction in the feature size, especially in the size of transistor gate structures, has also led to dramatic increases in the speed of the logic devices that power complex computational circuits [2].

The manufacturing of small feature sized devices was enabled by advances in lithographic technologies [2-4]. Lithography and microlithography refer to the techniques and methods used in printing the circuit element patterns employed in the construction of semiconductor devices. This lithographic process allows the definition of devices on small, well-defined areas of the semiconductor substrate. The integrated circuits are then manufactured by repeatedly processing the substrates through a cycle of basic unit operations, such as film deposition, lithography and etch. The overall cycle may be repeated 20 to 30 times for modern logic devices.

1.2 Introduction to photolithography

The basic photolithographic steps are shown in Figure 1-1 [5]. The first step is to prepare the substrate. The substrate may need to be cleaned and a prime step may also be added, in which the substrate is exposed to a reagent (*e.g.* hexamethyldisilizane) to modify the surface chemistry of the substrate to improve the adhesion of the photoresist to the surface. The photoresist, or resist, is a special material that will undergo changes in its physical and/or chemical properties upon exposure to radiation.

In the next step, photoresist is applied. The photoresist, mixed in the form of a solution in an organic solvent, is spin-coated onto the substrate and soft baked on a hot plate to remove residual casting solvent. The photoresist coated substrate is then exposed to radiation, typically ultraviolet light. The exposure tool uses a mask to selectively expose the desired pattern onto the photoresist. Following exposure, the resist is typically post-exposure baked on a hot plate. The whole substrate is then treated with a developing solvent, by immersion or some other technique that selectively dissolves either the exposed or unexposed areas depending on the nature of the resist. The areas of the substrate that are no longer covered by photoresist can then be subject to further processing such as plasma etching. The remaining resist patterns serve as a barrier that protects the underlying substrate from these processes. Once the substrate is processed, the photoresist layer is stripped using a stronger solvent or plasma etching and the entire process can be repeated for each layer of the device.

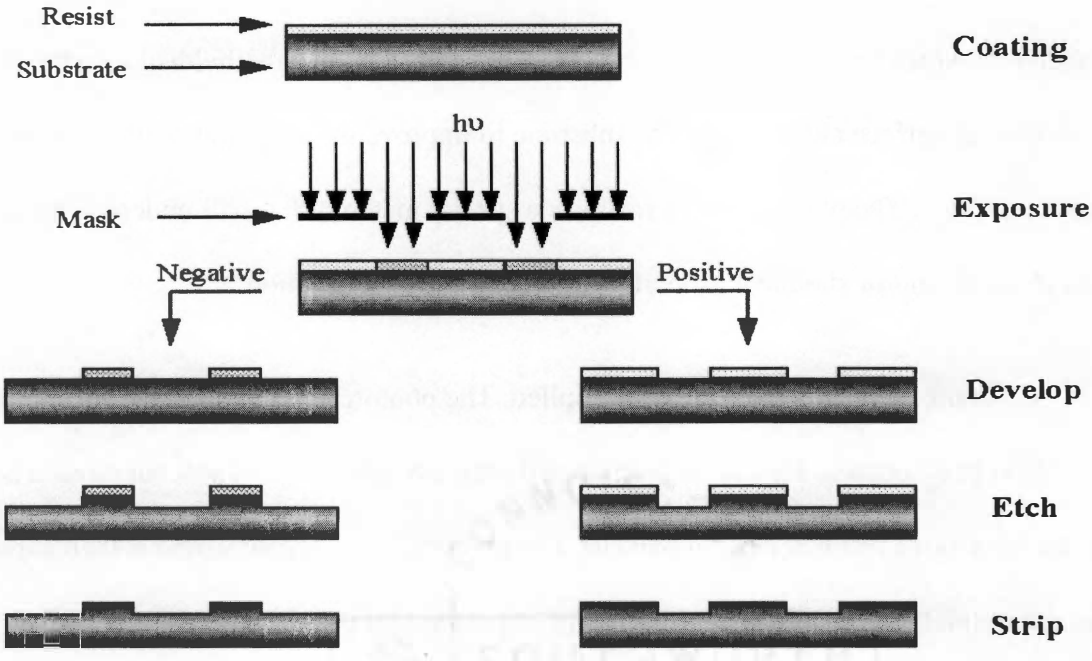

Figure 1-1. General schematic of the steps in a lithographic process.

Adapted from reference [5].

The resolution of a diffraction-limited lithographic process is given by the Raleigh criterion, as shown in equation (1-1) and (1-2),

$$RESOLUTION = k_1 \frac{\lambda}{NA} \qquad (1\text{-}1)$$

$$DOF = k_2 \lambda / NA^2 \qquad (1\text{-}2)$$

where DOF denotes depth of focus, λ is the wavelength of radiation used, *NA* is the numerical aperture of the lens in the projection tool exposure system, and k_1 and k_2 are process dependent adjustment factors. The k_1 and k_2 factors are controlled by a variety of factors, including the photoresist performance and tool issues such as lens aberration. The numerical aperture is defined as the sine of the capture angle of the lens, and is a measure of the size of the lens system.

All of these factors are under investigation in order to print smaller features. Exposure tool manufacturers are developing lens systems with higher numerical apertures. Semiconductor manufacturers, aided by resist makers and other tool suppliers, are learning to manufacture with lower k_1 factors. However, in order to significantly reduce feature size, photoresist exposure wavelengths must be reduced. As can be seen from equation (1-1), the shorter the wavelength, the smaller the feature size.

1.3 Developments in lithography

More than 40 years ago, Intel founder Gordon Moore predicted that the number of transistors on a microprocessor would double every 18 months. This became known as Moore's Law [6].

Figure 1-2 shows the progression of memory technologies over the past 25 years, along with projections of future technologies [5]. This progression conforms closely to Moore's law. The plot also shows the lithographic technologies used to manufacture each device generation. As is shown in the figure, the main method to reduce the device critical dimensions has been to continually reduce the wavelength of the radiation used to expose the photoresist.

Light sources have also been continuously improved along with the effort of radiation wavelength reduction. Initially, the photolithography light source was a mercury lamp filtered for G and H-lines at wavelengths of 436nm and 405nm, respectively. This was adequate for creating features down to about 0.4μm. Around 1990, the 365nm i-line in the near ultra violet was filtered from the mercury lamp and this allowed the definition of features down to about 0.3μm.The development of lithography at a wavelength of 248nm required the invention of new light sources such as the reliable and narrow-linewidth KrF laser. This was called deep ultraviolet (DUV) lithography. DUV lithography with a 248nm source can print features as small as ~200nm. Other DUV sources provide a decrease in wavelength to 194nm (ArF laser) and perhaps 157nm

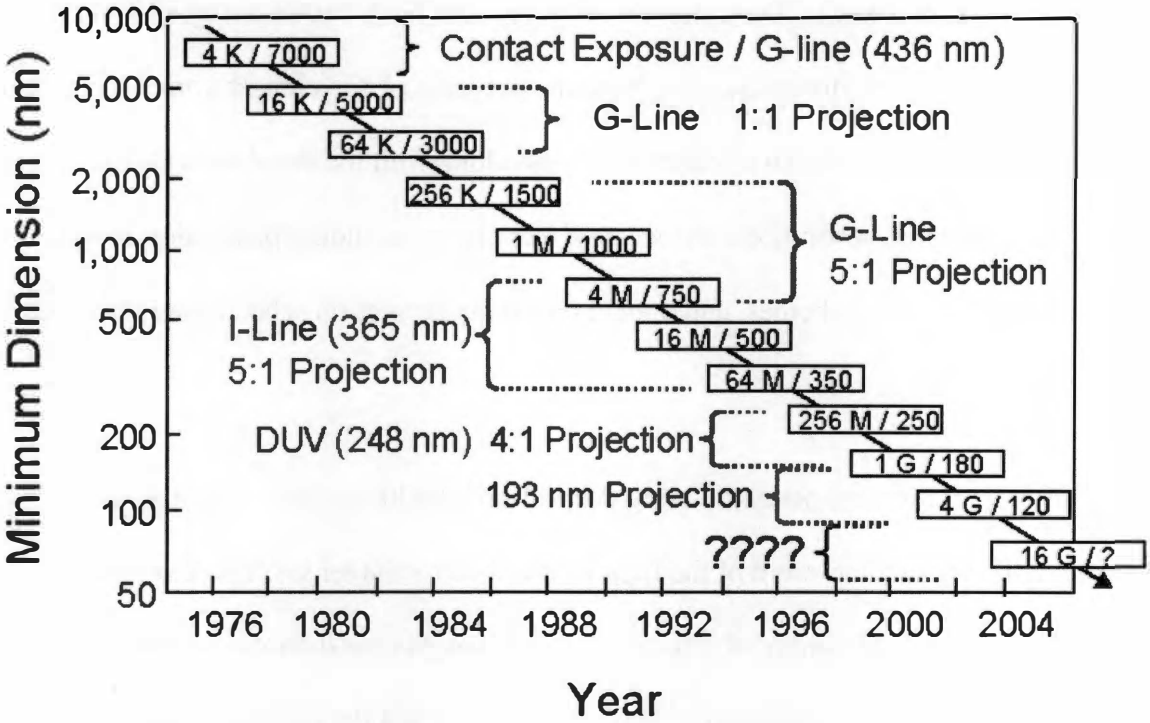

Figure 1-2. Semiconductor industry roadmap of memory technology development. The associated lithographic technologies used to the manufacture of each device generation are also shown. Each box shows each device generation's memory size and critical feature size (nm). Reprinted from reference [5].

(Fluorine Excimer Laser). The smallest feature that can be patterned using 194nm wavelength is ~90nm. However, along with the decrease of wavelength comes a decrease in the depth of field as shown in equation (2). So along with the developments of lithography systems, resolution enhancement techniques including phase-shift masks, modified illumination schemes, and optical proximity correction schemes are also under investigation.

A serious problem posed by using deep-ultraviolet lithography is that as the wavelengths get smaller, more of the light is absorbed by the lenses. There simply is no material with a sizeable index of refraction at wavelengths considerably below 157nm that can be turned into a high-quality lens. The result is that the light is absorbed before reaching the substrate/silicon wafer, making lithography impossible.

Extreme ultraviolet (EUV) has been considered one of the most promising solutions for next generation lithography (NGL) tools to produce features below 100nm. EUV lithography utilizes a 13.4nm wavelength and is capable of printing features 100nm and below.

EUV imaging systems are entirely reflective because of the much shorter wavelength involved. In EUV systems (Figure 1-3) [7-8], the light first travels into a condenser, which gathers in the light and directs it onto the mask. The pattern on the mask is reflected onto a series of four to six curved mirrors, reducing the size of the image and focusing the image onto the silicon wafer. Each mirror bends the light slightly to form the image that will be transferred onto the wafer.

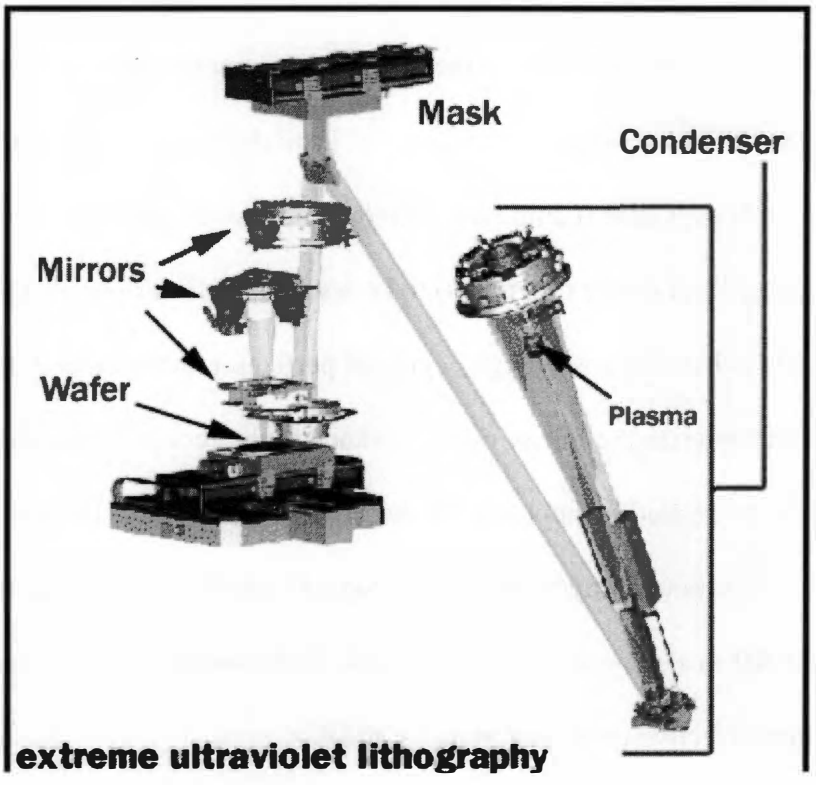

Figure 1-3. Schematics of a EUV operation system. Image source: Sandia National Laboratories.

The mirror surfaces must have very high reflectivity for wavelengths around 13nm and this is generally achieved by coating with multilayer thin films (MLs) (Mo: Si). Because of the short wavelength of EUV, the mirror surface needs to be of extremely high quality: roughness with wavelength in the range of 1mm through 1μm (mid-spatial frequency roughness) to be less than 0.2nm rms, and roughness with spatial wavelength less than 1μm (high-spatial frequency roughness) to be less than 0.1nm rms [8]. There are significant challenges to achieving a very high degree of perfection in the surface finish of the mirrors and to characterize the mirror quality to such high precision. The mask is also a mirror with patterns created by applying the patterned absorber over the ML reflector. As mask repair is almost impossible, a technique to achieve defect-free masks (depositing defect-free MLs) also needs to be developed. Additional research is also required to develop new effective resist materials for EUV.

In contrast to optical lithography systems, electron-beam lithography systems easily create extremely fine patterns. This is because the electron beam spot size is usually very small and the resolution is not limited by diffraction due to the much shorter wavelength of the electrons. An important use of EBL is in photo-mask production. EBL is also widely used for research into quantum effects and other novel physics phenomena at very small dimensions. However, the long writing time, resulting in low throughput, continues to be the major challenge for electron-beam lithography.

One of the other candidates for NGL from the electron beam point of view is called electron-beam projection lithography (EPL) [9]. This concept involves the projection of sections of a chip pattern, called "subfields", using a 4X mask onto a wafer.

The subfield is small compared to the size of the chip, but large compared to the patterned features. The complete IC chip is then generated by stitching together the subfields.

Currently IBM, in cooperation with Nikon, is investigating novel electron optical methods for utilizing EPL. Usually as a consequence of beam scanning, off-axis aberrations are generated. Researchers at IBM utilize Curvilinear Variable Axis Lenses (Figure 1-4) to simultaneously shift the optical axis along with the deflected beam to overcome the off-axis aberrations [9]. Their approach— Projection Reduction Exposure with Variable Axis Immersion Lenses (PREVAIL) — combines electronic beam scanning with continuous stage motions. By sequentially exposing and stitching together 0.25mm subfields at the target wafers, PREVAIL can achieve an effective field size of 5mm at sub 100nm resolution.

For the PREVAIL system, significant effort is needed for the design of a high-emittance electron source, in particular, for the provisions of extremely uniform heating of the large disk cathode at the electron gun. Optical lithography reticles, such as chrome-on-glass masks are not feasible for the PREVAIL system because of the short penetration length of electron beams. New materials, such as membrane or stencil masks, need to be developed. In the PREVAIL system, subfield distortion and shape astigmatism also needs to be monitored and corrected.

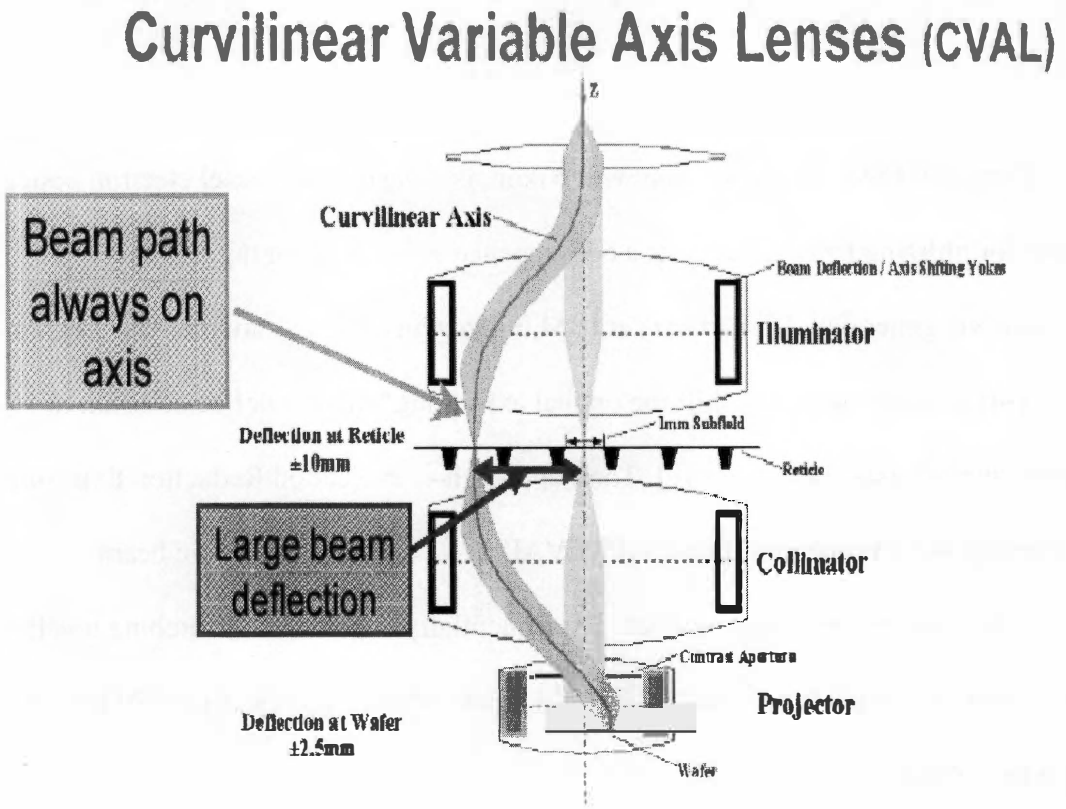

Figure 1-4. Concept of the Curvilinear Variable Axis Lenses (CVAL). Reference [9].

Both EUV and EPL approaches still face enormous challenges, both in the systems themselves and the masks required. Other possible solutions for an NGL system include X-ray lithography and immersion lithography. They are not as mature as EUV and EPL and it is difficult to judge their potential for NGL at this time.

1.4 Parallel electron-beam array lithography concept

A maskless electron beam lithography system based on negative electron affinity has been investigated by Schneider *et al.* [10]. A large band gap (*e.g.* GaN) photocathode coated with a surface layer of electropositive material (Cs_2O) is employed. Because of this activation layer, the conduction band is now above the vacuum level— a condition called Negative Electron Affinity. The stimulating laser strikes the active region of the photocathode and electrons are emitted. For lithography applications, the photocathode needs to be patterned to obtain sub-optical emission areas. Issues such as quantum efficiency and emission stability are currently under investigation.

Chang *et al.* introduced the concept of "miniaturized scanning electron microcolumns" for EBL and electron microscope applications [11]. He proposed using arrays of these microcolumns for 100nm lithography. However, a large number of microcolumns (>100) are needed in order to achieve high throughput.

Baylor *et al.* [12] introduced the concept of massively parallel electron beam lithography — Digitally Addressable Electron Beam Array Lithography (DEAL), which uses electrostatically focused electron-beam arrays for direct write. This concept employs VACNFs based field emission dual-gate triodes, which are used as part of a "digitally

addressable field emission array" (DAFEA). This proposed system employs a large array of independently modulated miniature electron beams and a raster scan system that offer the advantages of being maskless.

A schematic of this concept microfabricated on a silicon integrated circuit containing the logic and memory and control circuits is shown in Figure 1-5. This concept utilizes a very high density of emitter cathodes ($\sim 3\times10^{6}/cm^{2}$) so the DAFEA plane can be angled slightly with respect to the wafer (~0.4 degree) and multiple emitters can individually illuminate every 30nm pixel on a 300mm wafer. This allows for redundancy of emitters illuminating any pixel and thus allows for up to two bad emitters per ten-emitter column.

As is well known, electron beam proximity effects limit the resolution of EBL at high electron energies [13]. As the electrons penetrate into the resist material, some of them experience small angle forward scattering and many of them experience large angle scattering events leading to back scattering, which will cause additional exposure in the resist, thus broadening the feature. This concept is designed to use electron energy less than 1keV, so it should not be appreciably affected by these proximity effects. Also there should not be any space charge limitation for this low-current operation.

A Logic-Memory-Circuit (LMC) is employed in the DAFEA to control emission from the individual emitters. The LMC circuit consists of logical shifts that allow a

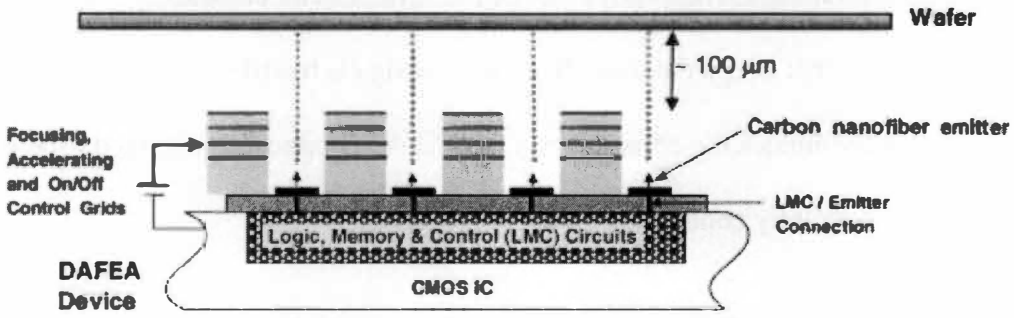

Figure 1-5. Concept of maskless massively parallel electron beam lithography. Reference [12]

pattern of "on" and "off" pixels to be stored. This digital addressability eliminates the need for conventional masks. The control part of the LMC circuit consists of a dose control circuit (DCC) that keeps the dose delivered during each write cycle. A dose control circuit that terminates the emission at a fixed dose as opposed to a fixed time is required for this lithography concept.

1.5 The electron source for use in massively parallel electron beam lithography

The following properties are desired for a field emission cathode:

1) low emission threshold field, E_{th}, for initiation of electron emission;
2) high emitted current density;
3) resistance to sputtering by residual gases in the operating environment;
4) low current noise and uniformity in operating characteristics;
5) low energy spread (Cold field emitted electrons have low energy spread of 0.2-0.3eV).

The conventional Spindt-type field emission tips [14] have a relatively blunt tip and high fields are needed to initiate field emission. Some of them require complex fabrication procedures. Their lifetime is short and a very high vacuum is needed for operation. Carbon materials offer additional advantages in field emission compared to conventional metal or silicon emitters, such as longer lifetime, more resistance to gas

bombardment, and the ability to operate in harsh environments. Recent research in flat panel displays has turned to carbon nanotube-based emitter materials for field emission elements.

1.6 Vertically aligned carbon nanofiber (VACNF) based electron source

Vertically Aligned Carbon Nanofibers (VACNFs) [15-23] are similar to carbon nanotubes and possess a high geometric field enhancement due to their small tip sizes. Additionally, single VACNFs can be grown at predetermined locations making the further integration of them easier and at deterministic locations. VACNFs have been found to be compatible with standard processing techniques [21-22], thus making an attractive electron source for this massively parallel electron beam lithography.

Vertically Aligned Carbon Nanofibers are usually catalytically grown in a plasma enhanced chemical vapor deposition chamber. The VACNF growth is catalytically controlled so that the presence of a fiber at a given location is completely determined by catalyst pre-deposition. By lithographically patterning catalyst deposition, and by appropriately controlling subsequent growth conditions, fiber growth becomes deterministic allowing one to control the location, height and diameter of the VACNF [15-17]. Consequently, VACNFs can be grown as isolated individual cathodes and in very large patterned arrays [16-19]. Further work has shown that the shape of the fibers can be tailored during the growth process resulting in conical, cylindrical and cylinder-on-cone geometries [16]. VACNF growth mechanism and control are further discussed in Chapter 2.

Field emission properties of individual VACNFs have been measured with a moveable current probe capable of positioning the anode probe tip above an individual VACNF with submicron accuracy [18]. It has been shown that isolated VACNFs are good field emitters with emission threshold fields of 15-50V/μm. Isolated VACNFs have displayed stable emission for over 175 hours (the longest period of test) of continuous 10nA operation at vacuum levels of 10^{-6} torr. Field emission current versus voltage (I-V) analysis has shown a maximum measured FE current exceeding 5 μA without any degradation to the VACNF tip. Details of VACNF field emission properties are discussed in Chapter 3.

Utilization of VACNFs in electrostatic gating structures was first demonstrated by Guillorn *et al.* [20]. This process first completed the gate aperture patterning followed by growth of VACNFs. The necessity to bias the gate during growth prevented this process from being adaptable to wafer-level production, a necessary capability for practical application. Later, it was demonstrated that it is possible to further process VACNFs for functional gated devices [21]; in this paper, this fabrication process was wafer level based and the yield was greatly improved. Soon self-aligned gated field emission devices using individual VACNFs were reported [22], and the gate apertures were well aligned to VACNFs, based on self-aligning during chemical mechanical polishing. This work [21, 22] also demonstrated that the carbon nanofibers did not seem to degrade during film deposition, plasma etching and wet chemical etching. The finished devices displayed FN behavior and the device can function at 20nA continuously without degradation [22]. Dual-gate structures were also successfully fabricated [23] with the upper electrode

serving as a focus electrode. A focused electron beam could thus be generated from these VACNFs. Figure 1-6 shows the fabrication process for these dual gate structures.

1.7 Thesis objective

This thesis focuses on efforts to investigate and improve on current field emission device design to realize the massively parallel electron-beam array lithography concept (DEAL), as discussed in section 1.4. This thesis presents theoretical simulation work to better understand the operation of these devices and to direct the experiment design. It presents research results on design, characterization and optimization of the microfabricated field emission devices. The consideration for several aspects of device design is discussed along with the device design solutions.

This thesis begins an overview of the active nanoscale FE element growth study and its field emission behavior. Then a numerical investigation of the dual-gate device behaviors is carried out. The various designs and realization of field emission devices are then discussed, including how to achieve individual cathode addressability and how to fabricate fully self-aligned devices. Electron beam induced deposition (EBID) techniques are explored for device repair. Finally, conclusions are drawn from this thesis work.

Since VACNFs are utilized as the electron sources for the DEAL applications and are further incorporated in the fabrication of field emission device arrays, an overview of the VACNF growth aspects that are related to this electron-beam lithography application is given in Chapter 2. The growth mechanism of VACNFs is also discussed with an

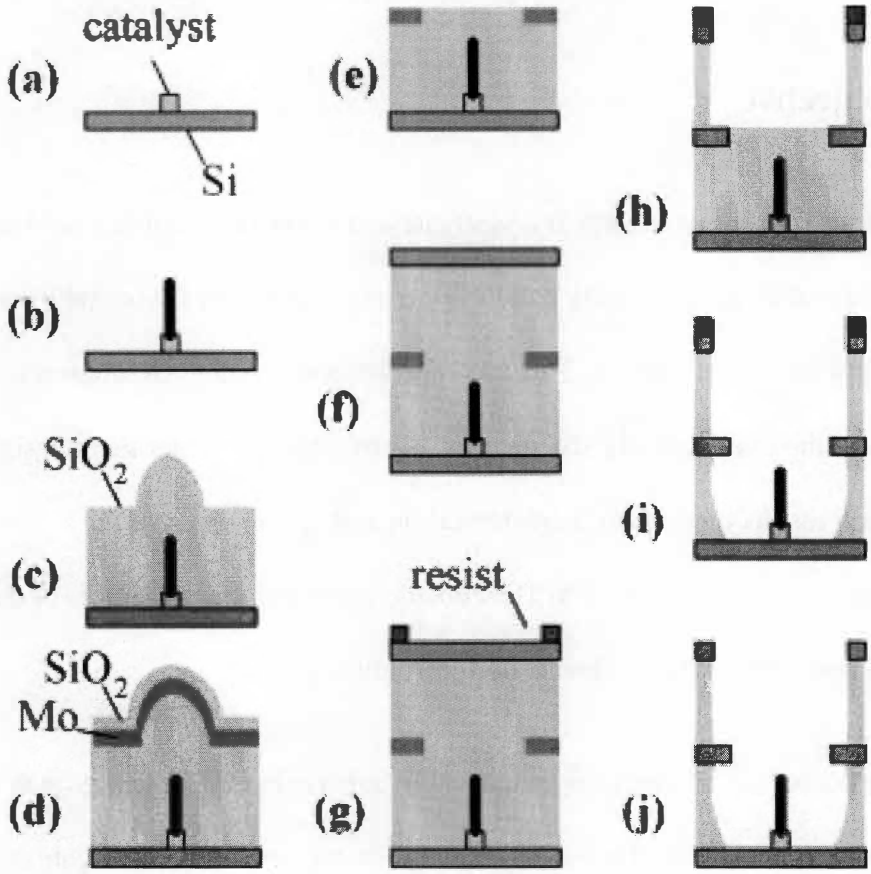

Figure 1-6. Process scheme to fabricate dual-gate field emission structures based on VACNFs. The first aperture was defined by chemical mechanical polishing (e) and the second aperture was defined by photolithography (g)-(j). Reprinted from [23].

emphasis on how to achieve vertical alignment of carbon nanofibers. The effects of parameters that govern the synthesis of the VACNFs are discussed, such as catalyst size and thickness, plasma conditions, and gas conditions. In addition, electrical transport properties of VACNFs are also presented in this chapter. Deposition techniques using EBID to produce nanoscale FE structures are also included here.

Chapter 3 begins with an introduction to the FE process followed by the FE characteristics of carbon materials, especially of VACNFs. Then, along with a review of gas adsorption effects on the electronic properties of carbon-based materials, the effects of gas environment effects on the performance of VACNF field emission are discussed. Field emission properties of a W nanofiber deposited by EBID are also included in this chapter.

Numerical simulation of the electron trajectories and device performance on the current VACNFs-based FE triode structures [23] is described in Chapter 4. Depth of field of these triode structures is calculated by simulation. The electrode thickness effects on the device behavior, especially on the focusing property and depth of field are also presented. In addition, focus electrode/VACNF misalignment impacts on the final electron beam path are also presented, with an emphasis on the final electron beam shape. This chapter is highly modified from a paper submitted to the Journal of Vacuum Science and Technology B.

The design of individual cathode-addressable field emission devices is discussed in Chapter 5. This chapter begins with the discussion on the need to achieve individual

cathode control for DEAL applications. In order to realize individual cathode addressability, it is required to grow VACNFs on an "insulating" substrate and possible strategies are discussed. Microfabrication of single gated FE devices using VACNFs on "insulating" substrates is then carried out and detailed. Electrical field-testing on the finished cathode-addressable devices is also included.

The efforts to realize self-aligning dual-gate devices with VACNFs are detailed in Chapter 6. Self- aligning is the best and perhaps only method to fabricate VACNFs-based dual-gate devices in very well aligned arrays on the wafer scale. The challenges to carry out self-aligning on nanoscale tips compared to conventional silicon tips are included in this chapter. Different fabrication processes are proposed with a discussion on the actual experimental limitations. One of these proposed processes is determined to be the best way to achieve self-alignment and characterization of this process is reported in Chapter 6. At the end of this chapter, the prospect of using three-dimensional nanostructures produced by EBID as a repair method for existing VACNFs-based devices is explored. The current device failure rate is beyond DEAL redundancy design and thus there is need for device repair. Along with a brief introduction to EBID technique, the integration of field emission devices with W nanofibers by EBID is carried out and detailed. Both single-gated (cathode) and double-gated (triode) devices are successfully fabricated. Initial lithography test obtained with the W triode device is also included.

Chapter 7 will summarize all the results and conclusions from this work with a discussion of possible future work.

Chapter 2

Deposition of field emission materials

2.1 Growth of VACNFs

2.1.1The structures of carbon nanotubes and carbon nanofibers

Controlled synthesis and characterization of nanoscale structures is an important step toward the realization of practical devices with these nanoscale structures. Two different kinds of nanoscale materials are investigated in this thesis: VACNFs grown by DC-PECVD and W nanofibers by electron beam induced deposition (EBID). Deposition of both structures is discussed with an emphasis on the VACNF deposition.

Before the discussion of VACNFs, CNTs structures are introduced here first because of the close similarity of VACNFs. Carbon nanotubes are seamless cylinders that can be derived from a single atomic layer of crystalline graphite called a graphene sheet [24]. A single walled carbon nanotube (SWNT) can be seen as the rolling-up of only one graphite sheet into a cylinder with a diameter of a few nanometers, while a multi-walled carbon nanotube (MWNT) is made of several concentric graphene sheets around a common central axis (Figure 2-1).

Depending on the rolling of the graphene sheet, each SWNT is designated an (n, m) tube as shown in Figure 2-1. (N, 0) and (n, n) tubes are also called zigzag tubes and

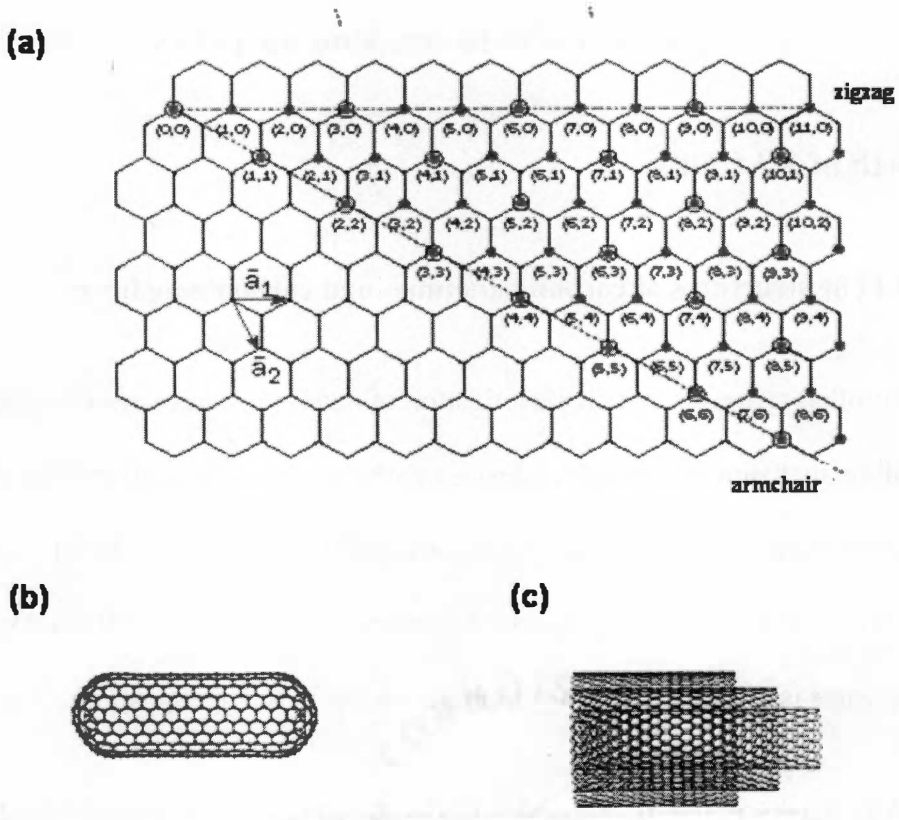

Figure 2-1. Nanotube formation: schematic drawing of rolling of graphene sheets. (a) A graphene sheet orientation with (n, m) notation. An (n, m) SWNT is created by rolling the graphene sheet and joining points (0, 0) and (n, m). (b) A SWNT structure. (c) A MWNT structure. Reference [24-25]

armchair tubes respectively as seen in Figure 2-1. Calculation shows that when $|n-m| = 3q$ (q is an integer), the tube is metallic; otherwise it is semiconducting [25]. Since a MWNT is a coaxial arrangement of several SWNTs, each of which may have different values of n and m, most MWNTs are metallic.

Carbon nanofibers (CNFs), or vertically aligned carbon nanofibers (VACNFs) are similar to CNTs in external morphologies, but there is a distinct structural difference. Properties of VACNFs are expected to be different from those of MWNTs, as will be discussed later in this chapter. A CNT consists of a concentric graphene cylinder. A VACNF is usually composed of graphitic "funnels" and cones, also referred to as a "herringbone" and "bamboo-like" structure [17, 26-27]. Comparison of the two structures is shown in Figure 2-2. A VACNF is not a MWNT with higher degree of crystallinity; the long-range crystalline structure of a VACNF is entirely different from a MWNT.

2.1.2 VACNF growth method

Catalytic growth of carbon nanofibers was first studied about 15 years ago [28]. Almost a decade later, it was shown that VACNFs can be synthesized using plasma enhanced hot-filament chemical vapor deposition [29].

For a typical direct-current plasma enhanced chemical vapor deposition (DC PECVD), a conductive substrate must be provided for use as the cathode. Secondary electrons are generated from the cathode surface during the impact of energetic ions and

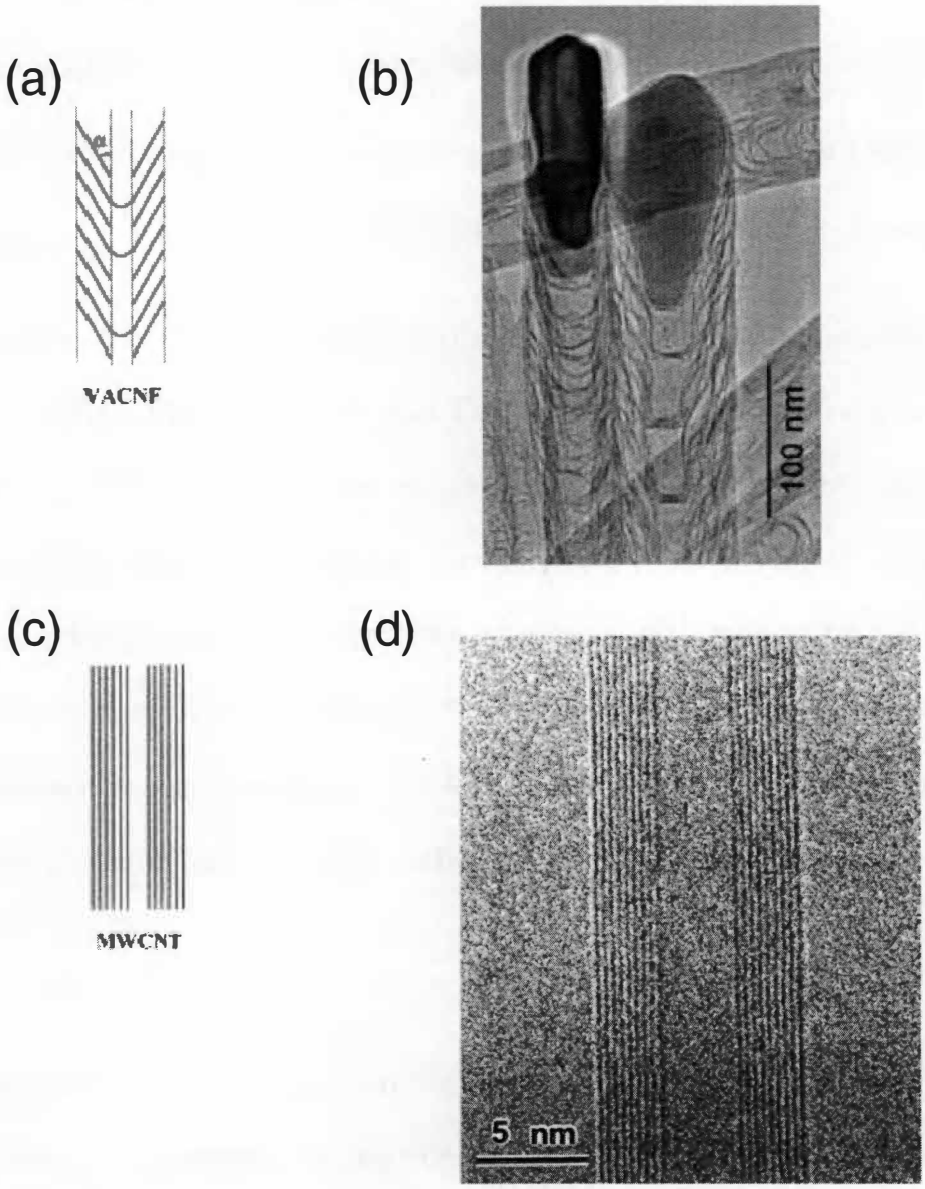

Figure 2-2. Comparisons of a VACNF and a MWNT. (a) and (b) are a schematic design and transmission electron microscope (TEM) photograph of a VACNF; (c) and (d) are a schematic design and transmission electron microscope (TEM) photograph of a MWNT.

sustain the plasma discharge. The yield of secondary electrons from nonconductive substrates is usually insufficient [30]. Another reason to use a conductive substrate for this thesis study is the need to electrically contact the carbon nanofibers for use as field emission guns.

A catalyst is required for VACNF growth. The catalyst is usually a transition metal, such as nickel (Ni), iron (Fe) , cobalt (Co), copper (Cu) or alloys of these metals [17, 27, 31-35]. Lithographical patterning of catalysts is performed. Between the substrate and catalysts, a buffer layer is required. Titanium (Ti), TiN, or a thin layer of silicon oxide (< 20Å, often referred to as native oxide) can be used for this purpose [36].

For the growth of VACNF using DC PECVD as performed at Oak Ridge National Laboratory [17, 27, 32], the sample is mounted directly on a heater plate, which also serves as the cathode. The growth chamber is first evacuated before growth to a base pressure (~20mTorr). Then ammonia (NH_3) (or hydrogen, H_2) is introduced into the chamber and the sample is pretreated with the NH_3 plasma at elevated temperatures. This process is referred to as the "pre-etching" step. During this process, catalyst nanoparticles are formed [27, 32]. These nanoparticles act as the necessary seeds for the catalytic growth of isolated VACNFs. After this pre-etching step with NH_3, with the NH_3 plasma still on, C_2H_2 is introduced into the chamber and the VACNF growth begins. The temperature during growth is ~700°C as measured by a thermocouple. The growth time varies depending on the length of VACNFs needed. At the end of growth, the system is switched off and the chamber is allowed to cool before the wafer is removed.

2.1.3 VACNF growth model

As described earlier in Section 2.1.2, catalyst nanoparticles are formed in the pre-etching step. When acetylene (C_2H_2) or other carbonaceous gas is introduced to the reactor chamber, positively charged carbon radicals are generated and they are accelerated towards the cathode due to the electrical field present. These carbon radicals then meet the catalyst nanoparticles and diffuse through them. Eventually the carbon precipitates out of the catalyst particle and the VACNF grows, as seen in Figure 2-3 [33]. Figure 2-3 shows the so-called tip-growth mode, in which carbon precipitates at the bottom of the catalyst particle and causes the particle to lift up from the substrate; the catalyst remains on the tip of the VACNF. The diffusion and precipitation process continues throughout the VACNF growth.

The carbon layers formed beneath the catalyst particle take the shape of the bottom of the catalyst particle (stacked-cup shape) and lead to the formation of a "herringbone" or "bamboo" structure within the fiber. Figure 2-4 (a) shows a TEM image of such a carbon nanofiber. Since the catalyst particle has hemispherical morphology in contact with the substrate before the VACNF growth, the initial formation of carbon layers is parallel to the substrate, as shown in Figure 2-4 [26]. As the VACNF growth continues, the catalyst particle changes its shape and this transformation produces the cup structures. As the VACNF grows further, the cup structures change slowly and eventually reach equilibrium.

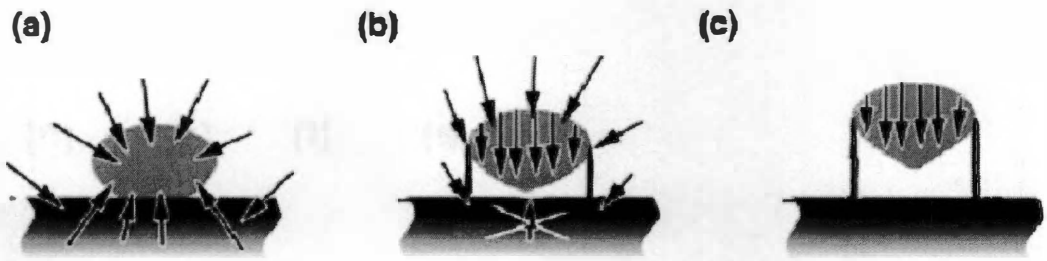

Figure 2-3. Illustration of VACNF growth after the "pre-etching" step. In (a), carbon radicals arrive at the catalyst surface; in (b), carbon diffuses out of the catalyst; in (c), continuation of (a) and (b) leads to the VACNF formation with the catalyst particle at the tip. Reference [33]

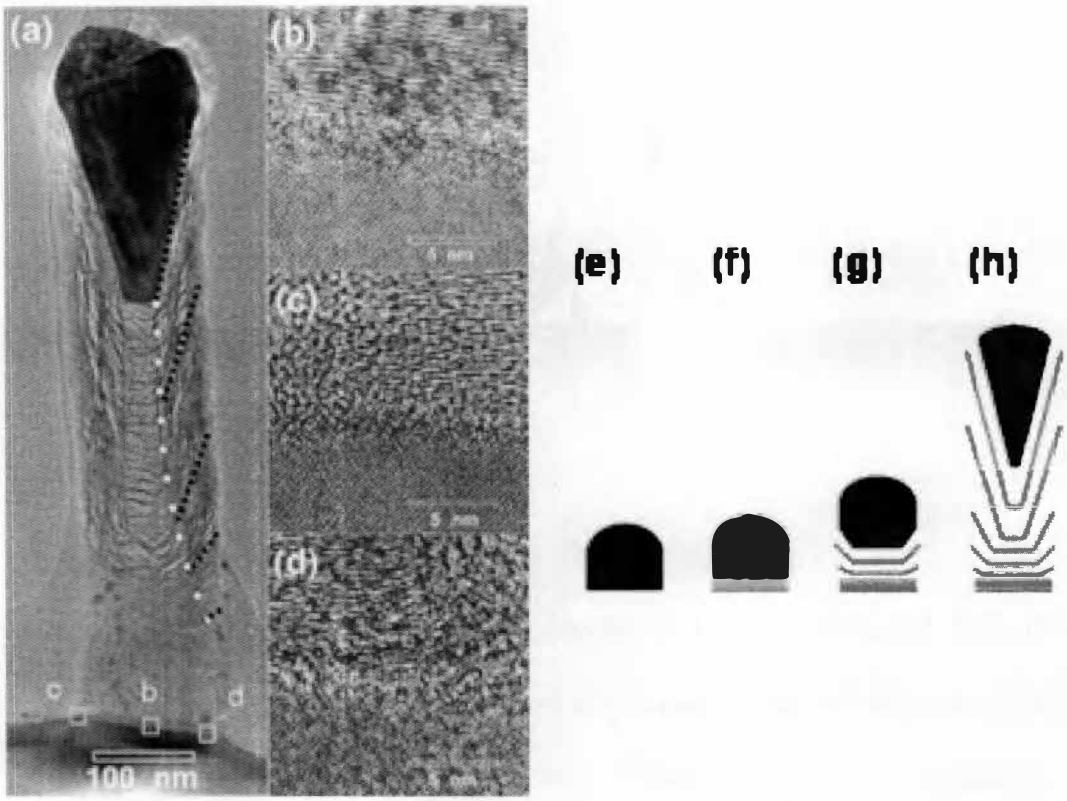

Figure 2-4. TEM images of a VACNF and the initial growth model. (a) Complete TEM images with catalyst and silicon substrate; (b) and (c) and (d) are enlarged images at points b, c, and d on the VACNF as shown in (a). Drawings (e)-(h) illustrate the initial growth of the VACNF – the graphite cup side angle changes as growth continues. Reference [26]

2.1.4 VACNF alignment mechanism

For DC PECVD growth of VACNFs, the growth direction of the carbon nanofibers is controlled by the direction of the electric field at the VACNF location. As shown in the left of Figure 2-5, the electrostatic potential contour around the cathode corners is significant bent. By positioning the sample near the edge on the substrate holder where the electrical field is no longer vertical to the substrate, we can successfully grow VACNFs at different angles with respect to the substrate [34]. The alignment angle is shown to be a function of the distance from the edge. Kinked carbon nanofibers could also be grown by a two-step process through positioning the substrate at different distances from the cathode edge.

Another important factor in achieving vertical alignment is the growth mode [35]. There are two growth modes: (1) base-type, in which the catalyst remains at the bottom of the carbon nanofiber during growth and (2) tip-type, in which the catalyst is pushed up and sits at the carbon nanofiber tip during growth. The directions of base-type carbon nanofibers are usually random, while tip-type nanofibers are vertically aligned (Figure 2-6). A feedback mechanism associated with a non-uniform stress distribution is employed to get an insight into this phenomenon (Figure 2-6). During carbon nanofiber growth, if the carbon nanofiber is bent, the vertical electrical force acting on the carbon nanofiber resulted in a non-uniform stress (part tensile and part compressive) across the interface of the catalyst particle. In the two growth modes, the stresses are distributed in opposite ways. Tensile stress favors carbon precipitation, and higher growth rate is experienced at interfaces experiencing tensile stresses. In the tip-growth mode, the compressive stresses

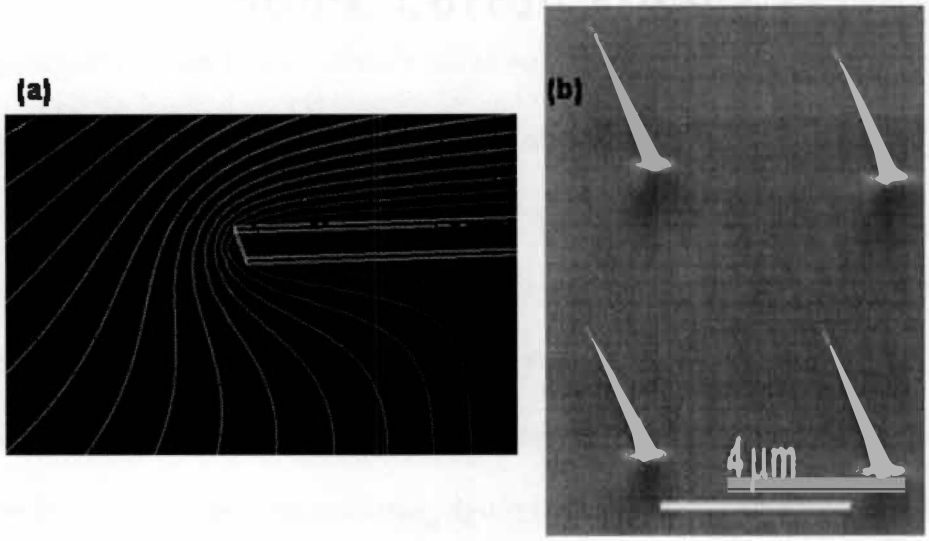

Figure 2-5. Electric field distribution at the sample edge during VACNF growth and the resultant VACNF growth direction. (a) The potential contours around the growth substrate (cathode corners). (b) Off-vertical carbon nanofiber growth results from the bending of the electric field. Figure (b) is adapted from [34].

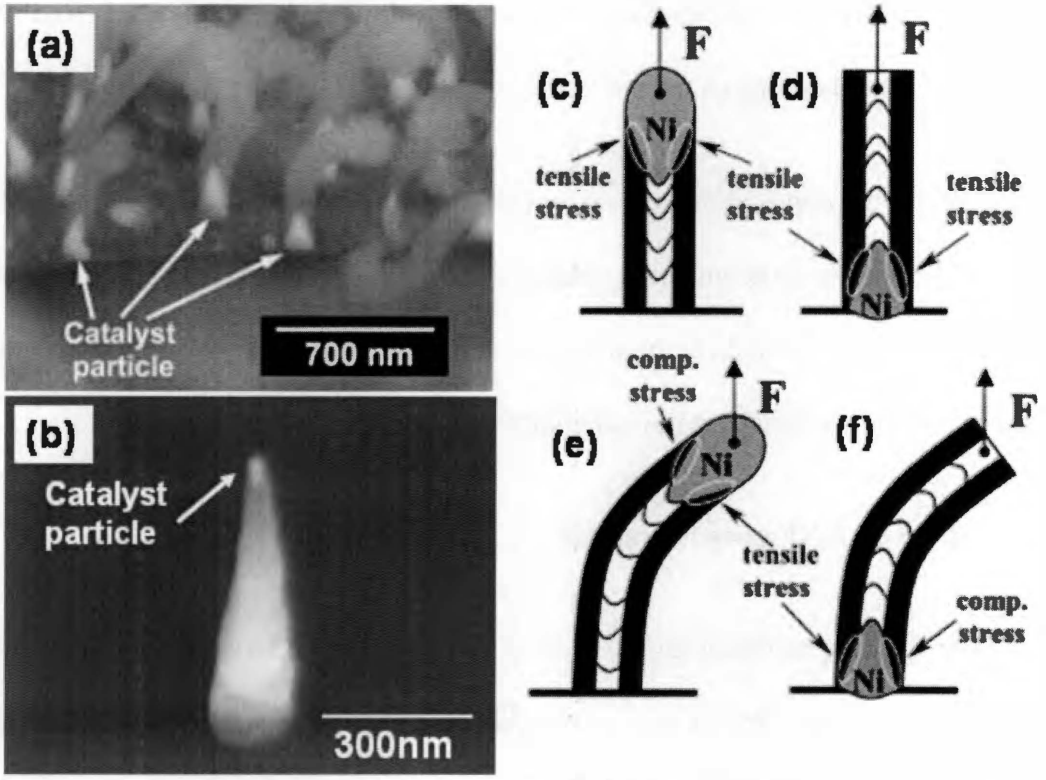

Figure 2-6. Base-type and tip-type growth. Picture (a) shows base-type carbon nanofibers with random directions. Picture (b) is a vertically aligned tip-type carbon nanofiber. Drawings (c) – (f) illustrate the feedback mechanism. ***F*** is the electrostatic force which creates equal tensile and compressive stresses if the carbon nanofiber is parallel to the electrostatic force as shown in (c) for tip-growth and (d) for base-growth. However, if during the growth, the carbon nanofiber starts to bend, non-uniform stresses are created: in (e), tensile stresses are created at lower growth rates; in (f), tensile stresses are created at greater growth rates. Since tensile stresses favor carbon precipitation, greater growth rate is experienced at interfaces with tensile stresses: in (e), growth rate is equalized by this feedback; in (f), growth rate is further imbalanced by this feedback. Reference [35]

are created at greater growth rates and the tensile stresses at lower growth rate, and the feedback equalizes the growth rates and thus maintains a vertical orientation. In the base-growth mode, since the compressive stresses are at lower growth rates, this feedback results in further bending of the structure.

It is thus proposed that the orientation of the carbon nanofibers synthesized by DC PECVD occurs due to negative feedback that requires: (1) the presence of the catalytic nanoparticle at the tip and (2) the direction of the electrical field during the growth process, which is normally perpendicular to the substrate.

2.1.5 VACNF growth control

The structure/morphology of VACNF can be controlled by the growth parameters, such as growth time, catalyst size, plasma power and gas flow ratio. The length of the carbon nanofiber growth is almost linear with growth time. Growth stops when all the catalyst has been sputtered away by the plasma. It is worth noting that an increased C_2H_2/NH_3 ratio leads to decreased growth rate [27]. This implies that the VACNF growth is supply-limited, not diffusion limited.

During the pre-etching step, discrete particles will develop, each of which is responsible for nucleating a single VACNF. The number of particles and particle size can be varied by adjusting the size/thickness of the catalyst, buffer layer material, substrate material or the annealing parameters. Figure 2-7 illustrates catalyst size effects. Besides the catalyst size, the catalyst thickness also plays a role in the number of nanofibers that can be grown from a single dot as seen in Figure 2-8.

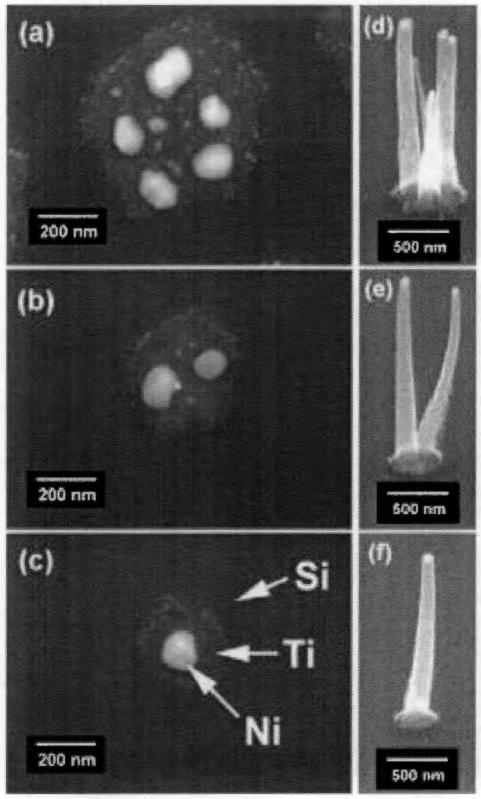

Figure 2-7. The effect of varying the diameter of catalysts. The pictures are taken after the plasma pre-etching process [32]. The Ni catalyst thickness is 15nm. Along with the catalyst sizes reduced from (a) to (c), the number of catalyst nanoparticles is reduced and eventually a single particle is formed.

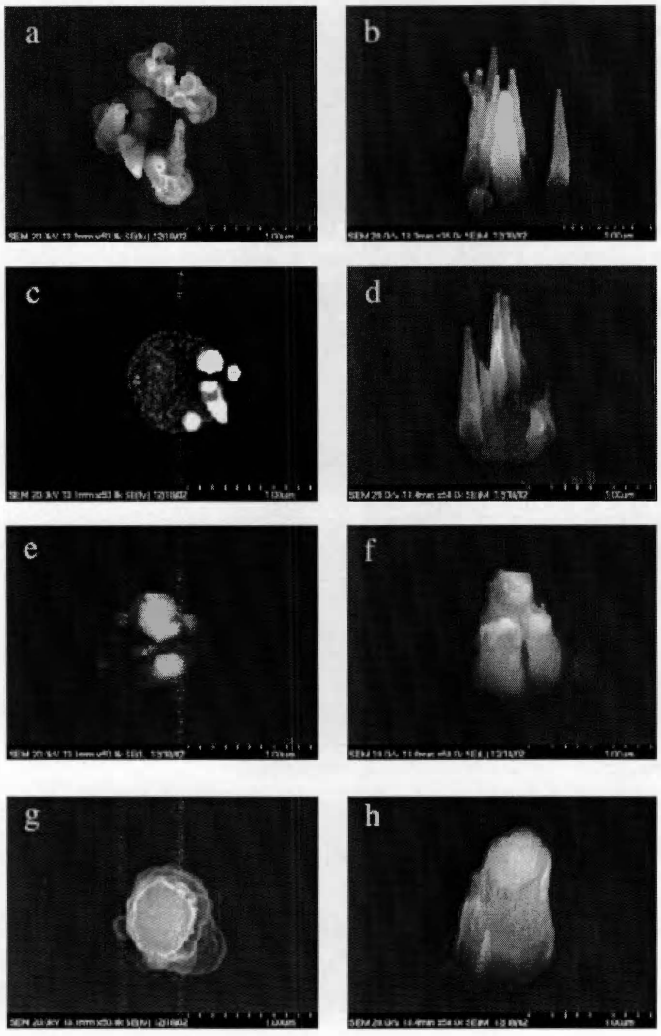

Figure 2-8. Effects of catalyst thickness on the growth of VACNFs. The catalyst diameter is 500nm. The deposited Ni catalyst thickness is 10nm, 40nm, 80nm and 160nm from top to bottom. Along with the increase of catalyst thickness, the average number of VACNFs is reduced and eventually a single VACNF can be grown. [17]

As discussed earlier, the diffusion and precipitation process continues throughout the VACNF growth. Simultaneously, etchant radicals that are present in the plasma eat away the available carbon in the vapor and solid phase. They also serve to etch away the carbon film on the substrate. A relatively higher ratio of NH_3 is needed for this purpose [14]. Under this condition, the substrate (usually silicon) is exposed to the plasma and as a result, the silicon substrate is being sputtered and re-deposited on the sidewalls of the VACNF. The resultant carbon nanofiber thus has a pure carbon core and a Si-N-C containing sheath deposited on the sidewalls of the nanofiber [17].

Conicity of the VACNFs can be tuned by adjusting the ratio of C_2H_2 to NH_3. Cylindrical, conical or cylinder-on-cone shapes can be formed by controlling flows of C_2H_2 to NH_3 as seen in Figure 2-9 [16]. This is hard to understand in terms of conventional thermal CVD process. But in a PECVD growth process, the growth is in two directions instead of one: vertically (similar to thermal CVD) and laterally (precipitation of C from the plasma discharge at the outer walls). As a result, a conical-shape VACNF is formed. By reducing the content of C_2H_2, the cone angle is reduced. Further reduction could lead to the formation of cylindrical carbon nanofibers.

It is also discovered that during growth, bombardment of the catalyst particle by energetic ions gradually removes the catalyst. This reduction in catalyst tapers the tips of VACNFs as a result. An extreme sharp tip is formed if the plasma is turned off at the same time all of the catalyst is removed. Continuation of the growth process without catalyst material will lead to badly-damaged VACNFs (Figure 2-10) [37].

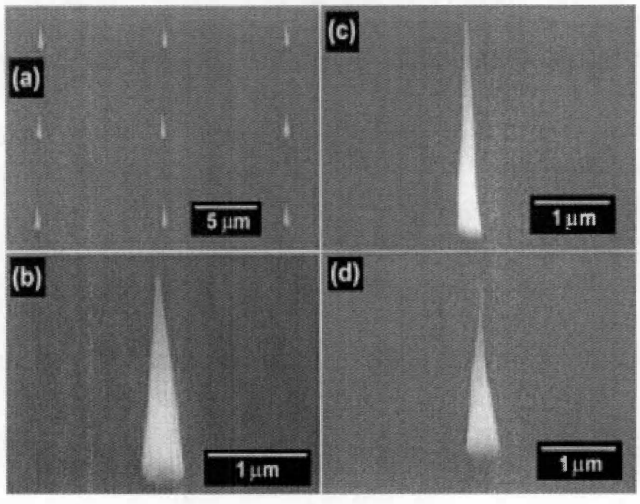

Figure 2-9. Different shapes of VACNFs formed by changing the ratio of C_2H_2 to NH_3. Photo (a) shows an array of VACNFs, while photos (b), (c) and (d) show an individual VACNF under different growth conditions. Photos (b) and (c) have a flow ratio of 60 sccm C_2H_2/80 sccm NH_3 and 55 sccm C_2H_2/80 sccm NH_3, correspondingly. Photo (d) shows a cylinder-on-cone shape synthesized by first growing with 60 sccm C_2H_2/80 sccm NH_3, followed by 50 sccm C_2H_2/80 sccm NH_3. [16]

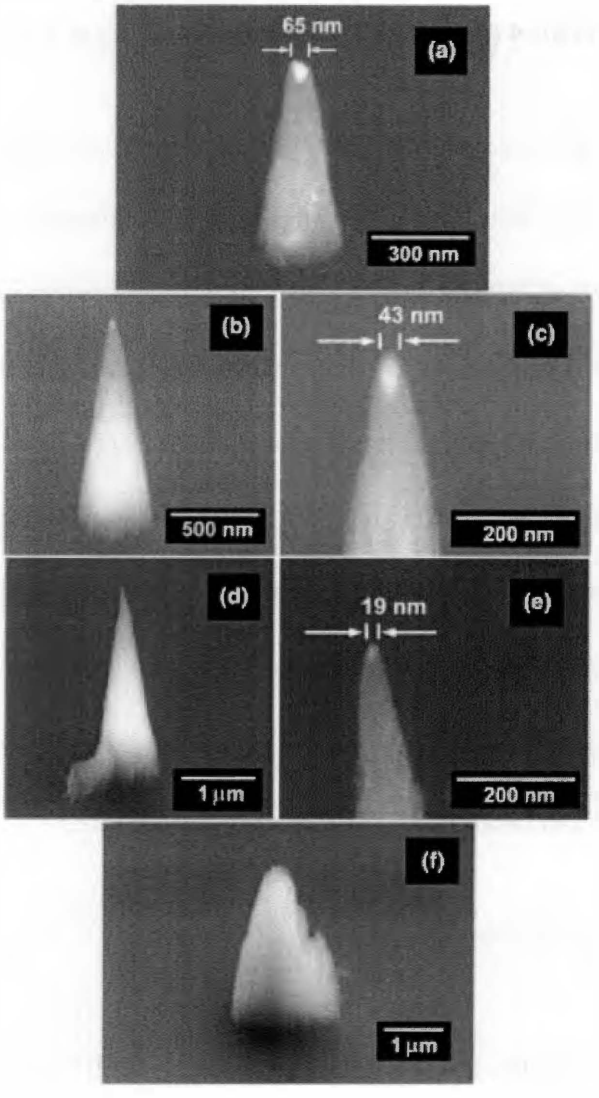

Figure 2-10. Sharpening of the VACNF tips by removing the catalyst material gradually. Growth times of (a), (b)-(c), (d)-(e), (f) are 15 minutes, 30 minutes, 60 minutes and 90 minutes, respectively. The VACNF tips are sharper and sharper along with growth time (a)-(e) before the catalyst is completely removed. After that, the nanofiber is damaged badly (f). [37]

2.1.6 Charge transport properties of VACNFs

Both two-probe and four-probe charge transport measurements have been carried out on individual VACNFs [38]. Four-probe measurement eliminates the contact resistance and is believed to reveal the intrinsic VACNF resistivity. Experimentally, forests of VACNFs with 10μm height are first grown on silicon substrate and then removed by scratching with a needle. The fibers are then dropped onto an insulting substrate (SiO_2 on Si) with alignment marks. Electrodes are then patterned on top of a single VACNF by electron beam lithography (EBL). Following pattern formation, titanium/gold (Ti/Au) are evaporated as ohmic contacts. Four-probe charge transport reveals a linear I-V behavior with an average resistivity of $4.2\times10^{-3}\Omega\cdot cm$. To first approximation, a model can be applied to VACNFs:

$$\rho(\theta) = \rho_a \sin^2\theta + \rho_c \cos^2\theta \qquad (2\text{-}1)$$

where ρ_a is the resistivity parallel to the basal plane ($\rho_a = 4\times10^{-5}\Omega\cdot cm$) and ρ_c is the resistivity perpendicular to the basal plane ($\rho_c = 4\times10^{-2}\Omega\cdot cm$).

This model is based on electrons traveling from one graphitic plane to another and agrees with experimental findings on carbon nanofibers [38]. This result is very different from carbon nanotubes. Charge transport in SWNTs is believed to ballistic [39], while the resistivity of MWNTs are at least two orders of magnitude lower than VACNFs [40]. This difference results from the internal structure difference of CNTs from VACNFs as discussed in section 2.1.1.

Another way to check transport properties is through vertical contacts on in-situ grown VACNFs. In this way, the carbon nanofibers are still attached to the substrate. An illustration of this method is shown in Figure 2-11 [41]. Basically, a dielectric (silicon oxide) is deposited followed by chemical mechanical planarization of the structures. Reactive ion etching is then used to expose the VACNF tips. Metal electrodes are patterned onto the structures. A rectifying junction is discovered by direct current measurements (Figure 2-11). Temperature sweep measurement confirms the junction to be Schottky type and a barrier height of ~0.3eV is extracted. The Schottky barrier usually exists between a metal and a semiconductor. Since the intrinsic VACNF is found to have a linear I-V behavior by four-probe measurements [38], there must be a semiconducting material in contact with the VACNF. Two possibilities exist: the semiconductor is on the top of the VACNF or at the bottom of the VACNF. Titanium/gold (Ti/Au) sits on top of the VACNF and replacement of Ti/Au with other materials of different work functions doesn't affect the I-V behavior. Therefore the semiconductor is at the bottom the VACNF. Further Auger spectroscopic results confirm this supposition and reveal a region of SiC-like material underneath the carbon nanofiber. Thus the Schottky junction occurs between the VACNF and SiC (metal-semiconductor).

This observation is important because VACNFs in most of the applications are still attached to the substrate and this rectifying behavior will have an effect on the overall application. For the purpose of this thesis, VACNFs are used as field emission cathodes and the turn on voltage is above 50V, much higher than the rectifying behavior regime. Thus the rectifying behavior is believed to have negligible effects.

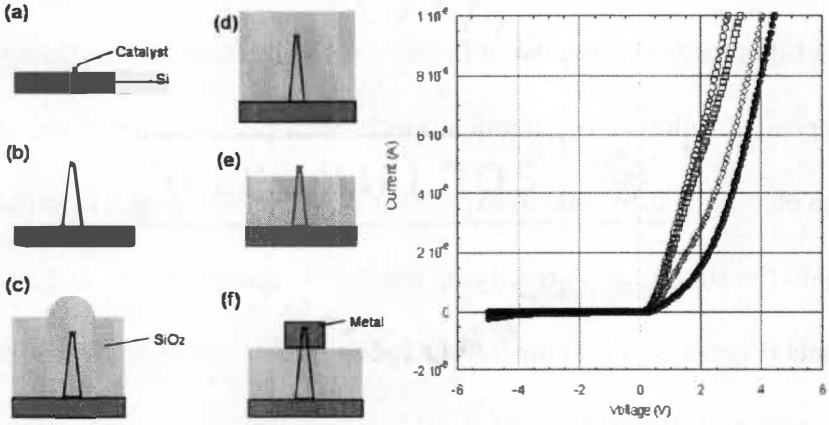

Figure 2-11. Vertical contacts to the nanofibers. Cartoons (a) - (f) on the left illustrate the fabrication method. The I-V curves on the right show the rectifying behavior. Reference [41]

2.2 Deposition of tungsten nanofibers by the Electron Beam Induced Deposition (EBID) technique

2.2.1 Introduction to electron beam induced deposition (EBID)

Electron beam induced deposition is a direct-write technique that has developed rapidly in recent years. Electron beam induced deposition is similar in nature to another direct-write deposition technique called focused ion beam (FIB) induced deposition, but it employs an electron beam rather than an ion beam. Electron beams are capable of being focused into a very small spot size, making them ideal for high-resolution deposition. In addition, implantation/contamination issues inherent to FIB are mitigated by use of an electron beam in the EBID process. These advantages make EBID an attractive alternative to FIB processing and, as a result, EBID has received considerable attention recently.

A modified scanning electron microscope (SEM) can be used for depositing a variety of materials via EBID. The SEM usually has a pump system designed to operate in high vacuum or in variable pressure mode [42]. The SEM is typically fitted with a hypodermic needle-tipped vapor injection system [42], which allows for localized delivery of the precursor gas to the substrate. The injection system is mounted on a wobble stick providing three-dimensional positioning capability and allows for accurate positioning of the vapor injector in order to optimize the directional flow and enhance precursor flux at the surface. Prior to the deposition, the precursor gas is introduced into the chamber and a steady-state flow is achieved. The electron beam is then turned on and

the sample is imaged in the region where deposition is desired. The EBID deposition location can be precisely determined in the SEM, so accurate feature placement is possible. For instance, a nanofiber can be deposited by placing the SEM in point analysis mode which fixes the beam on a single pixel. In the irradiated region, the precursor is decomposed into volatile and non-volatile species. The non-volatile species remains deposited on the substrate, while the volatile byproducts are pumped out.

A variety of materials such as tungsten [42], carbon [43] and gold [44] already have been deposited via EBID. Electron beam induced deposition has found a variety of applications in a variety of applications, such as clear defect lithography mask repair, resistless lithography and three-dimensional nanostructure fabrication.

2.2.2 Use of WF_6 instead of $W(CO)_6$ for the EBID deposition of W nanofibers as the field emission element

Little research has been reported on field emission applications of EBID deposited materials [45-46]. Although Takai and Yavas were successful in obtaining FE test results from EBID deposited platinum (Pt) tip arrays, they employed organometallic precursors. The resultant Pt deposit was highly contaminated with carbon and oxygen and had a much higher C content (73%) than platinum [45]. As a result, the electrical conductivity of the Pt tips was compromised [46].

Tungsten hexacarbonyl, $W(CO)_6$ has been widely used as a precursor for tungsten EBID [42, 47-48]. However, the use of $W(CO)_6$ as a precursor can be problematic as it is a solid at room temperature and requires heating to achieve desirable vapor flow rates.

Consequently, downstream condensation of $W(CO)_6$ was a consistent problem. In addition to the condensation issues, the precursor composition leads to severe carbon and oxygen contamination. Auger analysis showed that the material deposited using $W(CO)_6$ contained atomic weight of 12% tungsten, 70% carbon, and 18% oxygen [42]. A previous report of ion beam-induced deposition of tungsten from WF_6 revealed a deposit composition of 75% tungsten and 25% oxygen, whereas deposited tantalum from an organometallic precursor showed significant carbon and oxygen content [49]. Furthermore, WF_6 is selected for EBID of FE nanostructures because (a) the boiling point of WF_6 is 17.5°C, thus the condensation problems are mitigated, and (b) the absence of carbon and oxygen in the precursor should lead to a higher purity tungsten deposit.

A typical W nanofiber is shown in Figure 2-12 in a gated device structure. For this deposition, the SEM chamber was pumped to a base pressure of approximately 1×10^{-4} Pa before the introduction of WF_6 to a pressure of $\sim 8\times10^{-3}$ Pa. The estimated local pressure was 0.8Pa which corresponded to a vapor flux of $\sim 7.1\times10^{21}\, m^{-2}s^{-1}$ according to capillary flow data and analysis [50] of a similar injection system [51]. After determining the tungsten EBID rate, emitters were deposited in the gated apertures using a 20kV accelerating voltage and a beam current of ~33pA. The working distance was ~14.1mm and the deposition lasted between 60 and 90 seconds at 30,000× magnification in point analysis mode. The resultant W nanofiber was ~1μm tall and 40nm wide with tip diameter of less than 15nm.

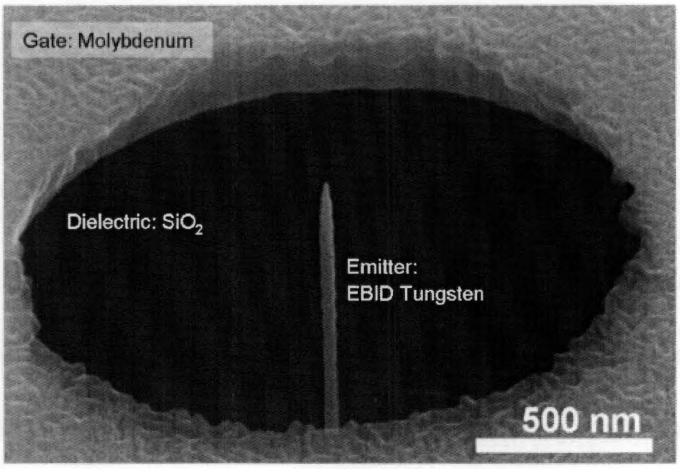

Figure 2-12. A typical W nanofiber by EBID in the gated device.

Chapter 3

Field emission properties of the active nanostructures

3.1 Theory of field emission

Field emission (FE) is defined as "the emission of electrons from the surface of a condensed phase into another phase, usually a vacuum, under the action of high (0.3-0.6V/Å) electrostatic fields" [52]. Extensive studies of FE from both metals and semiconductor materials have been carried out [52]. Since FE from nanofibers is the main concern of this thesis and VACNFs and EBID W nanofibers are metallic as discussed in the last chapter, the discussion below is limited to FE from metallic materials only.

In metals, there is a potential barrier called work function, Φ (usually 2-6 eV), corresponding to the electron energy difference between the Fermi surface and a field-free vacuum near the surface. Under the application of high electric fields, the potential barrier between the Fermi surface and the vacuum is deformed so strongly that electrons have a finite probability of leaking through it — this is called field emission. As can be seen, field emission is closely related to the quantum tunneling process.

The potential of an electron situated at a distance, z, from an infinite conductive surface is given by the "image" potential [53]:

$$\phi_{image} = -\frac{e^2}{16\pi\varepsilon_0 z} \tag{3-1}$$

where e is the elementary charge and ε_0 is the permittivity of vacuum. With the applied electrical field, E, the potential of the electron is given by

$$\phi = -ezE + \phi_{image} = -ezE - \frac{e^2}{16\pi\varepsilon_0 z} \tag{3-2}$$

This is shown in Figure 3-1. The dashed line labeled "No Field" denotes ϕ_{image}. The solid line labeled "With Field" shows the electron potential (equation 3-2) with the applied field. As can be seen from the figure, the barrier becomes deformed and is lowered by

$$\Delta\phi = \left(\frac{e^3 E}{4\pi\varepsilon_0}\right)^{1/2} \tag{3-3}$$

An expression of the emitted current as a function of applied field can be obtained by quantum-mechanical tunneling calculations. The expression is commonly referred to as the Fowler-Nordheim equation [54]:

$$I = \frac{e^3 E^2 \alpha}{8\pi h \phi t^2(y)} \exp\left[\frac{-8\pi(2m)^{1/2}\phi^{3/2}}{3heE} v(y)\right] \tag{3-4}$$

where α is the emission area in cm^2, h is Plank's constant, m is the electron mass, and $y=\Delta\Phi/\Phi$, and $t(y)$ and $v(y)$ are the Nordheim elliptic functions.

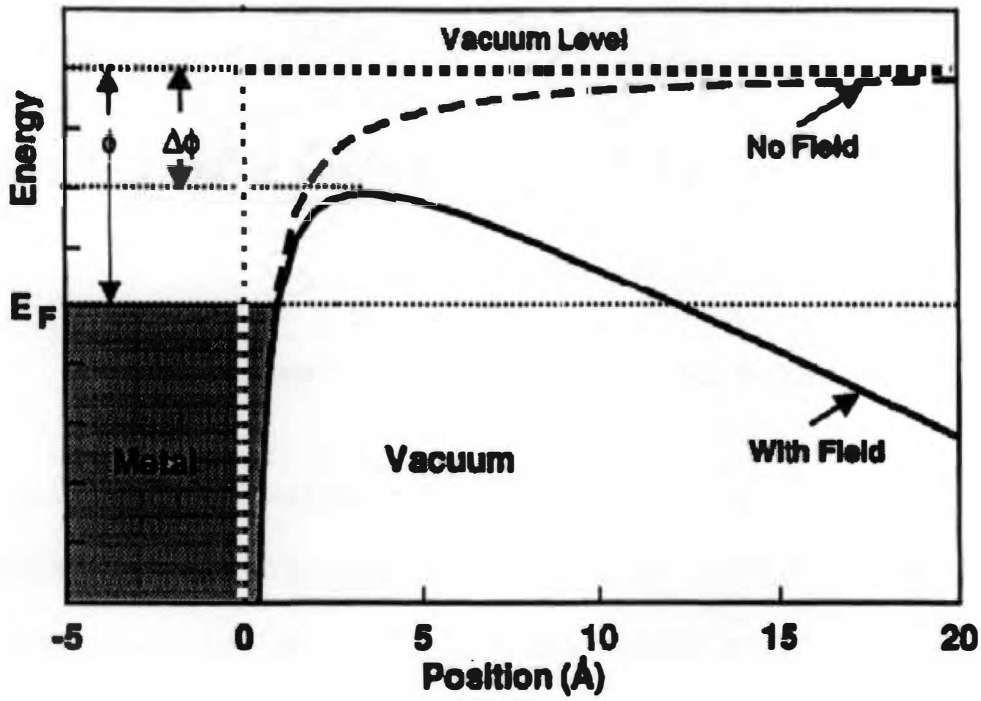

Figure 3-1. Band diagram drawing in the process of field emission from a metal. The dashed line denotes the potential, ϕ_{image}, of an electron without applied field. The solid line denotes the potential, ϕ, of an electron with applied field. The potential barrier has been lowered by $\Delta\phi$ in the presence of the electrical field. [53]

To first order, $t^2(y) = 1.1$ and $v(y) = 0.95\text{-}y^2$. So the Fowler-Nordheim equation can be further simplified into

$$J = \frac{I}{\alpha} = \frac{AE^2}{\phi} e^{9.89/\phi^{1/2}} e^{-B\phi^{3/2}/E} \qquad (3\text{-}5)$$

where $A = 1.5\times10^{-6}$, $B = 6.4\times10^{7}$, α is the emission area, ϕ is in eV, E is in V/cm, and J is in A/cm ^{2}.

3.2 FE properties of carbon nanofiber related materials

As early as the 1970s, carbon fibers were explored as FE electron sources [55–57]. These fibers were ~10μm wide with ~0.5μm sized tips and were discovered to have a high brightness and a high current density [55-57]. Beyond that, the carbon fiber source can run continuously in ambient gas pressure for more than 100h without any sign of breakdown, thus making possible the operation of field emission electron guns in conventional vacuum systems. It was found that operation pressure could be as high as 10^{-4} Pa without catastrophic failure, although pressure-dependent noises were observed.

In 1991, carbon nanotubes were discovered [58]. Along with the elevated interest in many other properties of carbon nanotubes, FE of single and multi-walled carbon nanotubes also becomes an area of intensive investigation [59]. Carbon nanotubes are good candidates for field emission because they are highly conductive, chemically and mechanically stable, and have very high aspect ratios (micrometer-sized length versus nanometer-sized diameters). Turn-on fields as low as 1 V/μm are reported for carbon

nanotubes due to high geometric field enhancements. The energy spread of field emitted electrons is only ~ 0.12 eV [60]. Furthermore, a field emitted electron beam from carbon nanotubes is coherent [61].

The emission brightness and current density are also investigated for carbon nanotubes [59, 62]. Emission currents as high as a few μA can be extracted from an individual nanotube. The brightness values obtained from individual multi-walled carbon nanotubes are an order of magnitude larger than the state-of-the-art commercial sources [62].

Another important aspect of carbon nanotube field emission is the low vacuum requirements. Carbon nanotubes have a long operation life [59] and can operate in relatively low vacuum. There are similar pressure-dependent noises as discovered for carbon fiber materials [55-57]. Higher vacuum and elevated temperature heating/baking can help stabilize the beam considerably [62]. The main challenge for carbon nanotubes to be applied in electron gun application is the ability to synthesize arrays of isolated individual high-quality carbon nanotubes.

3.3 Field emission properties of VACNFs

In contrast to carbon nanotubes, arrays of isolated individual high-quality VACNFs can be deterministically synthesized as discussed in Chapter 2. This is one of the superior qualities of VACNFs making parallel FE cathodes application feasible.

Merkulov first investigated the FE properties of VACNFs using a movable probe technique [15]. The FE measurements were taken by applying a positive voltage to a 1μm anode probe and measuring the field-emitted electron current to the probe. Once an emission site was determined, a FE current versus applied electric field (I-E) curve could also be obtained (Figure 3-2). The curve demonstrated Fowler-Nordheim behavior, indicating tunneling of electrons.

The turn-on field for sparse VACNF forests is around 15-30 V/μm as reported. In addition, emission site density, or spatial distribution of emission currents at a constant electric field, was also investigated by Merkulov. Similar results were reported later and confirmed Merkulov's work [63]. Dense VACNF forests are not suitable for field emission applications because relatively high turn-on electrical fields are usually needed (>50V/μm) and arcing is observed.

A detailed investigation of individual VACNFs were first reported by Baylor [18] using the same movable anode probe configuration described earlier [15]. The inter-fiber distance in this study has been increased so that emission current from only a single VACNF is observed. It has been shown that 50μm or larger inter-fiber spacing is needed (Figure 3-3). The anode probe to substrate distance is also carefully chosen to result in negligible field enhancements at neighboring VACNFs. The macro-electric field needed to extract 1nA current from a single VACNF is 12-60 V/μm depending on the geometry of the VACNF studied. I-V characteristics of the field emission from isolated VACNFs typically follow Fowler-Nordheim behavior. Isolated VACNFs have displayed stable emission for over 175 hours (the longest period of test) of continuous 10 nA operation at

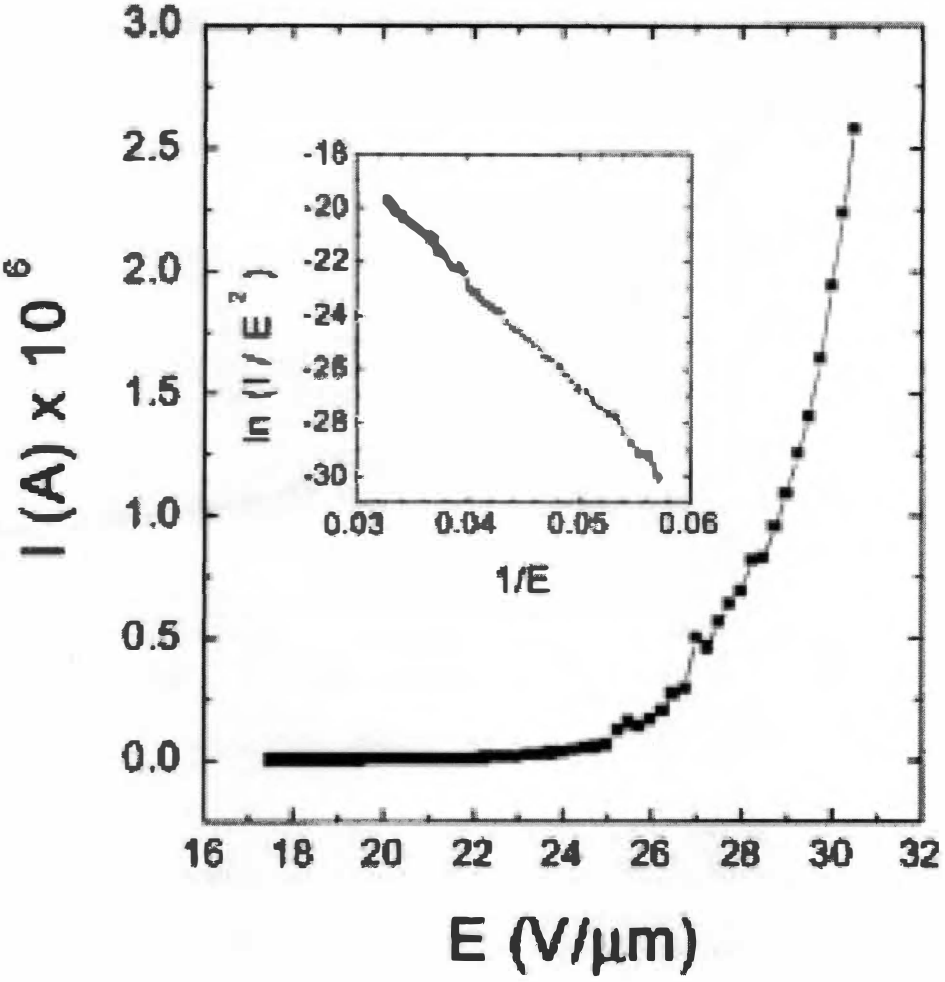

Figure 3-2. An emission current versus applied electric field (I-E) curve and Fowler-Nordheim plot (inset) obtained from a forest of VACNFs. From reference [15].

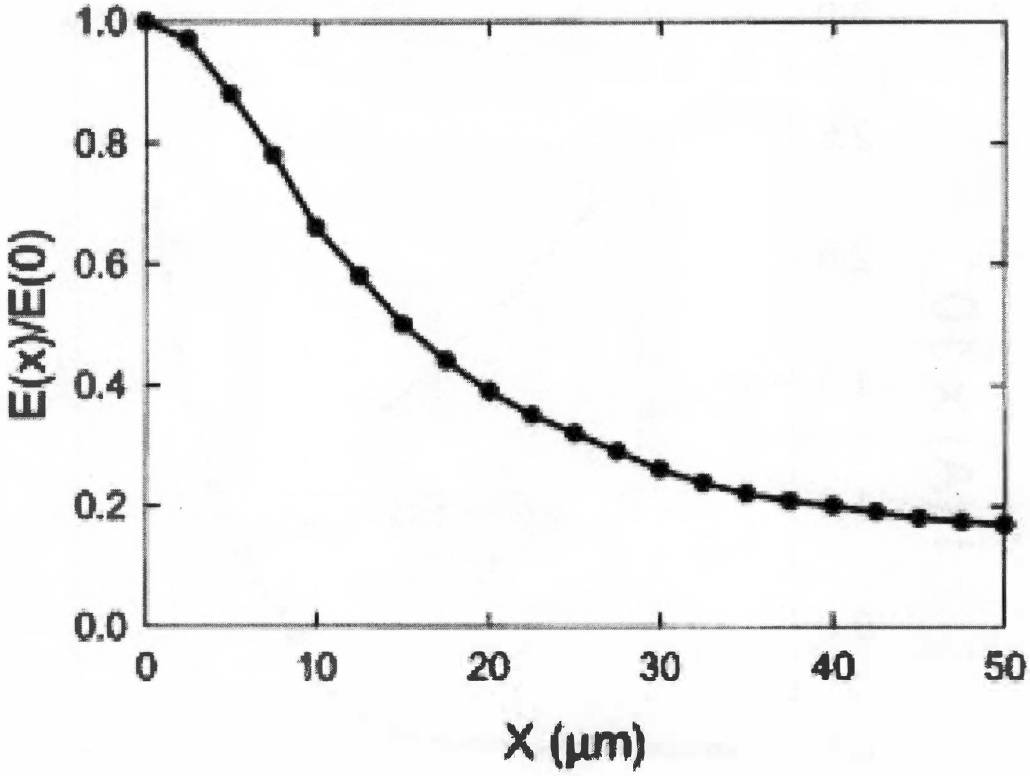

Figure 3-3. A plot of the calculated electric field at the substrate as a function of the lateral distance away from the anode probe. The probe height is set at 10 μm. The field is normalized to the field directly under the probe [18].

vacuum levels of 10^{-6} torr. FE current versus voltage (I-V) analysis has shown a maximum measured FE current exceeding 5 μA without any degradation to the VACNF tip. It was also shown that nanofibers that have been reactive-ion etched showed no degradation in the morphology or field emission. In fact, the field emission is typically enhanced as a result. Resistance to reactive-ion etching allows further integration of these VACNFs for more complex devices.

Semet and coworkers examined FE behavior of VACNF separated by 100μm using similar techniques [64]. This work confirmed the above results from Baylor. This paper also pointed out the effects of adsorbates on the VACNF field emission behaviors that will be discussed later in this chapter.

3.4 Adsorbate effects on VACNF field emission behavior

There are two general kinds of adsorption on solids – physical adsorption and chemical adsorption. Physical adsorption is non-specific and occurs on all solids with all gases. There is only weakly attractive van der Waals-type forces between solid and gas molecules. Chemical adsorption, on the other hand, corresponds to chemical bonding and the act of adsorption due to chemical reaction. Both chemical and physical adsorptions play a role in the FE behaviors.

The phenomenon of adsorbate molecules on the field emission behavior has been observed since the 1940s and many of the details are covered in the early textbook by

Gomer [52]. Field emission microscope/micro-channel plate has been used to study surface diffusion and various gas adsorptions [52].

Resonance tunneling behavior of field-emitted electrons through adsorbates has been investigated and documented by a few authors [65-67]. Chemisorbed molecules lying on the surface of a metal produce bonding states which form energy levels a few angstroms off the metal surface (Figure 3-4). These surface states create a resonant tunneling condition for electrons, and thus greatly increase the local tunneling current at the molecule [66].

Dean and coworkers reported the first field emission microscopy observation from single walled carbon nanotubes [68]. The observed field emission images contained one to four lobes (Figure 3-5). The lobed patterns observed from the nanotubes are essentially identical to those patterns commonly produced on metals by adsorbate atoms and molecules [67]. Under normal vacuum and surface conditions, the chemisorbed tunneling states appear to dominate nanotube emission at room temperature. In their experiments, they initially heated the sample to a temperature of 1800K in an ultra high vacuum under high electrical field conditions. When the temperature exceeds 900K, the current drops by an order of magnitude and the lobed emission patterns disappear. Field emission patterns showing atomic resolution from clean nanotubes are obtained by rapid cooling to room temperature at this condition. Dean's work on carbon nanotubes has been confirmed and detailed [69-70].

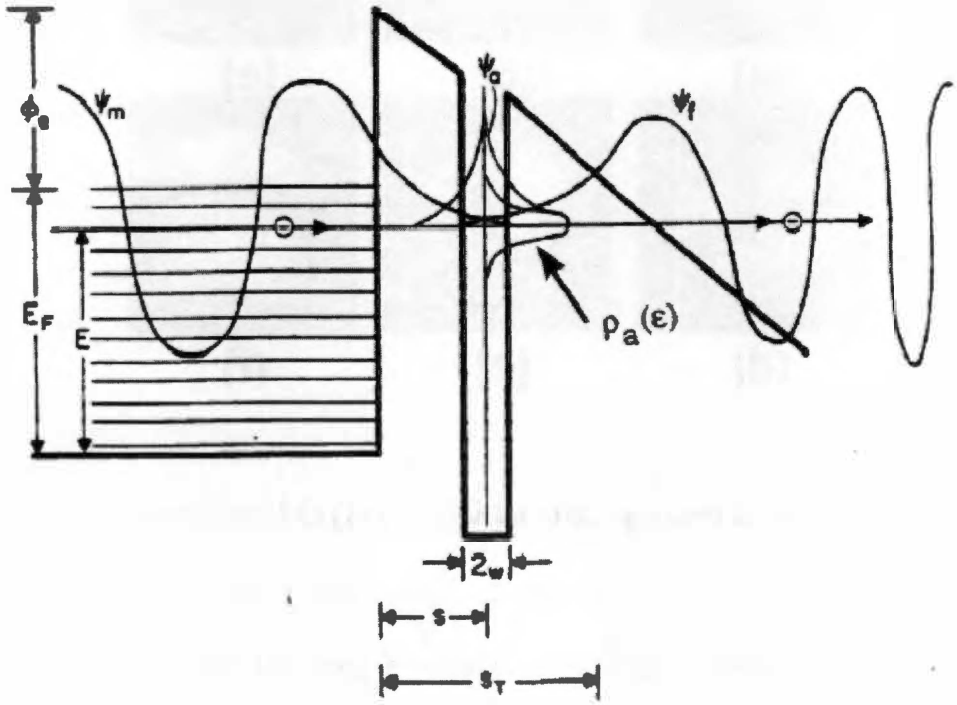

Figure 3-4. Schematic drawing to illustrate the principle of field emission resonance tunneling. The electron wave functions are: ψ_m, the unperturbed metal function; ψ_a, the localized adsorbate resonance function; and ψ_f, the emitted electron function. The adatom centered at z =s, with diameter equal to 2w, with a local density of states labeled ρ_a [66].

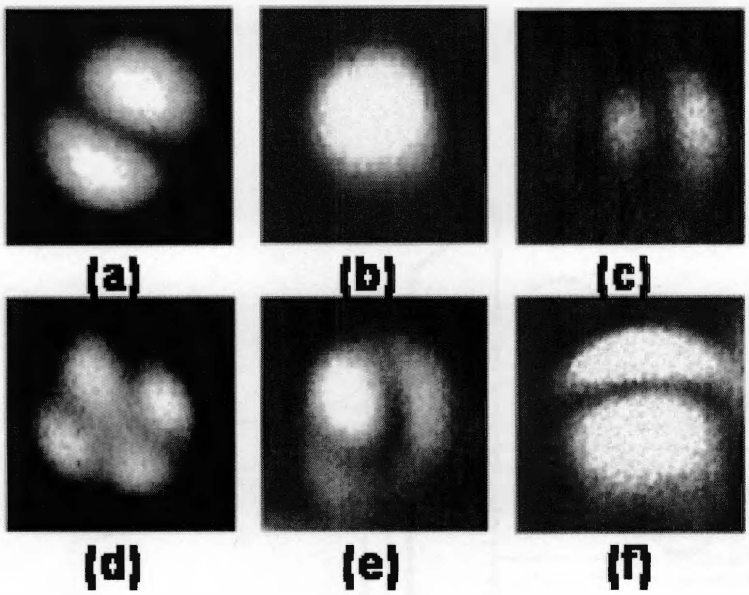

Figure 3-5. Field emission patterns with one to four lobes from carbon nanotubes at room temperature. The tilted versions of the symmetrical lobed patterns can be seen in pictures (d) – (f). Modified from reference [68].

Semet and coworkers [64] examined the adsorbate effects on VACNF emission. Before conditioning, the emission current was extremely unstable and the I-V characteristics displayed current saturation, an effect related to the diffusion and loss of tunneling state as characterized for carbon nanotubes [70]. The conditioning procedure was conducted in UHV using high levels of emission current (from 0.1μA to 1-5 μA) to locally heat the VACNF tip. At large currents, the temperature at the VACNF tip became so high that desorption of the adsorbate molecule occurred. The current dropped at a fixed field as expected after conditioning.

Properties of adsorbate effects on VACNFs are studied in detail at Oak Ridge National Laboratory [71]. Field emission from VACNF usually requires a low turn-on electric field, which is generally attributed to its high aspect ratio. However, numerical simulation results based on the same VACNF and measurement parameters employing the Fowler-Nordheim equation (equation 3-5) predict an emission current that is at least 100 times lower than experimentally obtained current, or, in other words, enhancements from geometry enhancement alone is not enough to account for such a low experimental turn-on electric field. It is thus suspected that resonance tunneling plays a role in the VACNF FE behaviors.

By increasing the macroscopic electric field, the current displayed step-like behavior along with the general exponential increase, as shown in Figure 3-6. Also hysteresis is observed in I-V curves (refer to the green arrows for different voltage sweep directions). This behavior was also observed for carbon nanotube field emission behaviors [70] and the steps were attributed to the adsorbate emission fluctuation. In this

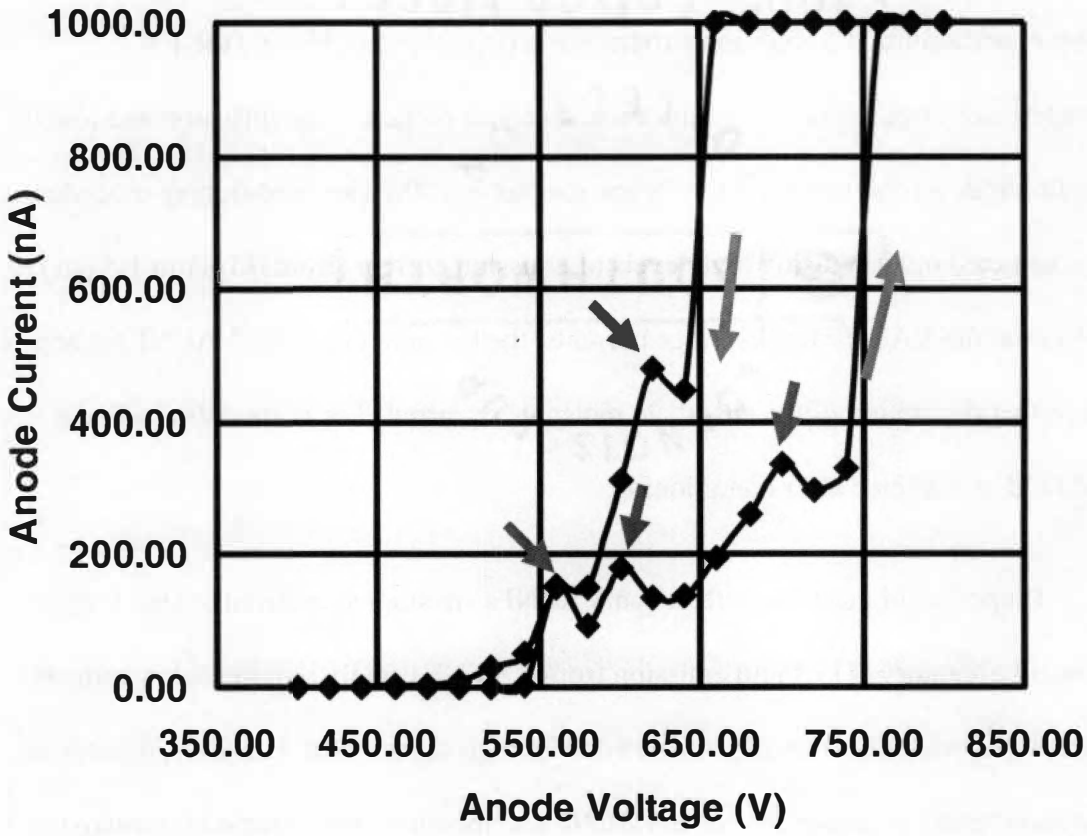

Figure 3-6. Field emission I-V curves obtained from VACNFs showing steps and hysteresis. The anode to substrate distance is approximately 12μm. The green arrows indicate the voltage sweep directions. The red arrows point to the appearance of the steps.

article, it was also shown that the hysteresis was also related to adsorbate emission and was absent in a clean emission. The current from adsorbate molecules is limited, also leading to the observation of current saturation in carbon nanotubes [70].

The electron beam image on the phosphor image was stable at low currents (this is important for electron beam lithography for the accuracy of writing). When currents are increased beyond 1μA, the beam changes its shape and position (as shown in Figure 3-7). This means that the adsorbate field emission is perturbed; possibly, current from a particular adsorbate molecule is saturated and the high local electric field results in displacements of adsorbate into a different configuration or triggers field emission from other adsorbate molecules. A detailed image evolution at different emission current levels was reported by Guillorn *et al.* [71].

Field emission energy distribution is also very important in understanding FE behaviors. The energy distribution of the emitted electrons is also important in the derivation of the noise characteristics of field emission cathodes and the resolution of the scanning electron field emission microscope.

Both the total energy distribution and the normal energy (normal to the emission surface) can be calculated by integration over the Fermi-Dirac distribution function. The total energy distribution is more important because it can also be measured experimentally. A theoretical curve of the total emission energy distribution at 0K is plotted on the top of Figure 3-8.

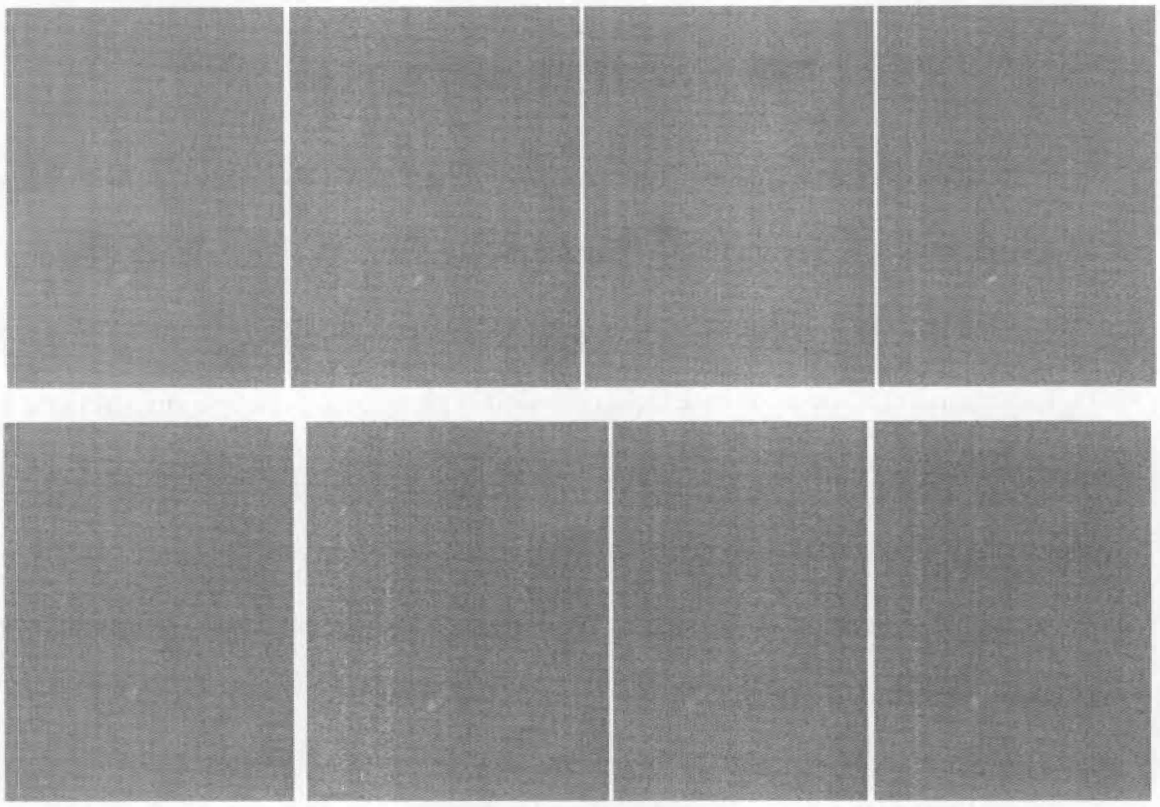

Figure 3-7. Optical observation of the electron beam evolution on the phosphor anode. The electrons are located near the bottom of the pictures. These images are obtained using a regular digital video camera so the resolution is limited.

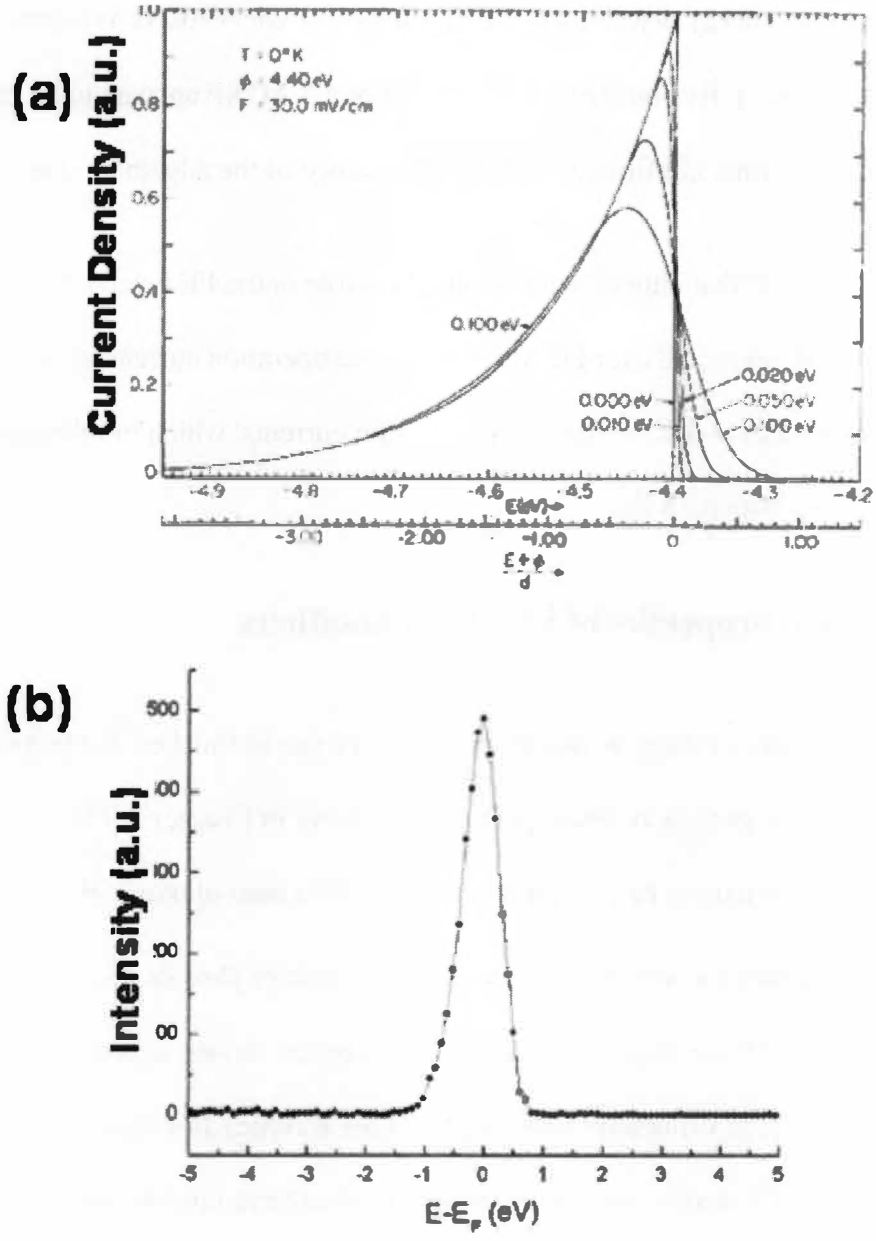

Figure 3-8. Field emission energy distribution (FEED). Picture (a) shows the theoretical FEED from a free-electron metal at 0K for different analyzer widths [16]. Picture (b) shows the FEED spectrum obtained from a VACNF at 100nA in a gated structure [72].

Field emission energy distribution (FEED) from a single VACNF is plotted on the bottom of Figure 3-8 [72]. By comparison, the FEED of a VACNF appears to be more symmetrical. This is further confirmation of the appearance of the adsorbate state [73].

It is worth noting that although adsorbate plays role in the FE behavior, EBL is not affected. For EBL, especially for DEAL concept, the operation current is very low. A stable emission pattern is discovered at low emission currents, which in lithography leads to a clear, sharp patterned line.

3.5 Field emission properties of EBID W nanofibers

The investigation of these W nanofibers is carried out in finished single-gate devices. The deposition process is discussed in detail earlier in Chapter 2. FE measurements were carried out in a vacuum chamber with a base pressure of $<5\times10^{-5}$ Pa. The electrons were collected by a 1-inch diameter phosphor screen anode 6.7mm away from the device chip. The gate electrodes on the device were wire-bonded to a custom-made package using aluminum wires. Three Keithley Instruments model 2400 direct current (DC) source-measurement units were used in this measurement and were connected to the cathode, gate, and the anode individually to provide independent measurement and control of each terminal. In this work, the gate was grounded and the anode was set at +1000V potential. The cathode was biased from –60V to –250V. Figure 3-9 illustrates the typical FE measurement setup. Prior to the deposition of W nanofibers, a typical device structure was first packaged and tested to determine the leakage current and noise level. The leakage current between the cathode and gate electrode in the device

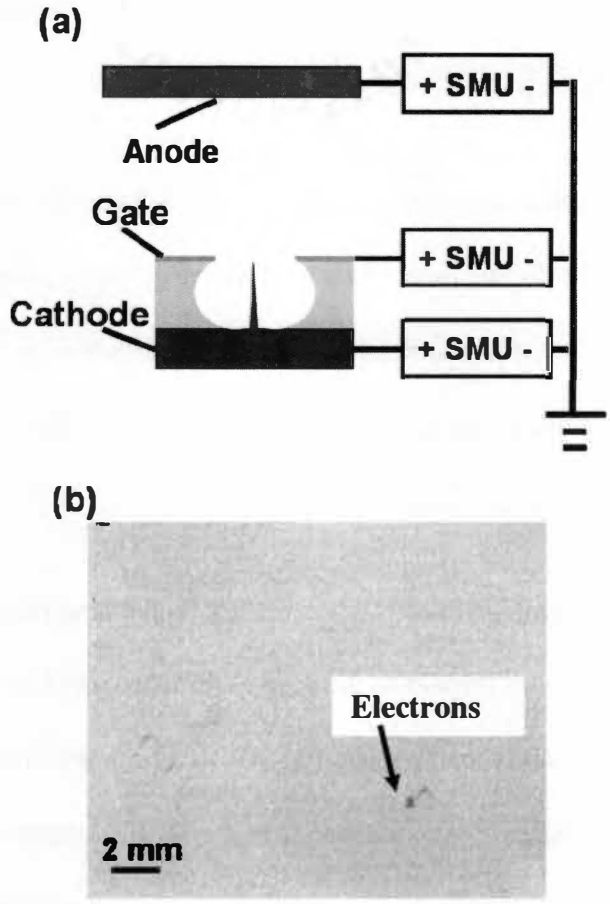

Figure 3-9. Field emission instrument setup and a typical electron image on the phosphor anode. (a) Setup of the measurement. All three source measurement units are grounded together. Drawing is not to scale. (b) Electron beam images on the phosphor anode. The total emitted current is around 1μA. The images were recorded using a color digital video camera. The images were inverted followed by contrast adjustment.

structure was less than 1nA up to 250V. The noise level on the anode was also less than 1nA at 1000V.

The emitted electrons collected on the phosphor anode were continuously captured using a color digital video camera. The images were transferred to a computer and inverted. Following image inversion, only brightness and contrast of the images were adjusted to enhance visual effects. No further image processing was applied. A typical image is shown in Figure 3-9 (b).

The threshold voltage (defined for this test as the amount of negative voltage biased on the cathode with respect to the gate required to yield 20nA of current), V_{th}, was initially around 130V, and then dropped to ~90V within a few minutes. A drop in threshold voltage or increase in emission current after FE initiation has been previously observed and reported in similar devices [74]. The threshold voltage after initiation (~90V) is similar to other devices reported [23], considering the 2.5μm diameter aperture size. The high initial value of V_{th} (~130V) is possibly due to contamination of the W tips in air. Due to the wider aperture opening (2.5μm diameter), the emission current collected by the gate is minimal (<5%).

A DC current-voltage (I-V) curve was obtained by sweeping the cathode voltage and recording the current collected by the anode. Figure 3-10 (a) shows a typical I-V curve and the associated Fowler-Nordheim (FN) plot (Figure 3-10 (a) inset). The anode current shows a reasonably linear fit when plotted in FN coordinates, consistent with the

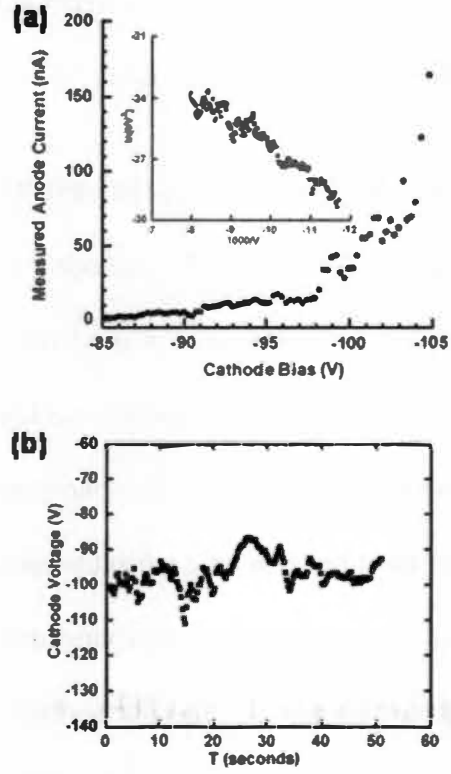

Figure 3-10. Field emission current-voltage and stability curves obtained from a W cathode device. (a) A field emission I-V curve of a single gated W nanofiber cathode. Inset: the measured anode data plotted in Fowler-Nordheim coordinates. (b) The threshold voltage at 40nA current as a function of time measured at 3×10^{-5} Pa vacuum level. The emission is somewhat noisy, possibly due to low vacuum or lack of cleaning of the W nanofiber tip.

cold field emission process. It is also worth noting that a current as high as a few μA can be extracted from a single 15nm W tip without device failure.

Time dependence of the cathode voltage required to emit 40nA current is also plotted in Figure 3-10 (b). It has a noisy behavior as the cathode voltage fluctuates ±10% around -100V. This noise is partly due to the operation in moderate vacuum conditions [62]. Although the voltage (or current) amplitude appeared to be fluctuating, the observation of the electron beam spot evolution on the phosphor anode indicated that this electron beam spot was constant in position with time when the cathode operates in a constant-current mode. As the total emission current was changed dramatically (by an order of magnitude), the electron beam spot on the phosphor anode would shift in position and/or change in brightness. This happens more frequently at high currents. This is an indication that as current changes, both emission position from the W tips and the total emission area are varied. This variation will result in blurred/distorted lines in the electron-beam writing as proposed by Baylor *et al.* [12]. Fortunately this change in emission area is not observed at low emission currents (<40nA). This is because at low electric fields, only a limited emission area can be activated. For massively parallel EBL applications [12], the devices are operated at low emission currents (<20nA), so the emission area can be assumed to be constant. Furthermore, a dose control circuit can be employed [12] so that the current magnitude fluctuation can be mitigated.

Chapter 4

Electron-beam focusing characteristics of double-gated VACNF based field emission devices

This chapter is highly modified from a paper submitted to *Journal of Vacuum Science and Technology B*.

X. Yang, W. L. Gardner, L. R. Baylor, H. Cui, D. H. Lowndes, D. C. Joy and M. L. Simpson. "Electron-beam focusing characteristics of double-gated carbon nanofiber based field emission sources".

For this paper, I carried out numerical simulations and contributed most of the writing.

4.1 The need for numerical simulation investigations

Although dual-gate structures have been successfully fabricated and characterized [23], there are many aspects concerning the device design that must still be investigated. For the device to be used as an electron source, one concern is the depth of field (DOF) of the resultant design. DOF is usually defined as the range of working distance (WD) within which the lens is in focus, or in this study, within which the electron beam spots are still relatively sharp. In practice, DOF is usually defined as the range of WD for twice the minimum beam size. For example, if the minimum beam size for a particular system is 10nm at WD=100μm, and the beam size reaches 20nm at both 95μm and 103μm, then for this system, DOF=103μm-95μm=8μm. DOF reflects how sensitively the beam focusing responds to a change in WD or focus potential, and is an important factor to produce sharp lithographic lines.

Another aspect of the design that needs investigation is the thickness of the electrode. Currently, both electrodes are fabricated by electron-beam evaporation and the electrode is only ~150nm thick. There should be an advantage to using thicker electrodes because the gradients in the electrical field coupled through each aperture are smaller. Because this gradient changes sharply near the aperture walls, reducing the gradient results in better focusing performance and larger DOF. The quantitive responses of different electrode thicknesses should be investigated by numerical simulations.

In the fabrication of VACNF based dual-gate structures [23] using both lithographic and non-lithographic methods, the resolution of the lithography tools, the tolerance of the self-aligning process, and the shift of the VACNFs with respect to the predetermined locations during growth all contribute to imperfections in the alignment of the structures. It is thus important to investigate quantitively these effects on the beam trajectories and more importantly on the resultant beam shape at the collecting surface.

4.2 Numerical simulation techniques are widely employed in scientific research

Use of numerical techniques for investigation of electron optics design yields very productive results. In the vast reports of FE study of different materials, test setup is usually different, such as the size and type of the anode probe, and the anode-cathode distance over which the test is carried out. These factors may affect the final quantitative FE results, such as the turn-on electric field, the emission current density, etc. Some of these effects are discussed by Nicolaescu *et al.* using electrostatic simulation codes [75].

The results indicate that the emission behavior for small anode probes is similar to that for large/flat anodes and it is derived that, as a practical rule, the ratio of the probe anode diameter to the anode-emitter spacing should exceed 2 for consistent emission results with large anodes. In Bonard *et al.* [76], numerical simulation supplements their experimental results in the understanding of FE current density optimization by adjusting the carbon nanotube film density.

Garcia *et al.* carried out detailed electrostatic two-dimensional modeling [77] on integrated field emission nanotips along with their experimental characterization. One of the most important findings is that for the integrated field emission nanotip structures, the best emission geometry is to have the gate electrode on the same level as the nanotips. Effects of misalignments and double tips are also investigated here.

Nicolaescu *et al.* carried out quite a number of electrostatic modeling on different geometries [78-80]. In one of his papers [79], he reported a very detailed investigation on device misalignment effects on the electron beam focusing and deflection properties of volcano-shaped dual gate silicon tip emitters. Their results indicated that although beams were deflected due to misalignment, a focused beam could still be obtained.

4.3 Integrated Engineering Software (IES) — Lorentz 2D and 3D

For this study, Lorentz 2D and 3D software packages from IES are employed. These software packages specialize in the boundary element method (BEM) for solving Laplace's equation and determining electric charge distribution [81-82].

The boundary element method is based on an integral formulation toward the solution of Laplace's equation [81]. There are three types of boundary conditions that are generally encountered in solving Laplace's equation (The following example is for 2D case only).

(1) Dirichlet, the value of the function is known on the boundary,

$$\Phi(\vec{r}) = \int_{\partial B} G(\vec{r},\vec{r}\,')\sigma(\vec{r}\,')dr' \qquad (4\text{-}1)$$

in which $\Phi(\vec{r})$ is the value of the potential at $\vec{r}$ on the surface, $\sigma(\vec{r}\,')$ denotes the charge density on the surface, and $G(\vec{r},\vec{r}\,')$ is the Green function:

$$\nabla^2 G = -\delta(\vec{r}-\vec{r}\,') \qquad (4\text{-}2)$$

$$G(\vec{r}-\vec{r}\,') = -\frac{1}{2\pi}\ln|\vec{r}-\vec{r}\,'| \qquad (4\text{-}3)$$

(2) Neumann, the normal derivative of the function is known on the boundary,

$$\Phi'(\vec{r}) = \int_{\partial B} G'(\vec{r},\vec{r}\,')\sigma(\vec{r}\,')dr' + \frac{\sigma(\vec{r})}{2} \qquad (4\text{-}4)$$

in which $\Phi'(\vec{r})$ denotes the derivative of the potential, $\sigma(\vec{r}\,')$ denotes the charge density on the surface, and $G'(\vec{r},\vec{r}\,')$ is the derivative of Green function.

(3) Mixed boundary of Dirichlet and Neumann, often encountered at the interface of two medium materials with dielectric constant ε_1 and ε_2:

$$(\varepsilon_1 - \varepsilon_2)\int G'(\vec{r},\vec{r}\,')\sigma(\vec{r}\,')dr' + (\varepsilon_1 + \varepsilon_2)\frac{\sigma(\vec{r})}{2} = 0 \qquad (4\text{-}5)$$

Once the charge distribution can be derived to satisfy the three types of boundary conditions, we can relate potential anywhere in the space to the charge density distribution through integration.

There are two other kinds of numerical techniques: finite difference method (FDM) and finite element method (FEM) [81-82]. The finite difference method utilizes a truncated Taylor series expression and the differential operator is then discretized at each grid point. It is easy to implement, but usually results in poor accuracy, low speed and poor presentation of the boundaries. The finite element method is targeted to minimize the total electrostatic (or magnetostatic) energy stored in a region. The region is covered with non-overlapped and non-separated sub-areas, called elements. Element geometries and unknown quantities are expressed by polynomials with nodal values as coefficients. Minimization of the total energy gives solution at the nodes. The finite element method is very commonly used and highly developed.

The boundary element method is believed to be superior to both FDM and FEM. First, it is based on an integral formulation, which in numerical simulation is a more favorable approach than discretizing a differential operator. In BEM, elements are only placed on the boundaries, so it is easy to set up a model, especially a model with open-regime problems. The boundary element method is also the best choice to deal with models with extreme ratios between the smallest and largest details. The smallest detail

usually sits at an isolated location and the element distribution can be easily tuned, independent of the rest of the model. Finally, ray-tracing results are very accurate since the field and potential distribution in space are derived from the actual charge distribution on the boundaries. The boundary element method is indeed verified to be accurate in solving Laplace's equation and ray tracing [81-82].

4.4 Lorentz 2D model set-up

The VACNF emitter geometry is modeled as a hemispherical tip on a conical section with height of 800nm, tip radius of 15nm, and base radius of 200nm. The extraction and focus electrode have aperture openings of 1.5μm and 3.6μm, respectively. Both the extraction and focus electrode have the same thickness of 100nm unless otherwise specified. The dielectric thicknesses are kept at 1μm. The working distance (WD) from the collecting anode (which simulates a semiconductor wafer being patterned) to the base plane, where the nanofiber sits, is set at 100μm, unless otherwise specified. The baseline geometry of the model, excluding the target anode plane, is shown in Figure 4-1.

The carbon nanofiber and the base plane are set at ground potential. A voltage of +90V is applied to the gate/extraction electrode. At this condition, the total emitter current is on the order of 0.1 pA. The focus electrode potential is adjusted to achieve smallest spot size at the collecting electrode. The collecting anode has a potential of +1000V unless otherwise specified.

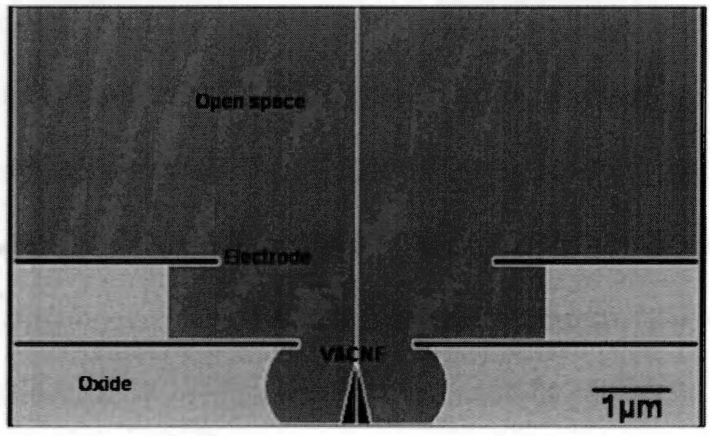

Figure 4-1. The full 2D simulation model geometry with materials assigned. The dark region is vacuum, the light region is SiO_2 dielectric, and the black region is assigned as "exterior". The drawing is to scale with the scale bar in the drawing at 1µm.

A relative permittivity of 3.8 and conductivity of 1×10^{-17} mho/m is assigned to the SiO_2 dielectric. Neumann boundary conditions are assigned to the outer cylindrical boundaries of the free space and dielectric regions to mimic the effects of an extremely large radial extension of these areas.

For the trajectories, an adaptive fifth order Runge-Kutta integration algorithm is used with an accuracy of 1e-4. This algorithm is similar to constant time-step algorithms, but with the ability to determine the time-step size within the minimum and maximum time settings in a self-adaptive fashion. Minimum and maximum steps are set to 0.1 *fs* and 200 *fs* or smaller. These settings are tested against smaller time steps, and the change in results is found to be negligible. Launch energy of 0eV is assumed. Emission angles are normal to the nanofiber tip surface and all electrons are assumed to be emitted from an area within 9° of the axis of symmetry. This angle is consistent with preliminary experimental findings.

4.5 2D Simulation results

The 2D models are cylindrically symmetrical around the emitter axis. An example of electron trajectories is shown in Figure 4-2 for three different focusing conditions: (a) under-focused, (b) optimal-focus, and (c) over-focused. The full geometry as shown in Figure 4-2 is for illustration only. The simulation only requires geometry layouts in half of the plane along with the designation of the rotation axis. With a potential of V_f =+9V on the focus electrode, the trajectories are divergent everywhere (Figure 4-2 (a)).

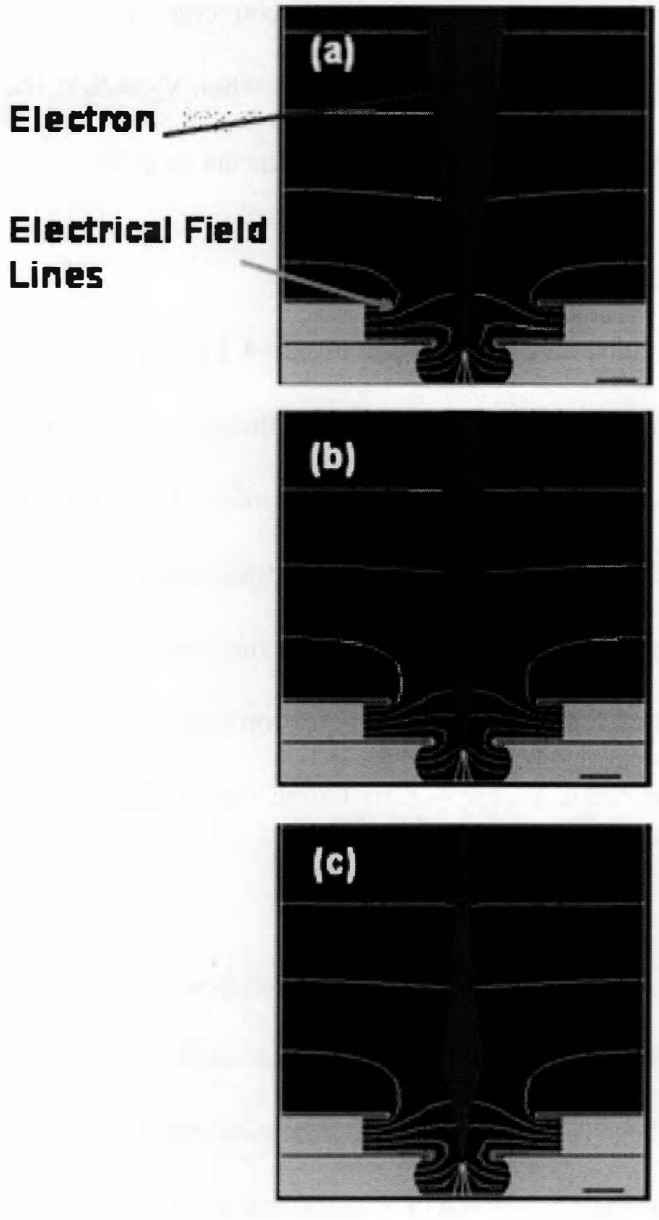

Figure 4-2. Three focusing conditions under different focus potentials. (a) Under-focused, spread-out beams; (b) optimal-focus, collimated beams; (c) over-focused, the beam crosses over and diverges. The scale in the picture is 1μm.

When V_f =-21V, they appear slightly convergent and actually converge to a beam diameter of ~50nm at the anode plane (Figure 4-2 (b)). Finally, when V_f =-26V, the trajectories become over-focused and once again divergent at the anode plane (Figure 4-2 (c)).

Depth of field simulation curves are presented in Figure 4-3 (a) by varying the position of the anode plane with three different sets of focus voltages. As the WD increases, the trajectories come to focus and then eventually defocus. The beam radii are determined as being the radial extent within which 50% of the trajectories fall, because the electron density on the outer area of the anode is much less than those near the center of the anode, due to the annular area represented by each electron trajectory. The effects of the counting methods are illustrated in Figure 4-3 (b). Curve trends similar to Figure 4-3 (a) are observed.

Depth of field indicates a range of WD for which electron beam spots are relatively sharp. If we define DOF as the range of WD with $2d_{min}$ around the minimum beam size d_{min}, a DOF value of ~5μm is derived for these dual gate structures from Figure 4-3 (a). This relatively small value may be related to the small change in the electrical field gradients when the anode plane is moved, since the anode plane is always set at a constant potential (1000V), as in our experiments. The DOF results with fixed electrical field gradient are shown in Figure 4-3 (b). Note that the slight electrical field gradient change plays a significant role in the resultant beam spread.

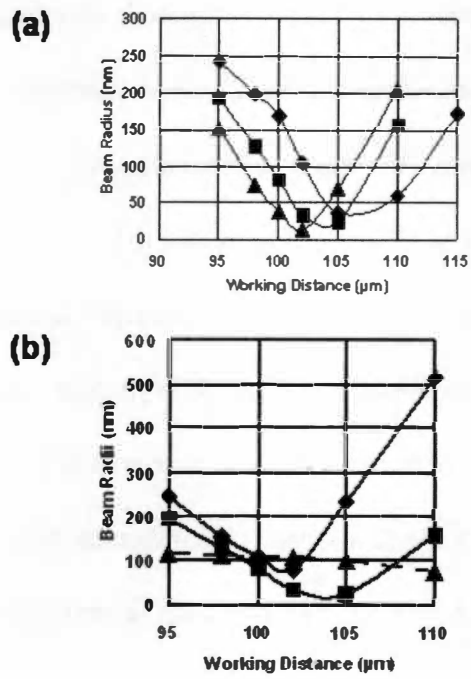

Figure 4-3. 2D depth of field simulation results. (a) Depth of field curves at three different focusing potentials (triangle denotes $V_f = -21.8V$, square denotes $V_f = -21.5V$, diamond denotes $V_f = -21V$). In all cases, the trajectories could be converged by varying the focus potentials. (b) Depth of field curves with different simulation methods. Diamond denotes method of counting 100% beams, square denotes method of counting 50% beams. The DOF curve obtained by fixing the electrical field gradients is denoted by the dotted line with triangles.

Different electrode thicknesses are also investigated: 100nm, 200nm, and 500nm. In these models, the dielectric thicknesses and the electrode aperture diameters are kept the same as stated before. A similar "V" shape of beam sizes versus WD curves is observed for all three thicknesses as shown in Figure 4-4 (a), indicating trajectories focusing and defocusing. However, the curves shift to the right as thickness increases. This shows that less optimal-focus potential is needed for thicker electrodes. Also, there is noticeable change in the slopes of the "V" shapes, as shown in Figure 4-4 (b): the thicker electrode has a relatively smoother slope. This indicates that the DOF can be improved by employing thicker electrodes. The optimum beam radius is also reduced for thick electrodes.

Our modeling results are presented using specific choices of a variety of parameters. The effects of changing some of these parameters on the final trajectory tracing and spot diameter have been discussed by Nicolaescu *et al.* [77]. An example of beam radii change is presented in Figure 4-4 (c) for a set of electron initial energies from 0 eV to 0.3 eV. Notice the beam radii increase as the initial energy increases. With a close look at the trajectories, we find that this is mainly due to a change of focus. The trajectories can be re-converged by adjusting the focusing potential by less than 0.5V. However, actual cold field emitters have emission energy spreads of ~0.3 eV [77]. This distribution of electron energy is estimated to cause further broadening of the beam by ~50%.

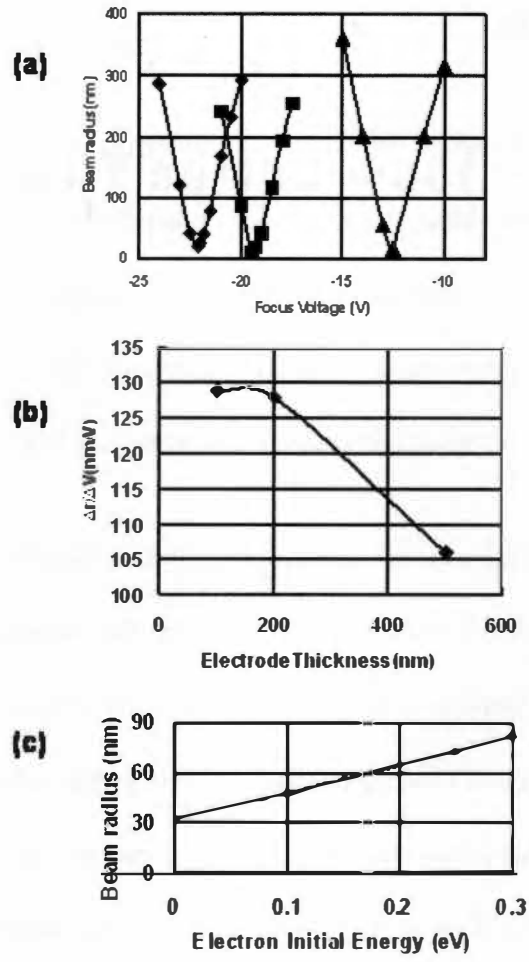

Figure 4-4. 2D simulation results of electrode thickness effects and the initial electron energy effects. (a) Beam radii plotted as a function of focus potential for different electrode thicknesses (diamond denotes 100nm, square indicates 200nm, triangle indicates 500nm). (b) The changes of beam radii per applied focus voltage were plotted as a function of electrode thickness. The thicker electrode has better depth of field as indicated by the decrease of $\Delta r/\Delta V$. (c) Beam radii as a function of electron initial energy. The trajectories can be re-converged by increasing the focus potentials.

4.6 3D modeling results

A 3D model of well-aligned rotationally symmetrical structures is constructed and the visualization of the beam shape on the anode is presented in Figure 4-5 (a). The contour plot is constructed by counting the number of electrons falling in a small area on the anode plane. For the same geometry as in 2D model, a well-focused beam with a diameter of only 20nm can be observed with a focus potential of around -22V.

Lorentz 3D is especially useful for studying the misaligned dual-gate VACNF based structures since rotational symmetry can no longer be assumed for these models. In the process developed by Guillorn *et al.* [23], the first electrode is formed by a self-aligning process and the second electrode is defined lithographically. The focus electrode offset may be significant due to two factors. The first is due to nanofiber migration from its predetermined catalyst location during the growth. This would not affect the extraction electrode since it is self aligned, but would affect the focus electrode alignment significantly because it is registered to the alignment marks on the wafer, thus only registered to the predetermined carbon nanofiber locations. The second is that, even with precise location of the VACNF, the focus electrode may suffer some misalignment due to the limited alignment precision of our lithography tool. The misalignment of VACNF would also play a role in the resultant device behavior considering the accuracy of self-aligning.

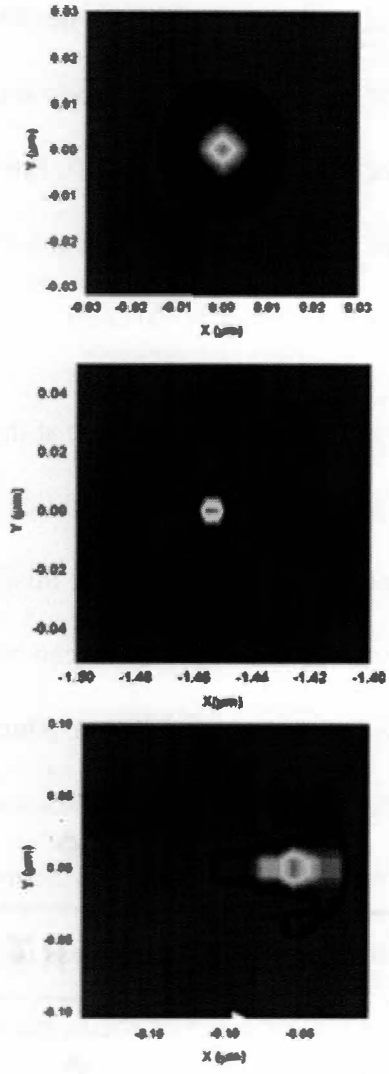

Figure 4-5. The electron beam shape at the anode for a no-misalignment and misaligned structures. (a) For a no-misalignment structure. (b) For a focus-electrode shift of 100nm from the center. (c) For a carbon-nanofiber shift of 10nm from the center.

Figure 4-6 (a) shows trajectories launched from an "ideal" structure, in which no offsets exist, and the trajectories are well collimated along the device axis. Figure 4-6 (b) shows trajectories launched from a structure with focus electrode shift, and Figure 4-6 (c) shows trajectories launched from a structure with VACNF shift. For cases (b) and (c), deflection of the trajectories is observed as a result of structure misalignment, and deflection is in the opposite directions of each other in (b) and (c).

For EBL, the most important concern is the beam shape at the anode, which represents the writing plane. This will affect the writing capabilities and resultant minimum feature size. Examples of well focused beams for the misaligned structures are shown in Figure 4-5 (b) and (c). A very small and well-converged beam is observed even for the maximum shifts studied: 100nm focus electrode shift or 50nm VACNF shift, although astigmatism and coma-type aberrations will increase somewhat from these misalignments. Optimal-focus potential for these misaligned structures may differ by as much as 1V. When compared to perfectly aligned structures, less focus potential is needed for VACNF-shifted structures to achieve optimal-focus, but slightly more potential is needed for the focus electrode-shifted structures to achieve optimal-focus. The Lorentz 3D simulation software proves to be very useful for specifying alignment tolerances for the fabrication of actual emitters for a commercial lithography tool.

A summary of the beam shift amounts when the focus electrode or VACNF is misaligned is shown in Figure 4-7. The ratio of beam shift to nanofiber offset is ~10:1, while the ratio of beam shift to focus electrode offset is ~15:1. The simulation results differ from a simple electron optics calculation: the structure is on the order of 2μm and

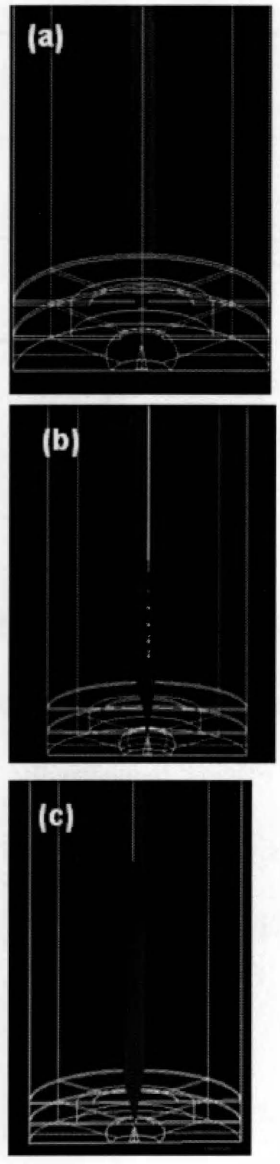

Figure 4-6. 3D modeling geometry with electron beams. (a) For the no-misalignment case; (b) for the shifted focus electrode case; (c) for the shifted nanofiber case. The beam shifts were in the same direction as the electrode shift, but in the opposite direction as the nanofiber shift.

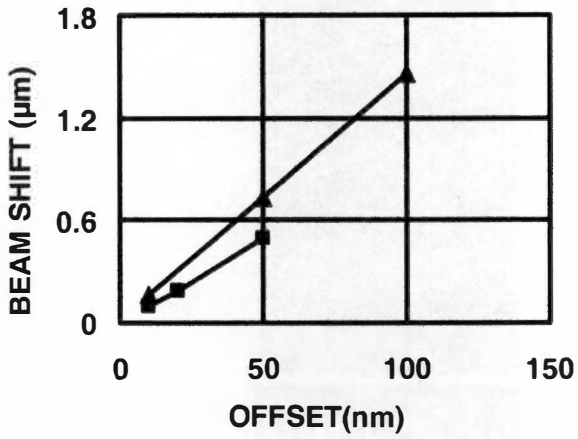

Figure 4-7. The electron beam shifts as a function of nanofiber or focus electrode shift. The triangle and square corresponds to focus electrode offsets and nanofiber offsets, respectively. The ratio of beam shift to nanofiber offset is ~10:1, while the ratio of beam shift to focus electrode offset is ~15:1.

considering the working distance is 100μm, 50:1 magnification in shift should be a first linear approximation. The beam radial position at the anode does not depend significantly on the focusing potential when the focusing voltage is within 0.5V of the optimal focus voltage. When the focusing potential differs significantly from the optimal focus potential, the beam spot is not well defined due to being out-of-focus.

Our contour plot in Figure 4-5 only shows the resulting images of the emitted electrons, or aerial images. Diffraction effects from the apertures on the resultant beam are not considered. To consider diffraction effects, we first calculate the Abbe Limit $\frac{\lambda}{\alpha}$, where λ is the electron wavelength and α is the beam convergence semi-angle, as calculated earlier. For 1000 eV electron energies, the wavelength is ~0.4Å, yielding an Abbe limit of ~6nm. Because this number is considerably smaller than the beam spot size, diffraction effects are not important. The actual EBL feature size may also differ from simulation results obtained from this paper due to electron penetration and scattering in the resist [83-84].

Another aspect of the device performance is the effect of having a semiconductor material as the field emitter. As discussed, the software is capable of assigning materials with different dielectric constants. However, field emission involving semiconductors needs to be investigated from the very beginning of the quantum tunneling process (tunneling not through a Fermi sea of free electrons) and the validity of Fowler-Nordheim equation is questioned. The investigation of semiconductor field emission is beyond the capability of the simulation softwares.

In conclusion, systematic simulations of VACNF-based, dual gated electron beam device focusing characteristics are investigated and discussed. It is shown that thick electrodes will enhance the focus behavior beyond that achieved with thin electrodes in terms of the focusing effectiveness, optimal focused beam size, and depth of field (DOF). The optimal focus voltage decreases and the nominal beam radius reduces for thick electrodes. The beam radius change per applied voltage also drops when electrode thickness increases from100nm to 500nm, indicating improvement of DOF. 3D modeling of the structure misalignment shows encouraging results for the devices to function as well focused electron sources, especially for electron beam patterning.

This simulation results warrants further research in the dual-gate field emission devices. In the next few chapters, several device design and fabrication efforts are discussed to improve on the current device design and minimize the device misalignments.

Chapter 5

VACNF based FE structures with individual cathode addressability

5.1 Individual cathode addressability is an essential part of DEAL concept

As introduced in Chapter 1, the DEAL concept offers a high throughput EBL system by taking advantage of using multiple field emission sources in parallel [12]. One important aspect of the design is to use logic, memory and control circuits that consist of logic shift registers that can control each emitter individually. This in effect replaces the conventional mask and is essential for any maskless lithography. The control part of the LMC has a dose-control circuit (DCC) for a controlled electron dose delivery. The DCC circuits terminate the electron emission at a fixed dose rather than a fixed time and thus accounts for emission noise and non-uniform operation over time. In order to record the dose and terminate the emission according to the dose delivered from each individual emitter, the circuits need to be connected to each emitter separately.

Dual-gate VACNFs-based field emission structures have been fabricated [23] and initial lithography was successful using these emitters [85]. For these structures, there are four terminals: the cathode, the gate, the focus and the anode. The gate electrode is used to turn the field emission on or off; the focus electrode is used to adjust the electron beam focus. However, in the device structure, the electrons are extracted from the cathode and accelerated towards the anode. Neither the gate electrode nor the focus electrode sees any

of these electrons under normal operation. Also, the anode is a resist-coated sample in actual lithographic writing. The DCC circuits cannot be integrated to it for control of millions of individual emitters. Therefore, the cathode is the only terminal for use of the integration of DCC circuits.

5.2 Design of individual cathode addressable field emission devices

For the existing dual-gate structures [23], carbon nanofibers are grown on n-type low-resistivity Si wafers using the native oxide as the buffer layer. The carbon nanofibers are thus electrically connected to each other through the Si substrate, as shown in Figure 5-1. In order to isolate VACNFs from one another, the immediate thought is to grow them on an insulating substrate. However, there exist two major problems with this idea. First, growth on an insulating substrate is not feasible in a direct current (DC) PECVD system. As discussed in Chapter 3, the yield of secondary electrons from nonconductive substrates is usually insufficient to sustain the plasma discharge. A possible solution to this problem is to perform radio-frequency (RF) PECVD growth of VACNFs. Indeed, VACNFs can be possibly synthesized this way [86-87]. However, a RF PECVD system is not readily available at this time. Possible means to get around the non-conductive substrate are preferred. Secondly, the bottom of carbon nanofibers still needs to be electrically addressed so electric fields can be applied to extract electrons from the VACNFs. There is no easy way to electrically address VACNFs grown on an insulating substrate.

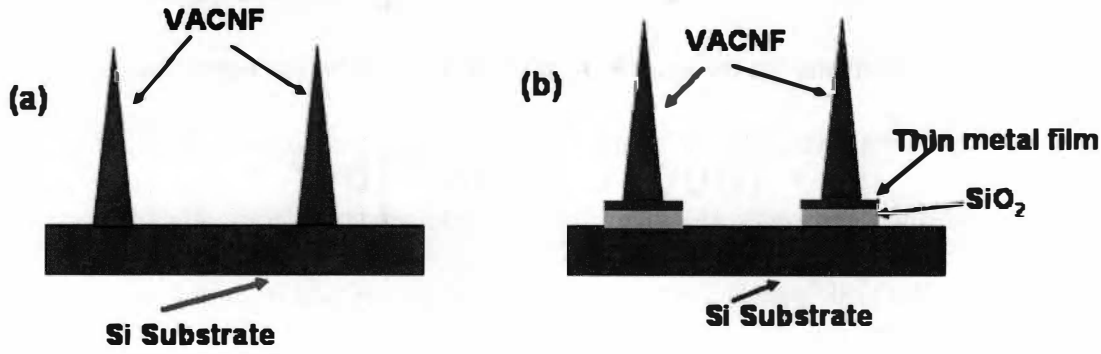

Figure 5-1. Achievement of individual cathode addressability. (a) VACNFs are grown on a conductive Si substrate and are all connected to each other; (b) VACNFs on a metal/SiO_2/Si substrate. The substrate has been patterned so VACNFs are isolated from each other.

After weighing all the options, the final idea is to deposit a conductive layer, presumably metal thin films, on the insulating substrate (SiO_2) before patterning the catalysts for VACNF growth. The substrate is now conductive, so plasma discharge can be maintained during the growth. However, the VACNFs are still electrically connected though. Through electrode patterning, the VACNFs can be isolated from one another (Figure 5-1).

5.3 Growth of VACNFs on a substrate other than silicon

Growth study of VACNFs on a silicon substrate has been discussed in Chapter 3. It was pointed out [17] that during the VACNF growth, a Si-N sheath is deposited on the sidewalls of the nanofibers. The Si comes from the sputtered substrate during growth. Cylindrical nanofibers that contain only carbon are discovered by removing the outer sheath using reactive ion etching (RIE). This outer sheath protects the VACNF during plasma etching, wet etching and other fabrication processes. In order to get similar chemistry in the carbon nanofibers, a thin layer of Si is added onto the top of the conductive metal layer.

Although the substrate is covered with a metal layer, it is still insulated from the heater cathode in the growth chamber by the SiO_2 layer. So during VACNF growth, the surface of the sample substrate is floating. Metal clips are thus used to ground the metal surface with the heater cathode. Still, it is not an easy task to develop a "recipe" to grow strong, sharp, aligned carbon nanofibers with the desired heights in this new configuration. In fact, a small change in the growth condition results in very different

growth results. One notable difference is that the supply rate of silicon to form the Si-N sheath from the substrate may be reduced; therefore the rate of the sheath deposition is reduced. To account for this reduction, C_2H_2 flow is accordingly reduced (from 57 sccm to 45 sccm). As a result, the growth time also needs to be adjusted; in this case, it is increased by 20-50%. The resultant carbon nanofibers are shown in Figure 5-2. Use of these bottom-addressed VACNFs in chemical probe applications has been investigated by Guillorn [88].

5.4 Individual cathode addressable device fabrication

The procedure to make field emission cathodes using these VACNFs is illustrated in Figure 5-3. A thin layer of oxide is deposited onto the Si substrate. This is followed by the deposition of 4 layers of metals: 10nm titantium/200nm tungsten/10nm titantium/10nm silicon (Figure 5-3 (b)). Ti is used here to improve the adhesion of the metals. Alignment marks are defined using photolithography and then etched using reactive ion etching (RIE) techniques. Electron beam lithography using a commercial system JEOL 6000 FS/E is performed to define the catalysts (Figure 5-3 (c)). Following catalyst deposition, the DC PECVD growth is carried out (Figure 5-3 (d)). The VACNFs are then patterned. In this process, photoresist is spun onto bare VACNFs at ~4000RPM. Following pattern definition, reactive ion etching is carried out for pattern transfer (Figure 5-3 (e)). After this process, the VACNFs are inspected under SEM and no damage is observed.

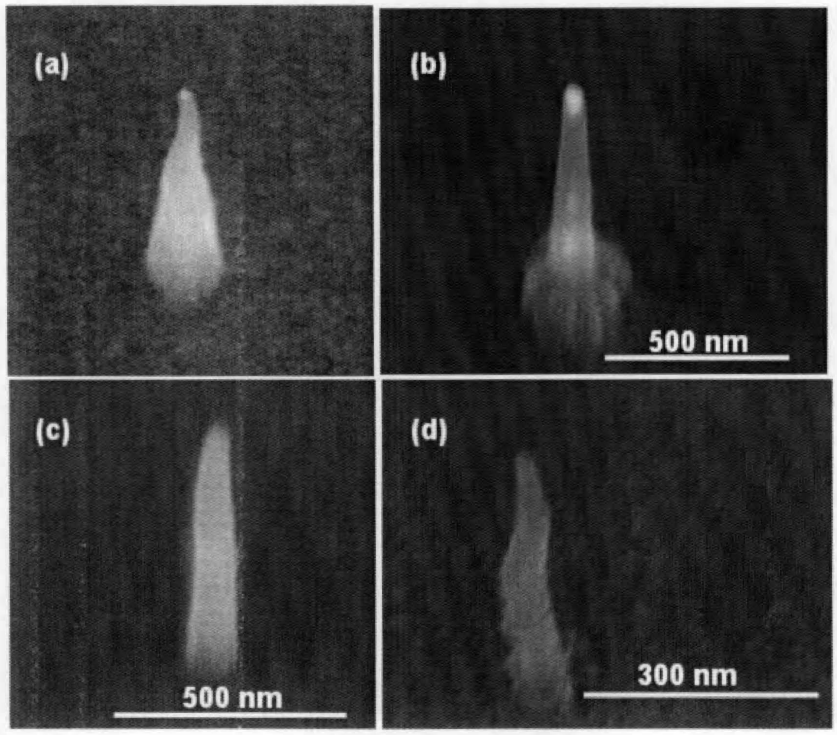

Figure 5-2. VACNFs of various qualities grown on a metal/SiO_2/Si substrate. (a) A sharp, vertical and strong VACNF; (b) a VACNF without the outer sheath; (c) a blunt VACNF; (d) a non-vertically-aligned, straight VACNF.

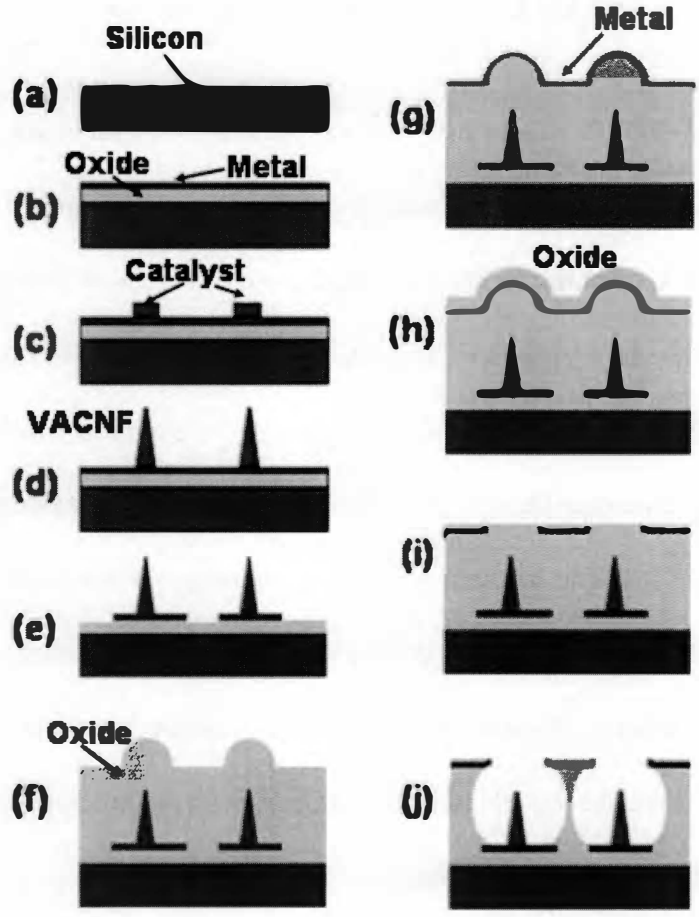

Figure 5-3. Schematics of the individual cathode-addressable device fabrication processes. (a) Start with a silicon substrate. (b) A 1μm oxide is deposited followed by 10nm Ti/200nm W/10nm Ti/10nm Si. (c) Alignment marks and catalysts are defined. (d) VACNFs growth. (e) The cathode electrode is patterned. (f) A 1μm layer of SiO_2 is deposited. (g) A thin metal layer is deposited as the gate electrode material. (h) Additional SiO_2 is deposited as a sacrificial layer during CMP. (i) CMP is performed and self-aligned apertures form. (j) Wet etching is performed to release SiO_2 inside the apertures.

Following growth of a 1 μm SiO_2 layer (Figure 5-3 (f)), the wafers go through another photolithography cycle for the gate electrode patterning along with the image reversal process (because of the bright field mask used). A layer of 150nm thick Cr is then deposited by e-beam evaporation, followed by liftoff (Figure 5-3 (g)). An additional layer of 500nm oxide is deposited as a sacrificial layer for chemical mechanical polishing (CMP). CMP is performed on these wafers to planarize the structures and form the apertures (Figure 5-3 (i)). The last step is wet etching using a buffered oxide etch (H_2O:HF=6:1) to release the oxide (Figure 5-3 (j)). Additional photolithography patterning is added here to protect areas other than around the apertures from exposure to wet etching. This is because the HF etch may attack the Cr electrodes due to the stresses present in the Cr film and surface roughness of the overall structure.

5.5 Characterization of the finished devices

Scanning electron microscope (SEM) images of a finished device is shown in Figure 5-4. The carbon nanofiber is very well aligned to the apertures and does not seem to degrade at all during the fabrication process. Also shown in Figure 5-4 is the alignment of the aperture for a tilted VACNF. It is observed that the apertures are aligned only according to the tip positions of the VACNF. This is easy to understand: the bump above VACNF forms right around the VACNF tips. Following CMP planarization, the bump is polished away, leaving apertures well aligned to the VACNF tips.

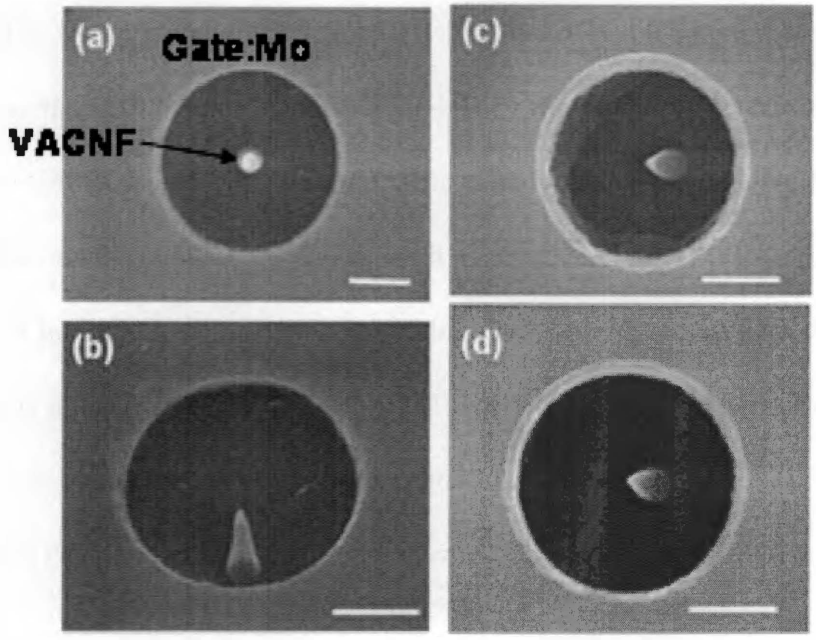

Figure 5-4. SEM images of the finished individual cathode-addressable devices. Picture (a) is at normal incidence angle of SEM and picture (b) is the SEM image at a 30° tilt angle. Pictures (c) and (d) show the self-alignment of apertures according to off-vertical VACNFs. The apertures are aligned to the tips of VACNFs.

The devices are then wire-bonded and transferred into a custom-made package. The field emission chamber used here has a feed-through for the electric connections. The chamber is pumped down to below 1×10^{-6} torr before the initiation of field emission. Keithley source measurement units (SMUs), models 237 and 2400, are used for this measurement. All cathodes and all gates are grounded together before testing. The anode is usually set at +1000V and the distance from the device to anode is around 6.7mm. The gate electrode is biased at ground potential during the test. For this initial FE testing, only one carbon nanofiber is tested each time. The cathode being tested is then biased negatively to drive electron emission. Typical field emission curves are shown in Figure 5-5. The behavior follows the Fowler-Nordheim equation with small fluctuations.

In summary, VACNFs-based field emission structures with individual cathode addressability are successfully designed and fabricated. Vacuum testing reveals a successful FE from the fabricated devices.

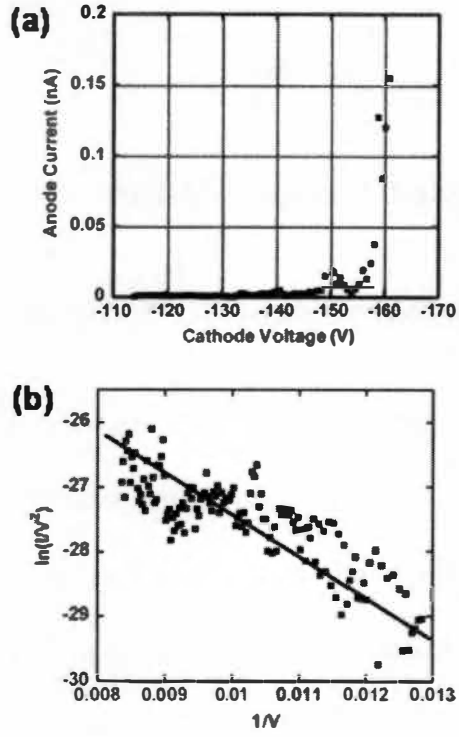

Figure 5-5. A current-voltage (I-V) curve obtained from the fabricated cathode-addressable device. (a) A typical I-V is obtained by sweeping the cathode biases negatively. (b) An I-V curve plotted in Fowler-Nordheim coordinates.

Chapter 6

Fully self-aligned dual-gate structures using VACNFs and investigation of nanoscale electron beam induced deposition techniques as a repair method

6.1 Design of fully self-aligned dual-gate devices

6.1.1Fine registry of VACNFs required for DEAL applications

As discussed in Chapter 1, in the application of massively parallel electron beam (EBL) lithography applications, millions of electron beams are operated in parallel for fine feature definition to achieve high throughput. For use as a next generation lithography tool, two things are essential: fine feature definition and pattern registry. An electron beam, if properly focused, can generally produce very small features due to its very short wavelength. To control the exact coordinates of lithography lines (pattern registry), first the origin of the electron beam needs to be calibrated. Since electrons usually originate from the very tip of the field emitters, i.e., the tips of VACNFs in this study, the origin of the electron beam can be controlled through the location of the field emitters.

However, there is usually an offset between the VACNF and the gate/focus electrodes in the fabrication processes employed by Guillorn *et al.* [23]. This is due to two factors: the resolution of the lithography tools and the migration of the VACNFs

during growth with respect to the predetermined locations. The effects of these offsets are investigated in detail in Chapter 2 using numerical simulation methods. The simulation results indicate that with moderate offsets, electron beam is deflected, but the beam shape is maintained at the anode. This is promising for lithography applications. Since the offsets in current devices [23] are higher than the amounts in simulation, methods to mitigate these offsets are desired.

As with any photolithography tool, there is usually limited pattern registry accuracy. The accuracy with Autostep 200, the tool employed in this thesis study, is claimed to be ~100nm, which is not accurate enough for EBL applications. The best way to produce highly aligned structures is to avoid photolithography tools for critical feature definition by utilizing a fully self-aligned process.

6.1.2 Literature review on design of fully self-aligned dual-gate structures

The single-gate structure is referred to as the cathode structure, and the dual-gate structure is also called the triode structure. In the triode structure, the bottom electrode is defined as the extraction electrode, or the gate electrode; the top electrode is called the focus electrode. The gate and focus electrode openings are referred to as apertures.

Chemical mechanical polishing (CMP) is used to design a fully self-aligned aperture formation process. Dvorson *et al.* [89] and Lee *et al.* [90] reported fully self-aligned silicon based dual-gate structures based on CMP self-aligning. The process [90] carried out two CMP steps to define each aperture (Figure 6-1). Based on the high CMP

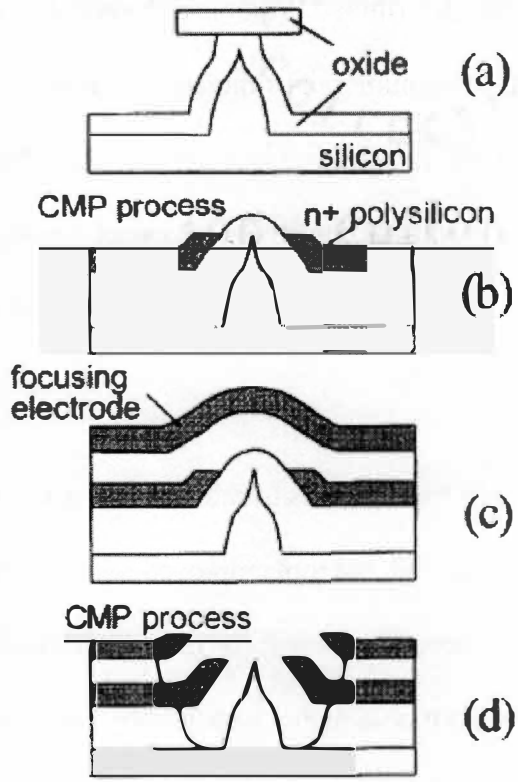

Figure 6-1. Self-aligned silicon-tips field emission devices based on CMP. (a) The silicon tip is etched and sharpened; (b) CMP is performed and the gate aperture is formed. Note the elevated height around the silicon tips. (c) Focus electrode is deposited and a bump is maintained around the tips. (d) Focus aperture is formed by another CMP process. [90]

selectivity of polysilicon with respect to oxide, the oxidized tips were exposed during CMP, leaving a localized bump formation around the tips (Figure 6-1 (b)). This height elevation was maintained after the focus electrode was defined (Figure 6-1 (c)). Thus additional CMP opened the focus apertures and thus leads to self-aligned apertures in both gate and focus (Figure 6-1 (d)). Dvorson *et al.* [89] elaborated upon this process and added several RIE steps for better control of the aperture formation. However, this process leads the formation of gate apertures that are too close to the emitter tips.

In this thesis study, the electrode is usually refractory metals deposited using e-beam evaporation techniques, so polysilicon CMP cannot be applied; neither can the CMP selectivity between the emitter material and oxide. Although these methods [89-90] cannot be applied directly to fabricate fully self-aligned VACNFs based field emission structures, methods modified from their research are investigated.

6.1.3 Design of fully self-aligned dual-gate (triode) structures using VACNFs

Since the first step in the device fabrication is oxide deposition, the morphology of the structure after oxide deposition is first characterized. Figure 6-2 shows both the AFM and SEM images of VACNFs after various amounts of oxide deposition. From Figure 6-2, we can see that oxide deposition is compatible with bare VACNFs and the height of the oxide bump over the VACNF is dependent on the amount of oxide deposited. This information is of great importance in the design of fully self-aligned triode structures as will be discussed later in this chapter. One possible fabrication

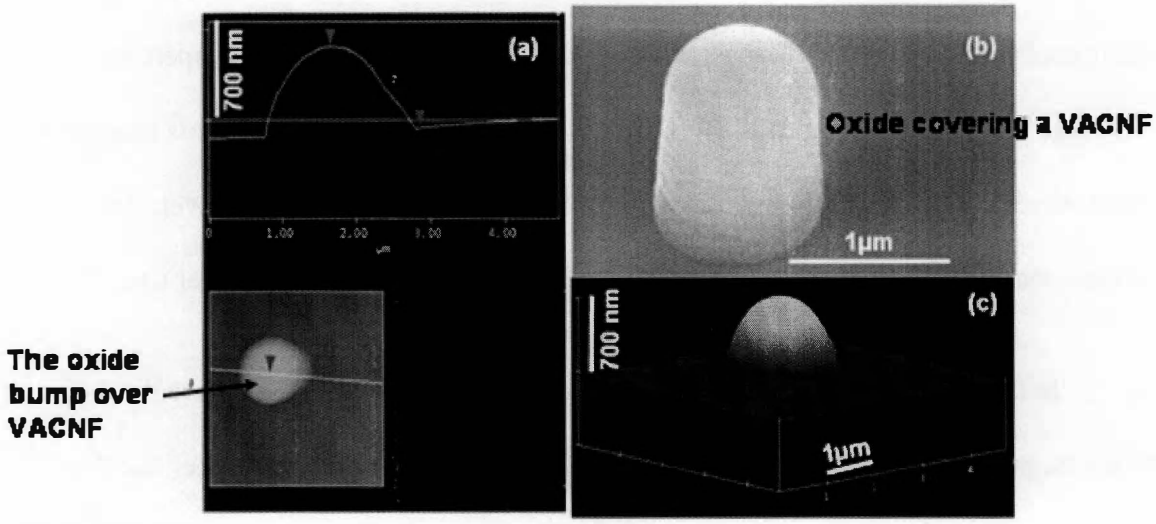

Figure 6-2. Pictures of the structures after oxide coating on 1μm-tall VACNFs. Picture (a) shows the step height of the bump over a VACNF tip in AFM (1.5μm thick oxide). Picture (b) shows a tilted image of an oxide-coated VACNF (700nm thick oxide). Picture (c) is the AFM image of an oxide-coated VACNF (1.5μm thick oxide).

scheme to realize fully self-aligned VACNF based triode structures is shown in Figure 6-3.

Four oxide/metal layers are first deposited, followed by a single CMP process. In this process, only one CMP is carried out and both apertures are formed simultaneously. Usually as a result, the gate aperture has a volcano-shape. Although the focus electrode is now partly shielded by the gate electrode, preliminary modeling results show that electron beam focusing can still be achieved by adjusting focus potentials. A device fabricated following this process is shown in Figure 6-3 (c). For this device, the height of the VACNF is ~1μm and the oxide thickness is ~700nm. Although both apertures are successfully defined and very well aligned, as can be seen in the image (Figure 6-3 (c)), the gate electrode opening is too small for practical use of this device. However, the focus aperture has the desired size of ~2μm. So it is unlikely to produce appropriate sized apertures on both the gate and focus electrode level by adjustment of device design parameters, such as oxide thickness; therefore, other paths to achieve self-alignment must be considered.

Another way to achieve fully self-aligned triode structures is based on Figure 6-1. The key design of the process as shown in Figure 6-1 is that the bump was not completely planarized in Figure 6-1 (b). Continuation of oxide/metal deposition leads to the extension of the bump that is still well registered to the emitter. Based on Figure 6-1, a similar process is designed to fabricate fully self-aligned VACNFs-based triode structures, shown in Figure 6-4. The first few steps as shown in Figure 6-4 (a-e) is the same as the process employed by Guillorn *et al.* [23]. Then as shown in Figure 6-4 (f),

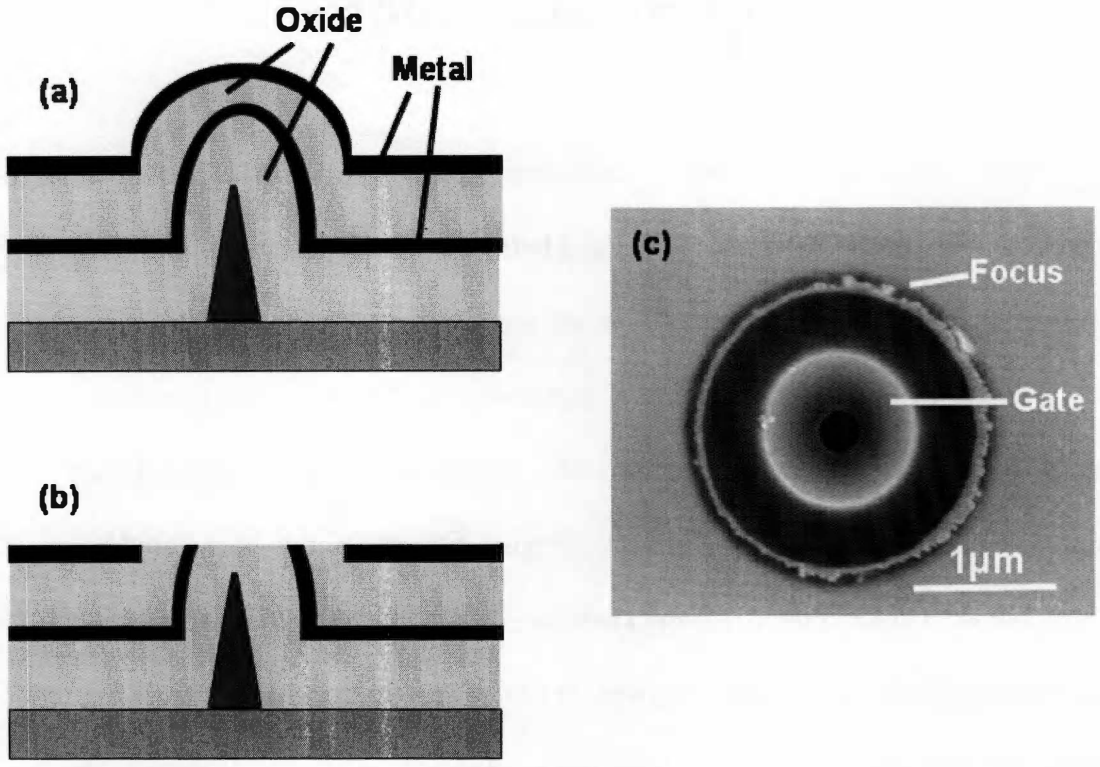

Figure 6-3. One proposed fully self-aligning fabrication process based on a single CMP process. (a) Deposition of all the oxide/metal. (b) CMP is performed and both gate and focus apertures are defined. (c) A normal incidence SEM picture showing a typical device fabricated by this process. The VACNF can not be seen because of the small aperture opening.

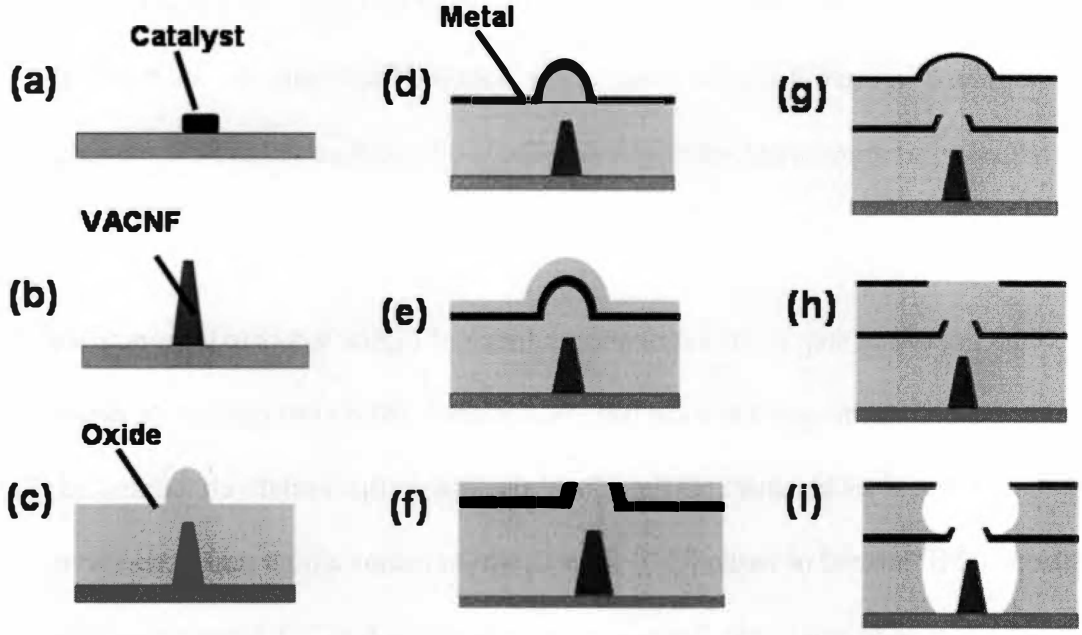

Figure 6-4. A design scheme to realize fully self-aligning based on two CMP steps for aperture definition. (a) The catalyst is defined using electron beam lithography (EBL) and deposited. (b) A VACNF is grown by DC-PECVD. (c) An oxide deposition is carried out, (d) followed by gate electrode definition. (e) A sacrificial layer of oxide is deposited before CMP. In step (f), CMP polishing is terminated before completely removing the bump. (g) More oxide/metal is deposited and the bump remains. (h) Focus apertures can be formed by employing CMP once more. (i) Wet etch is used to release oxide in the apertures.

CMP polishing is designed to terminate before completely removing the bump. In this way, a partial bump is maintained (Figure 6-4 (g)). The focus apertures can be formed by employing CMP once more (Figure 6-4 (h)). Lastly, wet etching is used to release oxide in the apertures (Figure 6-4 (i)). In this process, both the focus and gate aperture sizes can be adjusted, so appropriate-sized gate and focus openings can both be achieved by this process.

One important step in the fabrication scheme of Figure 6-4 is to terminate the CMP process before the structures are fully planarized. This is not difficult to achieve on silicon based processes because: (1) the size of the silicon tip is relatively large, and (2) polysilicon CMP instead of oxide CMP is used, which means a high polish selectivity between the electrode and oxide. In the process to develop VACNF based fully-self aligning processes, the VACNF tips are on the nanometer scale and the polysilicon electrode by low pressure chemical vapor deposition (LPCVD) is not yet possible, so oxide CMP is the only choice.

The possibility of partially planarizing at step (f) in Figure 6-4 is investigated: devices after various amounts of CMP polish are characterized (Figure 6-5). CMP is known to be effective in device planarization and the bump over VACNFs is ripped off immediately during CMP (the bump is dislocated from the circular gate opening in Figure 6-5 (a)). This bump may affect subsequent device processing and needs to be removed. It is determined that the dislocated bump can be easily eliminated by either wet etching or dry etching. The device structure after bump removal in shown in Figure 6-5 (b).

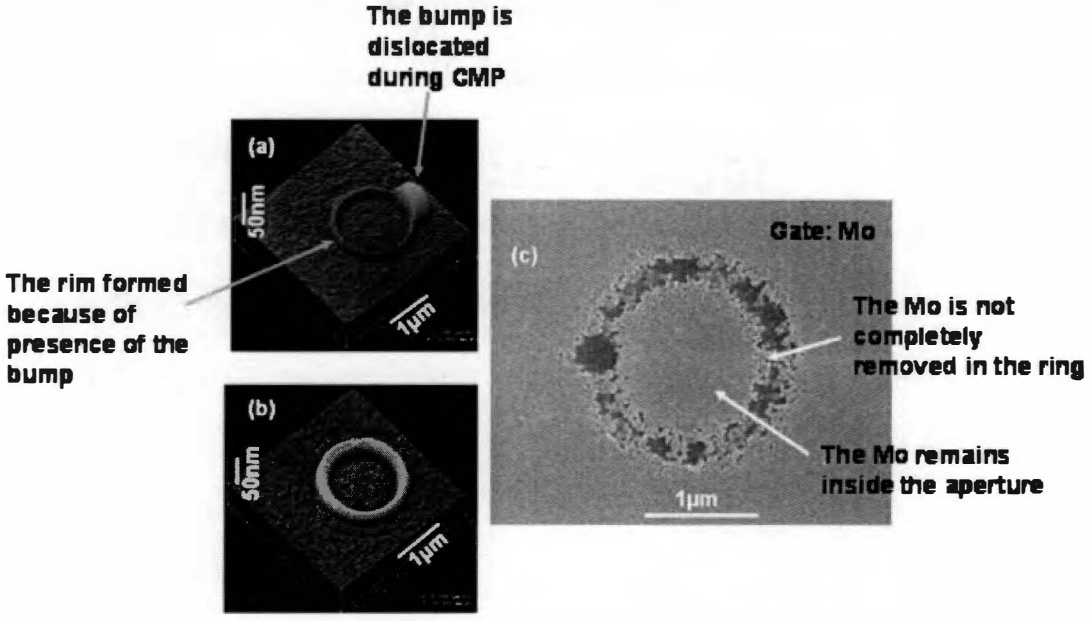

Figure 6-5. AFM and SEM images of the device at various stages of the fabrication scheme in Figure 6-4. (a) An AFM image of the device immediately after the first CMP (Figure 6-4 (f)). The bump is dislocated from the center of the gate aperture. (b) The AFM image of the device after cleaning of the polished bump. (c) An SEM image of the device after the focus aperture definition. The aperture definition is not successful and metal remains inside the aperture.

The subsequent fabrication can thus be carried out. However, a big problem still exists: there is not much of a bump left after CMP. The only thing left is a rimmed gate opening and the inside of the aperture is at the same height level as the structure outside of the aperture. Moreover, the gate rim is measured to be less than 30nm. Since the focus electrode is at least 100nm thick, the bump in Figure 6-4 (g) needs to be higher than 100nm, which cannot be achieved based on the gate rim of less than 30nm. The focus aperture definition is not successful, as shown in the SEM image of Figure 6-5 (c), after step (h) in Figure 6-4.

Now the realization of the fabrication scheme of Figure 6-4 lies in the adjustment of the CMP polish recipe to reduce the CMP planarization effectivity and maintain a higher partial bump after the step in Figure 6-4 (f). Past research shows that by increasing the back pressure (the pressure applied to the wafer during CMP), and reducing down pressure, the ratio of post- to pre-polish step height increases [91-92]. So CMP polish process with back pressure from 1.5psi to 7psi and wafer chuck rotation from 9RPM to 26RPM is performed in this study. At the very extreme (very high back pressure and low rotation), the polish rate drops dramatically. At this stage, wafers are likely to be broken during to the high friction and low retention force. A suitable recipe for controlled VACNF-related bump removal has not been found in this study.

Based on the investigation of fabrication schemes of Figure 6-3 and Figure 6-4, other methods other than CMP alone must be considered to realize fully self-aligned structures. One such idea is shown in Figure 6-6. VACNFs are grown on the substrate (Figure 6-6 (a)). Oxide is deposited over VACNFs (Figure 6-6 (b)) and the gate electrode

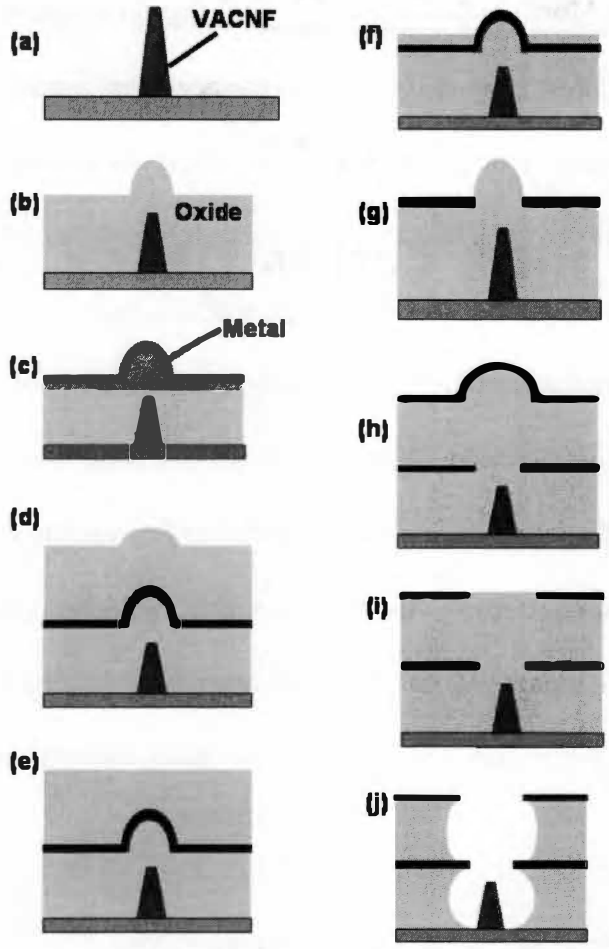

Figure 6-6. A fully self-aligning process based on both CMP and etch selectivity of RIE. (a) VACNFs are grown on the substrate; (b) oxide is deposited over VACNFs; (c) metal film is patterned; (d) more oxide is deposited; (e) CMP is carried out for structure planarization; (f) an oxide RIE process is carried out to remove most of the oxide on top of the electrode; (g) a metal RIE process is carried out to remove the metal over the bump: In this process, a remaining thin layer of oxide is used to protect the metal electrodes from being etched; (h) another layer of oxide/metal is deposited; (i) CMP once more leads to the formation of the focus electrode aperture; (j) wet etching is performed to release oxide inside the apertures.

is patterned (Figure 6-6 (c)). More oxide is deposited (Figure 6-6 (d)) and CMP is carried out for full structure planarization (Figure 6-6 (e)). In the next step, a reactive ion etch (RIE) designed for oxide is carried out to remove most of the oxide on top of the electrode (Figure 6-6 (f)). This oxide RIE recipe has a very low etch rate on the metal (molybdenum (Mo), in this study), so the bump is exposed. Following this, a RIE process designed for metal etch is carried out to remove the thin layer of metal over the bump (Figure 6-6 (g)). In this process, a remaining thin layer of oxide is used to protect the metal electrodes other than the bump from being etched. The gate aperture is now opened and more importantly, the bump remains. Another layer of oxide/metal is then deposited and by employing CMP once more the focus electrode aperture is defined (Figure 6-6 (h) and (i)). Lastly, wet etching is performed to release oxide inside the apertures (Figure 6-6 (j)).

In this process, the electrode material is molybdenum (Mo). The Mo etch recipe has an etch rate of >80nm/minute on Mo, and ~50nm/minute on oxide. The oxide etch recipe has an etch rate of ~60nm/minute on oxide, but only ~5nm/minute on Mo (selectivity of >10:1). Although two steps of CMP are used in this process, the first CMP step for a simple planarization purpose doesn't need stringent control. The surface is completely planarized and is pure oxide after the first CMP process. Full planarization insures device continuation in further device integration. The opening of the gate aperture is done by RIE and this process can be easily controlled through the etch time.

The devices are imaged during and after the fabrication process (Figure 6-7). Figure 6-7 (a) shows a tilt-angle SEM image of the device at step (g) in Figure 6-6. The metal is completely removed from the bump, as confirmed by X-ray energy dispersive analysis (EDS). The bright dot in Figure 6-7 (a) is actually above the rest of the structure and the AFM image in Figure 6-7 (b) confirms this. The bump height is now ~400nm, and this height is adequate for the further definition of focus apertures (the focus electrode is ~150nm thick). Final device images are shown in Figure 6-7 (c) and (d). A VACNF can be seen at the bottom of the device.

In summary, several fabrication schemes towards the realization of fully self-aligning are discussed. Because of the nature of the nanoscale tips involved, and the employment of oxide CMP process, most of the fabrication schemes do not produce well-defined, reproducible devices. The fabrication process described in Figure 6-6 is the best method; devices are successfully fabricated by this process.

6.2 Design of Field emission devices using W nanofibers selectively grown by nanoscale EBID

6.2.1 The need to repair VACNF in dual-gate field emission structures

VACNFs are used as the field emission elements in DEAL applications [12] mainly because of the massive production capability in a vertically aligned fashion. In DEAL concept, Baylor *et al.* suggested a density of emitter cathodes of $\sim 3\times10^6/cm^2$ for a minimum throughput of 60 wafers per hour. Redundancy is achieved by slight rotation

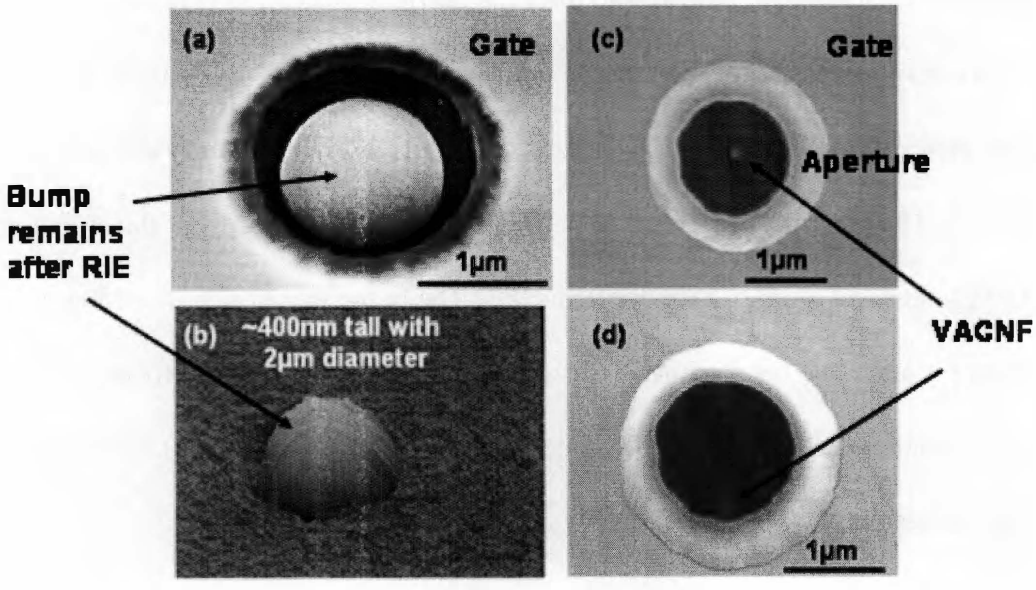

Figure 6-7. AFM and SEM images of devices following the fabrication scheme in Figure 6-6. (a) A tilted-angle image of the device at step (g) in Figure 6-6 after the removal of metal over bump. (b) The AFM image of the device at step (g) in Figure 6-6. (c) A normal incidence angle SEM image of the finished device. (d) A tilted SEM image of the finished device.

(~0.4°) of the emitter plane with respect to the wafer motion (Figure 6-8). However, this redundancy can only compensate for ~1% of bad emitters (missing or defective). Since the percentage of defective VACNFs in the finished devices is much higher than 1%, methods to repair or replace these emitters are essential.

6.2.2 Single-gate field emission devices using W nanofibers selectively grown by nanoscale EBID

Single-gate field emission cathodes using W nanofibers selectively grown by nanoscale EBID are investigated. Device fabrication was performed on 100mm diameter, device quality, low resistivity, n-type silicon wafers [Figure 6-9 (a)]. A 1μm SiO_2 film was deposited onto the silicon substrate using a silane-based RF PECVD process. The wafer was then metallized with 150nm of molybdenum (Mo) deposited by electron beam evaporation [Figure 6-9 (b)]. The gate apertures were then defined using photolithography [Figure 6-9 (c)] and a reactive ion etch (RIE) process was performed to etch the aperture pattern through the Mo film back to the oxide layer [Figure 6-9 (d)]. The structures were then immersed in a dilute solution of hydrofluoric acid (Buffered Oxide Etch, water: HF=6:1) to remove the oxide inside the apertures. The resist was then stripped using NMP 1165 resist stripper and the structures were thoroughly rinsed in de-ionized water and dried with N_2 [Figure 6-9 (e)]. The resultant structure had a 2.5μm diameter aperture opening and was ~1μm deep.

Tungsten nanofibers were then deposited by EBID at the center of each aperture [Figure 6-9 (f)]. The deposition process has been included in Chapter 3. The resultant W

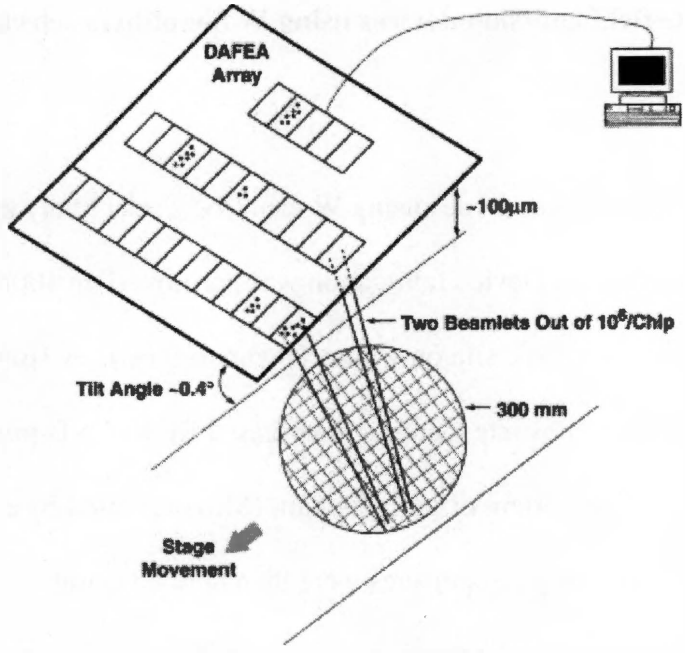

Figure 6-8. Diagram of the DEAL lithography redundancy design. Redundancy is achieved by slight rotation of the DAFEA arrays with respect to the wafer movement: each wafer pixel is illuminated by multiple writing beams [12].

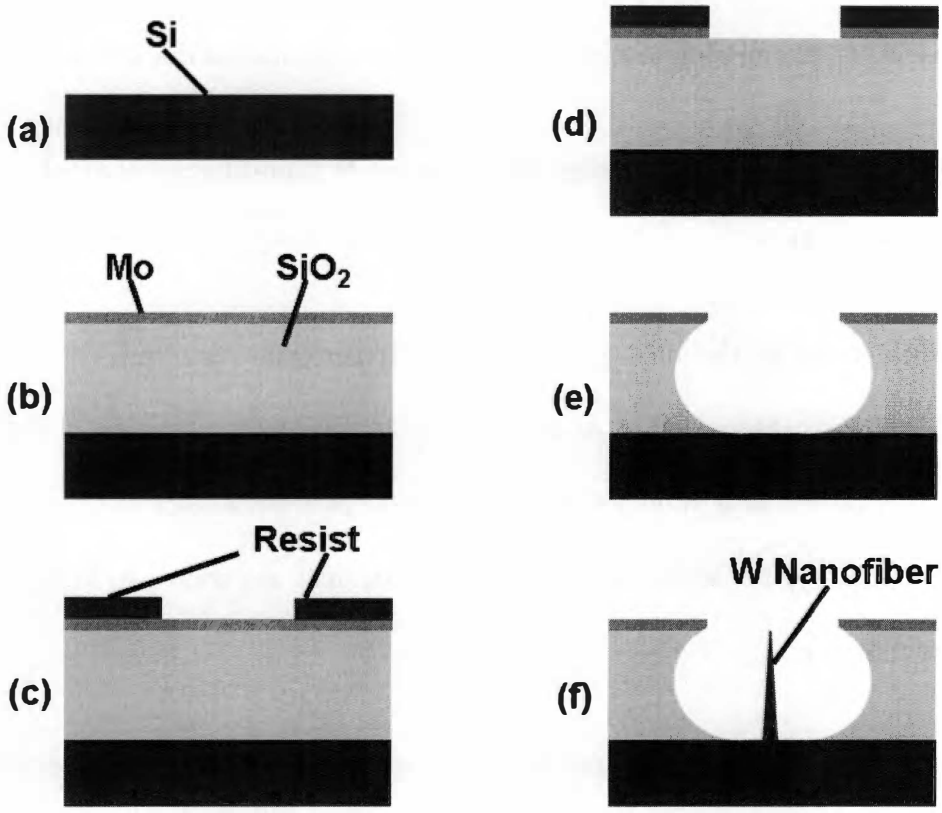

Figure 6-9. Summary of the W nanofiber cathode device fabrication process. (a) Start with a low-resistivity Si wafer; (b) 1μm SiO_2 is deposited followed by 150nm Mo; (c) apertures are patterned and developed; (d) Mo is etched by RIE; (e) SiO_2 is cleared by HF; (f) W nanofibers are deposited by EBID.

nanofiber was ~1μm tall and 40nm wide with tip diameters of less than 15nm. The quality of this process is high—it was deterministic and there were no observable defects in the devices. Field emission test is successful in these devices as discussed in Chapter 4.

6.2.3 Dual-gate field emission devices using W nanofibers selectively grown by nanoscale EBID

While most of the dual-gate devices [23] perform very well, occasionally a missing VACNF is discovered in an otherwise good structure, as shown in Figure 6-10 (a). EBID deposition of a W nanofiber was carried out at the center of the apertures on these structures. Typical SEM images of finished devices are shown in Figure 6-10 (b) and Figure 6-10 (c).

Initial FE test is carried out and similar emission behaviors as discussed in Chapter 3 are discovered. Following initial FE testing, the devices were then loaded into another chamber specifically built for DEAL lithography testing on PMMA coated samples. The lithography testbed has been described in an earlier publication [85]. In brief, a JEOL 5D-II is modified by removing the original electron column and replacing it with a spool piece with a leveling ring and a bracket. This bracket is attached to a motorized stage. Fiber-optic displacement sensors are built into the system for position measurements. Four Keithley 237 SMUs are also employed to monitor and control the devices.

For the lithography test, PMMA coated glass substrates were loaded onto the JEOL 5D-II cassettes. A W nanofiber device chip was then loaded on top of the PMMA

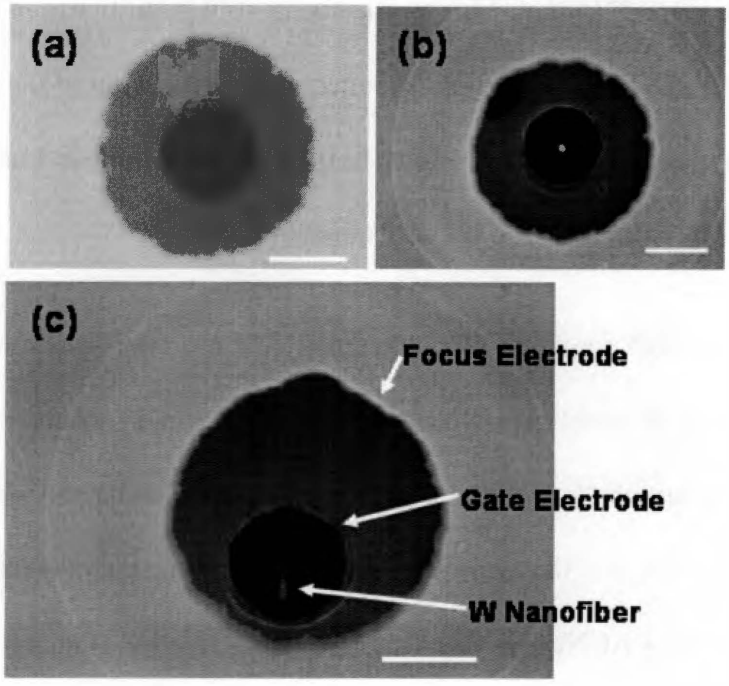

Figure 6-10. The SEM images of dual-gate devices prior to and after W nanofiber deposition. (a) The finished DEAL structure with a missing nanofiber; (b) normal view of the device structure after a W nanofiber was electron beam deposited at the center of the apertures; (c) 20° tilted view of a W nanofiber inside the aperture. The scale bar is $1\mu m$.

coated glass substrates. The nanofiber chip was lowered to ~500μm above the substrate during the writing. The cathode was operated at -500V with respect to the glass substrate. Typical lithography lines are shown in Figure 6-11. The lines were bright with relatively sharp edges. There were 5V increments in the focus voltage in between each line. The decrease in the linewidth from top to bottom reflects better focusing of the electron beam, consistent with numerical simulation results [23]. The W nanofiber longevity was not comprised even in close proximity to the resist-coated substrates.

In conclusion, both single- and double-gated field emission structures have been fabricated using EBID W nanofibers. Successful field emission is observed for both structures. Initial lithography is successful and the electron beam can also be focused by applying focus potentials. It is thus very promising to use EBID techniques to repair/replace defective VACNFs.

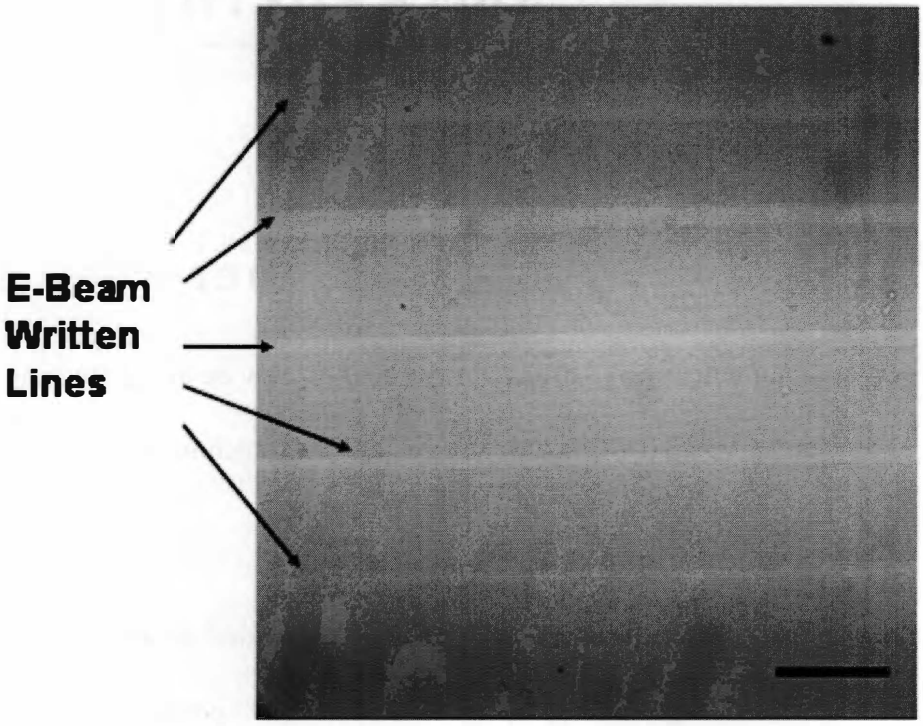

Figure 6-11. Optical images of the initial lithography lines obtained using these W nanofiber triode structures. The scale bar is ~100μm.

Chapter 7

Conclusion

7.1 Conclusion

In this thesis, numerical simulations of ray tracking, new device design and fabrication, and repair of VACNFs-based devices using EBID techniques are accomplished.

Numerical simulation of the triode performance is included in this thesis. Lorentz 2D and 3D software from Integrated Engineering Software (IES) company is used for this purpose. A two-dimensional rotational-symmetric model is first created. Depth of field (DOF) on the current devices is investigated by adjusting the working distances. The DOF of these triode structures is calculated by simulation to be ~5μm for the current triode structures. Electrode thickness effects on the device behavior is investigated by adjusting the thickness of both the gate and focus electrodes from 100nm to 500nm. The simulation results indicate that the DOF can be improved by employing thicker electrodes since the slope of beam radius change per applied focus voltage is decreased for thick electrodes. The optimum beam radius is also reduced for thick electrodes. Simulation results also indicate that less focus voltage is needed for thicker electrodes. Three-dimensional (3D) simulation is also carried out to study misaligned devices in which rotational symmetry can no longer be assumed. 3D modeling results for three different cases are studied and compared: no misalignment case, focus-electrode misaligned case

and carbon-nanofiber misaligned case. 3D modeling of the structure misalignment shows that a very small and well-converged beam is observed for the maximum shifts studied: 100nm focus electrode shift or 50nm VACNF shift, although astigmatism and coma-type aberrations will increase somewhat from these misalignments. The beam is deflected as a result of the device offsets. The beam deflection to focus-electrode offset ratio is ~15:1, while the beam deflection to carbon-nanofiber offset ratio is ~10:1.

Single-gate individual cathode-addressable devices are successfully designed. In this thesis study, since DC-PECVD is the main growth method, the devices are fabricated through the growth of VACNFs on a sandwich-like substrate: metal/oxide/silicon. The growth of VACNFs is different from that on a bulk silicon substrate. Less C_2H_2 flow is needed and the growth time also needs to be adjusted. The substrate with VACNFs is then patterned and as a result, each VACNF is isolated from the others. Microfabrication is carried out and CMP self-aligned apertures are attained. Scanning electron microscope images show a high quality device fabricated in this way. Further electrical FE testing reveals that the devices function very well as individual FE sources.

Several possible fabrication schemes to achieve fully self-aligning aperture formation in triode fabrication are also designed and discussed in this thesis. The conventional silicon fabrication process is not suitable and CMP alone is not enough for the definition of both gate and focus apertures in a self-aligning fashion due to two reasons: (1) the nanoscale size of the field emitter, (2) refractory metals instead of polysilicon electrodes are used, so the selectivity of polysilicon CMP on oxide can't be applied. A fabrication method is developed that combines both chemical mechanical

polishing (CMP) and reactive ion etching (RIE) selectivity to achieve fully self-aligned apertures. The devices are characterized during and after the fabrication. Both SEM and AFM images are obtained and indicate that fully self-aligned devices can be successfully fabricated by this method.

Repair on a missing/defective VACNF in triodes is demonstrated using EBID techniques. EBID techniques are the best choice for VACNF field emission device repair since it is a direct-write technique and requires no mask, no resist and no post-processing. Devices are produced by fabricating the device first without a VACNF followed by the deposition of EBID nanoemitters. Both single and dual-gate devices with an EBID deposited W nanofibers are produced. Field emission test is carried out on these devices and electrons are successfully extracted from the nanofiber tip and collected by the phosphor anode. Longevity of the devices are characterized and the devices have a long lifetime similar to carbon nanofiber devices. Initial lithography test using the fabricated W triode device is carried out in a modified JEOL 5D-II system. Lithography lines are also successfully written and the linewidth varies with the focus voltage, proof of beam focus. The lifetime of the W devices is not compromised even in close proximity to the resist environment.

In addition for the application of massively parallel electron beam lithography, these field emission devices can also be used in any application that requires an electron source, such as field emission display and electron microscopy applications.

7.2 Future work

Future work can be carried out in several areas, including optimization of the VACNF growth, device fabrication and testing, and numerical simulation.

In this thesis work, a fully self-aligning process is designed to compensate for device misalignments from both the limited accuracy of the lithography tool and the VACNF migration during growth. In these fully self-aligned devices, the apertures and VACNFs are well registered to each other. However, if the VACNF drifts from its predetermined location, the device is shifted accordingly. Although this may not pose a problem in a single-beam lithography system, for massively parallel EBL applications, this means that the locations of millions of electron beams are all needed to be calibrated individually. Therefore ways to mitigate VACNF migration during growth are of great importance. The VACNF migration occurs during the initial growth when catalyst nanoparticles first ball up. The amount of VACNF migration usually depends on the buffer layer material (native silicon in this thesis, Ti, TiN, etc.), the catalyst characteristics (the particle size, the stress, etc.) and the growth temperature (at lower temperature, there should be less mobility of the catalyst nanoparticle, thus leading to less migration).

Lithography testing using these fully self-aligned triode structures needs to be conducted. One of the most important factors characterizing an EBL system is the smallest achievable feature size. Larry *et al.* [64] reported ~300nm linewidth in this initial lithography effort. The 300nm linewidth is mainly limited by the misalignment of

the triode structures [23], so narrower lines are possible with these fully self-aligned triodes. Also in this thesis, both fully self-aligned and individual cathode-addressable devices are designed and fabricated. Further realization of individual cathode-addressable triode structures with fully self-aligned apertures can also be explored.

In field emission testing, one area of future work is the investigation of the focus voltage effects on the local electrical field at the emitter tip, or on the emission current. The voltage on the focus electrode counteracts the field enhancement, but quantitative effect depends on the device design and can be overwhelming or just ignored, to the extremes. Both experiments and simulation can be performed to investigate this effect.

Experimental focus data can be applied to direct the choice of parameters used in numerical simulation. For example, the emission half angle in the simulation is assumed to be 9°, and under a certain focus voltage, the simulation results give an electron beam size of 50nm. Experimentally, under the same operating conditions, a linewidth of 90nm is obtained. We know then the emission half angle may be under-estimated and needs to be adjusted. However, caution should be exerted here that the experimental linewidth is a combination of actual electron beam size, aberration, stigma, and proximity effects. Corrections are needed before comparison with the simulation results.

LIST OF REFERENCES

LIST OF REFERENCES

[1] L. Hoddeson, V. Daitch, *True Genius: The Life and Science of John Bardeen.* (Joseph Henry Press, 2002).

[2] L. F. Thompson, *Introduction to Microlithography*, Second Edition. Edited by L. F. Thompson, C. G. Willson, and M. J. Bowden. (Washington. DC: American Chemical Society, 1994), p.1.

[3] C. G. Willson, *Introduction to Microlithography*, Second Edition, Ed. L. F. Thompson, C. G. Willson, and M. J. Bowden, (Washington. DC: American Chemical Society, 1994), p.139.

[4] S. M. Sze, *VLSI Technology*, Second Edition. (New York: McGraw-Hill Book Company, 1998).

[5] dot.che.gatech.edu/henderson/.

[6] G. E. Moore, Electronics, **38**, 114 (1965).

[7] www.howstuffworks.com.

[8] J. E. Bjorkholm, Intel Technology Journal, **Quarter 3** (1998).

[9] R. S. Dhaliwal, W. A. Enichen, S. D. Golladay, M. S. Gordon, R. A. Kendall, J. E. Lieberman, H. C. Pfeiffer, D. J. Pinckney, C. F. Robinson, J. D. Rockrohr, W. Stickel,

and E. V. Tressler, IBM Journal of Research and Development-Advanced Semiconductor Lithography, **45** , 615, (2001).

[10] J. E. Schneider, P. Sen, D. S. Pickard, G. I. Winograd, M. A. McCord, R. F. W. Pease, W. E. Spicer, A. W. Baum, K. A. Costello, and G. A. Davis, J. Vac. Sci. Technol. B, **16**, 3192 (1998).

[11] T. H. P. Chang, M. G. R. Thomson, E. Kratschmer, H. S. Kim, M. L. Yu, K. Y. Lee, S. A. Rishton, B. W. Hussey, and S. Zolgharnain, J. Vac. Sci. Technol. B, **14**, 3774 (1996).

[12] L. R. Baylor, D. H. Lowndes, M. L. Simpson, C. E. Thomas, M. A. Guillorn, V. I. Merkulov, J. H. Whealton, E. D. Ellis, D. K. Hensley, and A. V. Melechko, J. Vac. Sci. Technol. B, **20**, 2646 (2002).

[13] T. H. P. Chang, J. Vac. Sci. Technol., **12**, 1271 (1975).

[14] C. A. Spindt, I. Brodie, L. Humphrey, and E. R. Westerberg, J. of Applied Physics, **47**, 5248 (1976).

[15] V. I. Merkulov, D. H. Lowndes, L. R. Baylor, J. Appl. Phys, **89,** 1933 (2001).

[16] V. I. Merkulov, M. A. Guillorn, D. H. Lowndes, M. L. Simpson and E. Voelkl, Appl. Phys. Lett., **79**, 1178 (2001).

[17] A. V. Melechko. T. E. McKnight, D. K. Hensley, M. A. Guillorn, A. Y. Borisevich, V. I. Merkulov, D. H. Lowndes, M. L. Simpson, Nanotechnology, **14**, 1029 (2003).

[18] L. R. Baylor, V. I. Merkulov, E. D. Ellis, M. A. Guillorn, D. H. Lowndes, A. V. Melechko, M. L. Simpson, and J. H. Whealton , J. Appl. Phys., **91**, 4602 (2002).

[19] K. B. K. Teo, M. Chhowalla, G. A. J. Amaratunga, W. I. Milne, G. Pirio, P. Legagneux, F. Wyczisk, D. Pribat, D. G. Hasko, Appl. Phys. Lett., **80**, 2011 (2002).

[20] M. A. Guillorn, M. L. Simpson, G. J. Bordonaro, V. I. Merkulov, L. R. Baylor, and D. H. Lowndes, J. Vac. Sci. Technol. B, **19**, 573 (2001).

[21] M. A. Guillorn, A. V. Melechko, V. I. Merkulov, E. D. Ellis, M. L. Simpson, D. H. Lowndes, L. R. Baylor, and G. J. Bordonaro, J. Vac. Sci. Technol. B, **19**, 2598 (2001).

[22] M. A. Guillorn, A. V. Melechko, V. I. Merkulov, D. K. Hensley, M. L. Simpson, and D. H. Lowndes, Appl. Phys. Lett., **81**, 3660 (2002).

[23] M. A. Guillorn, X. Yang, A. V. Melechko, D. K. Hensley, M. D. Hale, V. I. Merkulov, M. L. Simpson, L. R. Baylor, W. L. Gardner, and D. H. Lowndes, J. Vac. Sci. Technol. B, **22**, 35 (2004).

[24] P. M. Ajayan, Chem. Rev., **99**, 1787 (1999).

[25] R. Saito, M. Fujita, G. Dresselhaus, and M. S. Dresselhaus, Applied Physics Letters, **60**, 2204 (1992).

[26] H. Cui, X. Yang, M. L. Simpson, D. H. Lowndes, and M. Varela, Applied Physics Letters, **84**, 4077 (2004).

[27] V. I. Merkulov, D. K. Hensley, A. V. Melechko, M. A. Guillorn, D. H. Lowndes, M. L. Simpson, J. Phys. Chem. B, **106**, 10570 (2002).

[28] R. T. K. Baker, Carbon, **27,** 315 (1989).

[29] Z. F. Ren, Z. P. Huang, J. W. Xu, J. H. Wang, P. Bush, M. P. Siegal and P. N. Provencio, Science, **282,** 1105 (1998).

[30] M. Ohring, *Materials Science of Thin Films* (Academic Press, San Diego, 2002).

[31] K. B. K. Teo, S. -B. Lee, M. Chhowalla, V. Semet, V. T. Binh, O. Groening, M. Castignolles, A. Loiseau, G. Pirio, P. Legagneux, D. Pribat, D. G. Hasko, H. Ahmed, G. A. J. Amaratunga and W. I. Milne, Nanotechnology, **14**, 204 (2003).

[32] V. I. Merkulov, D. H. Lowndes, Y. Y. Wei, G. Eres, E. Voelkl. Applied Physics Letter, **76**, 3555 (2000).

[33] A. V. Melechko, V. I. Merkulov, D. H. Lowndes, M. A. Guillorn and M. L. Simpson, Chemical Physics Letters, **356**, 527 (2002).

[34] V. I. Merkulov, A. V. Melechko, M. A. Guillorn, M. L. Simpson, D. H. Lowndes, J. H. Whealton, and R. J. Raridon, Applied Physics Letters, **80**, 4816 (2002).

[35] V. I. Merkulov, A.V. Melechko, M. A. Guillorn, D. H. Lowndes, and M. L. Simpson, Applied Physics Letters, **79**, 2970 (2001).

[36] K. B. K. Teo, M. Chhowalla, G. A. J. Amaratunga, W. I. Milne, G. Pirio, P. Legagneux, F. Wyczisk, J. Olivier, and D. Pribat, J. Vac. Sci. Technol. B, **20**, 116 (2002).

[37] V. I. Merkulov, A. V. Melechko, M. A. Guillorn, D. H. Lowndes and M. L. Simpson, Chemical Physics Letters, **350**, 381 (2001).

[38] L. Zhang, D. Austin, V. I. Merkulov, A. V. Meleshko, K. L. Klein, M. A. Guillorn, D. H. Lowndes, and M. L. Simpson, Applied Physics Letters, **84**, 3972 (2004).

[39] A. Bachtold, M. S. Fuhrer, S. Plyasunov, M. Forero, E. H. Anderson, A. Zettl, and P. L. McEuen, Physical Review Letters, **84**, 6082 (2000).

[40] B. Wei, R. Spolenak, P. K.-Redlich, M. Rühle, and E. Arzt. Applied Physics Letters, **74**, 3149 (1999).

[41] X. Yang, M. A. Guillorn, D. Austin, A. V. Melechko, H. Cui, H. M. Meyer III, V. I. Merkulov, J. B. O. Caughman, D. H. Lowndes, and M. L. Simpson, Nano Letters, **3**, 1751 (2003).

[42] P. D. Rack, S. Randolph, Y. Deng, J. Fowlkes, Y. Choi, and D. C. Joy, Appl. Phys. Lett., 82, 2326 (2003).

[43] M. -Y. Yen, C. -W. Chiu, F. -R. Chen, J. -J. Kai, C. -Y. Lee, and H. -T. Chiu, Langmuir, 20, 279 (2004).

[44] I. Utke, B. Dwir, K. Leifer, F. Cicoira, P. Doppelt, P. Hoffmann, E. Kapon, Microelectronic Engineering, 53, 261 (2000).

[45] M. Takai, T. Kishimoto, H. Morimoto, Y. K. Park, S. Lipp, C. Lehrer, L. Frey, H. Ryssel, A. Hosono, and S. Kawabuchi, Microelectronic Engineering, **41/42,** 453 (1998).

[46] O. Yavas, C. Ochiai, M. Takai, A. Hosono, and S. Okuda, Applied Physics Letters, **76**, 3319 (2000).

[47] P. C. Hoyle, J. R. A. Cleaver, and H. Ahmed, J. Vac. Sci, Technol. B, **14**, 662 (1996).

[48] K. T. Kohlmann, M. Thiemann, and W. H. Brünger, Microelectronic Engineering, **13**, 279 (1991).

[49] K. Gamo, D. Takehara, Y. Hamamura, M. Tomita, and S. Namba, Microelectronic Engineering, **5,** 163 (1986).

[50] F. Rugamas, D. Roundy, G. Mikaelian, G. Vitug, M. Rudner, J. Shih, D. Smith, J. Segura, and M. A. Khakoo, Meas. Sci. Technol., **11**, 1750 (2000).

[51] K. T. Kohlmann-von Platen and W. H. Bruenger, J. Vac. Sci. Technol. B, **14**, 4262 (1996).

[52] R. Gomer, *Field Emission and Field Ionization* (Harvard University Press, Cambridge, Massachusetts, 1961).

[53] A. Modinos, *Field, Thermionic and Secondary Electron Emission Spectroscopy,* (Plenum Press, New York, New York, 1984).

[54] I. Brodie, C. A. Spindt, Advanced in Electronics and Electron Physics, **83,** 1 (1992).

[55] C. Lea, J. Phys. D: Appl. Phys., **6,** 1105 (1973).

[56] F. S. Baker, A. R. Osborn, J. Williams, Nature, **239,** 96 (1972).

[57] F. S. Baker, A. R. Osborn, J. Williams, J. Phys. D: Appl. Phys., **7,** 2105 (1974).

[58] S. Ijima, Nature, **354**, 56 (1991).

[59] W. Zhu, C. Bower, O. Zhou, G. Kochanski, and S. Jin, Applied Physics Letters, **75**, 873 (1999).

[60] N. de Jonge and N. J .van Druten, Ultramicroscopy, **95**, 85 (2003).

[61] N. de Jonge, Y. Lamy, K. Schoots, T. H. Oosterkamp, Nature, **420,** 393 (2003).

[62] N. de Jonge, J. Appl. Phys., **95**, 673 (2004).

[63] M. Chhowalla, C. Ducati, N. L. Rupesinghe, K. B. K. Teo, and G. A. J. Amaratunga, Applied Physics Letters, **79**, 2079 (2001).

[64] V. Semet, V. T. Binh, P. Vincent, D. Guillot, K. B. K. Teo, M. Chhowalla, G. A. J. Amaratunga, W. I. Milne, P. Legagneux, and D. Pribat, Appl. Phys. Lett., **81,** 343 (2002).

[65] E. W. Plummer, J. W. Gadzuk, and R. D. Young, Solid State Commun., 7, 487 (1969).

[66] J. W. Gadzuk, *A Century of Excellence in Measurements, Standards, and Technology– A Chronicle of Selected NBS/NIST Publications, 1901-2000.* (NIST Special Publication 9582001), p.155.

[67] J. W. Gadzuk and E. W. Plummer, Rev. Mod. Phys., **45**, 487 (1973).

[68] K. A. Dean, B. R. Chalamala, J. Appl. Phys., **85**, 3832 (1999).

[69] K. Hata, A. Takakura and Y. Saito, Surface Science, **490**, 296 (2001).

[70] K. A. Dean, B. R. Chalamala, Appl. Phys. Lett., 76, 375 (2000).

[71] M. A. Guillorn, Ph.D. thesis, Department of Materials Science and Engineering, the University of Tennessee, 2003.

[72] L. R. Baylor (unpublished).

[73] R. Collazo, R. Schlesser, Z. Sitar, Diamond and Related Materials, **11**, 769 (2002).

[74] M. A. Guillorn, M. D. Hale, V. I. Merkulov, M. L. Simpson, G. Y. Eres, H. Cui, A. A. Puretzky, and D. B. Geohegan, Appl. Phys. Lett., **81**, 2860 (2002).

[75] D. Nicolaescu, V. Filip, J. Itoh, and I. Kleps, Jpn. J. Appl. Phys., **38,** 6237 (1999).

[76] J. -M. Bonard, N. Weiss, H. Kind, T. Stöckli, L. Forró, K. Kern, A. Châtelain, Advanced Materials, **13**, 184 (2001).

[77] N. García, M. I. Marqués, A. Asenjo, A. Correia, J. Vac. Sci. Technol. B, **16**, 654 (1998).

[78] D. Nicolaescu, S. Kanemaru, V. Filip, and J. Itoh, Jpn. J. Appl. Phys., **41**, 5551 (2002).

[79] D. Nicolaescu, V. Filip, and J. Itoh, Jpn. J. Appl. Phys., **40**, 3996 (2001).

[80] D. Nicolaescu, V. Filip, and J. Itoh, J. Vac. Sci. Technol. B, **19**, 892 (2001).

[81] Y. B. Yildir, K. M. Prasad, D. Zheng, Control and Dynamics Systems, **59**, 167 (1993).

[82] www.integratedsoft.com.

[83] D. C. Joy, Microelectronic Engineering, **1**, 103 (1983).

[84] D. C. Joy, *Molecular Electronic Devices*, Edited by F. L. Carter (M. Dekker: New York, 1987), p.367.

[85] L. R. Baylor, W. L. Gardner, X. Yang, R. J. Kasica, M. A. Guillorn, B. Blalock, H. Cui, D. K. Hensley, S. Islam, D. H. Lowndes, A. V. Melechko, V. I. Merkulov, D. C. Joy, P. D. Rack, M. L. Simpson and D. K. Thomas, J. Vac. Sci. Technol. B, **22,** 3021 (2004).

[86] G. W. Ho, A. T. S. Wee, J. Lin and W. C. Tjiu, Thin Solid Films, **388,** 73 (2001).

[87] T. Ikuno, H. Furuta, T. Yamamoto, S. Takahashi, M. Kamizono, S. Honda, M. Katayama, T. Hirao, K. Oura, Surface and Interface Analysis, **35,** 15 (2003).

[88] M. A. Guillorn, T. E. McKnight, A. Melechko, V. I. Merkulov, P. F. Britt, D. W. Austin, D. H. Lowndes, and M. L. Simpson, Journal of Applied Physics, **91**, 3824 (2002).

[89] L. Dvorson, G. Sha, I. Kymissis, C. -Y. Hong, and A. I. Akinwande, IEEE Transactions on Electron Devices, **50**, 2548 (2003).

[90] J. H. Lee, Y. -H. Song, S. -Y. Kang, S. G. Kim, K. I. Cho, and H. J. Yoo, J. Vac. Sci. Technol. B, **16**, 811 (1998).

[91] J. W. Lee, B. U. Yoon, C. K. Hong, C. L. Song, J. T. Moon, M. Y. Lee, Proceedings of Advanced Metallization Conference in 1998, 243 (1999).

[92] J. J. Vlassak, Journal of the Mechanics and Physics of Solids, **52**, 847 (2004).

Vita

Xiaojing Yang was born in a farmer's family in China in 1978. Although poor, her family strongly supported her education. In 1993, she was admitted to the best senior high school in the city. She scored in the top 5 every year among more than 500 students there. She was especially good at mathematics and physics. In 1996, she had the opportunity to pursue her college study in a class specially organized for talented students in the Physics Department of Jilin University, exempt of admission tests.

In 2000, when she received her B.S. degree, she decided to pursue advanced studies in the United States. She chose the Physics Department at the University of North Carolina at Chapel Hill (UNC-CH). She worked as a teaching assistant during her first year at UNC-CH. She then joined Dr. Yue Wu's nuclear magnetic resonance (NMR) group and worked on gas adsorption properties in carbon nanotubes. This work was later published in *Physical Review B.*

In May 2002, she received her Master's degree and transferred to the Materials Science and Engineering Department at the University of Tennessee, Knoxville. Here she had an opportunity to work at Oak Ridge National Laboratory and utilize the nanofabrication facilities there. She carried out fabrication and characterization work on nanoelectronic devices. She also performed numerical simulations for electrical field distribution and charged particle ray tracing. Several papers have been produced based on her work. In May 2005, she plans to graduate with a PhD degree specializing in Materials Science and Engineering.

2094 9169 15
08/17/05 MAB